6-2016

An Exploration of CubeSat Propulsion

Andrew Davis Hine
Western Michigan University, hineandr@gmail.com

AN EXPLORATION OF CUBESAT PROPULSION

by

Andrew Davis Hine

A thesis submitted to the Graduate College
in partial fulfillment of the requirements
for the degree of Master of Science in Engineering
Mechanical Engineering
Western Michigan University
June 2016

Thesis Committee:

Kristina M. Lemmer, Ph.D., Chair
Jennifer Hudson, Ph.D.
J.P. Sheehan, Ph.D.

AN EXPLORATION OF CUBESAT PROPULSION

Andrew Davis Hine, M.S.E.

Western Michigan University, 2016

The development of new primary propulsion systems for CubeSats with the capability to complete orbital maneuvers has become a principal focus of many within the CubeSat community. One such propulsion device is the 1 cm Busek RF Ion Thruster (BIT-1). For systems such as the BIT-1 to become mission ready and implementable on spacecraft, preliminary testing must be completed to understand how these propulsion devices will perform when placed onboard. The research and testing performed and presented was used to understand how the BIT-1 propulsion device and others like it will interact with small spacecraft. This was accomplished by means of plume analysis in laboratory testing and magnetic field modeling.

ACKNOWLEDGMENTS

I am incredibly grateful to have the opportunity to thank the people who have given me so much. Though I am officially listed as the only author of this document, I alone cannot honestly take credit for everything that this thesis represents.

To my parents, John and Julie Hine, I want to say thank you. You both have helped me in countless ways, and whatever I put on this page will never be able to capture or explain how much I appreciate and love both of you. To my sister Amy, thank you for being you. I am incredibly proud of the person you have become and am honored to call you my sister. To my Grandma and Grandpa Joan and Norman Hine, Aunts and Uncles (greats and regulars), Cousins (firsts, seconds and thirds) thank you. Your love and support has helped me in more ways than you know. I am incredibly lucky to call such a wonderful group of people to call family. I love you all.

I would also like to thank all of my fellow students and lab mates who have been through this process with me every step of the way, lending their support and advice during each challenge and delay. I am grateful I did not have to face them alone. Thank you.

Next, I would like to thank the people and organizations who have supported me professionally. First off this project would not have been funded without the support of NASA's Space Technology Mission Directorate and the NASA Small Satellite Space Technology Program. Thank you for your belief in and support of this work. I would also like to thank everyone at Busek Co. Inc. Co. especially Dr. Michael Tsay for your willingness to lend guidance and advice. Thank you to Bernard Vancil at e-beam Inc. I am grateful we had the opportunity to work together and I appreciate your help in completing this research.

I would also like to thank the Jet Propulsion Laboratory and the amazing group of people who work there. You all inspire me every single day; thank you for letting me be a part of your team. It was an honor. Thank you especially to Dr. Colleen Marrese-Reading, Dr. Dan M. Goebel, Dr. Eric D. Gustafson, and Dr. Sara Spangelo.

Most importantly I would like to thank my advisor Dr. Kristina Lemmer, you have taught me so much over the past three years. I know I am a better engineer, scientist, and person because of you. Thank you for giving me the opportunity to be a part of your team. I am incredibly proud of what we have accomplished together (you getting most of that credit) and I am so excited to see all the amazing things to come for ALPE and the community we built together. Everything I will accomplish in my career is because of you. You have changed my life forever and I promise I will never forget that. If you ever need anything, all you have to do is ask. Thank you.

Andrew Davis Hine

TABLE OF CONTENTS

Table of Contents—Continued

CHAPTER

Table of Contents—Continued

APPENDICES

LIST OF TABLES

LIST OF FIGURES

List of Figures—Continued

NOMENCLATURE

Variables	Description
A	Richardson Coefficient for Cathode Inserts
$A_{corrected}$	Corrected Area of Faraday Probe
A_p/A_{probe}	Probe Area
A_s	Sheath Area
B	Magnetic Field
B_z	Magnetic Field Strength Along Z Axis
B_{zo}	Peak Magnetic Field Strength Along Z Axis
C	Capacitance
D	Diameter of Beamlet
d	Effective Grid Gap
d_a	Diameter of Aperture
d_b	Diameter of the Beam
d_s	Diameter of Screen Aperture
E	Electric Field
E_{screen}	Electric Field of Screen Grid
E_{Θ}	Electric Field Strength In Azimuth Direction
F_{accel}	Force Per Unit Area Applied to the Accel Grid
F_{ion}	Force of Ions
F_{screen}	Force Per Unit Area Applied to the Screen Grid

Variables	Description
F_{screen}	Net Force Applied to the Ion Engine
F_t	The Beam Divergence Correction Factor
g	Acceleration of Gravity
I	Current
I^*	Excited Neutral Production Rate
I^+	Singly Charged Ion Current
I^{++}	Current for Doubly Charged Ions
I_a	Electron Current Leaving Plasma to Anode
I_b	Beam Current
I_{be}	Electron Backstreaming Current
$I_{measured}$	Measured Current to Faraday Probe
I_p	Ion Production Rate
I_{probe}	Current to Probe
I_s	Ion Current to Screen Grid
I_{se}	Electron Saturation Current
I_{si}	Ion Saturation Current
I_{sp}	Specific Impulse
I_w	Ion Current to the Walls of the RF Thruster
J	Current Density
J_i	Ion Current Density

Variables	Description
k	Boltzmann's Constant
K_n	Knudsen Number
L_2	Equivalent Inductance
L_c	Coil Inductance
l_d	Distance from Accel Grid to Beam Plasma Surface
l_e	Modified Sheath Length
l_g	Gap Between Screen And Accel Grid
L_p	Plasma Inductance
l_{se}	Electron Saturation Current
l_{si}	Ion Saturation Current
M	Particle Mass
m_e	Mass of Electron
m_i	Mass of Ion
$\dot{m}_i$	Mass Flow Rate of Ions
$\dot{m}_p$	Mass Flow Rate of Propellant
N	Number Of Turns in Coil
n_∞	Density of Plasma Away from Probe
n_a	Density of Neutral Atoms
n_e	Electron Density
n_i	Ion Density

Variables	Description
$n_{i,OML}$	Ion Density from OML Calculations
$n_{i,s}$	Ion Density in the Sheath
$n_{i,thin}$	Ion Density from Thin Sheath Calculations
n_o	Density away from Edge of Plasma
p	Pressure
P_{abs}	Power Absorbed by a Plasma
P_{coll}	Probability of Collision
P_{max}	Maximum Perveance
P_{Pa}	Pressure in Pascal
PR	Power Reflected
q	Charge of a Particle
r	Radial Distance
R_2	Equivalent Resistance
R_c	Coil Resistance
r_L	Larmor Radius
R_p	Plasma Resistance
T	Thrust
t	Time
t_a	Thickness of Accel Grid
T_e	Electron Temperature in Kelvins

Variables	Description
T_{eV}	Temperature in Electron Volts
T_i	Temperature of Ions
T_{kelvin}	Temperature in Kelvins
T_m	Total Thrust For A Multi Charged Beam
t_s	Thickness of Screen Grid
t_s	Thickness of Screen Grid
U^*	Average Excitation Potential
U^+	Ionization Potential
v	Velocity of a Particle
$\bar{v}$	Maxwellian Velocity Distribution
v_E	Electric Field Drift Velocity
$v_\perp$	Velocity in the Tangential Direction to the Particle Gyration
V_a	Applied Accel Grid Potential
v_a	Ion Acoustic Velocity
V_b	Net Beam Voltage
V_{bp}	Beam Plasma Potential
v_{ex}	Velocity of Exhaust
V_f	Floating Potential
v_{gc}	Velocity of Guiding Center
v_{gc}	Velocity of the Guiding Center

<u>Variables</u>	<u>Description</u>
v_i	Ion Velocity
v_o	Bohm Velocity
V_{rf}	Voltage of RF Current
V_T	Total Acceleration Voltage
x_s	Sheath Thickness
Z	Impedance
Z_o	Source Impedance
ΔV	Voltage Difference From The Centerline to the Accel Grid Barrel

<u>Symbol</u>	<u>Description</u>
Γ_o	Incident Flux of Particles
Γ_z	Particle Flux Along Z Axis
α_m	Mass Utilization Correction Factor
γ_i	Ratio of Specific Heats
η_m	Thruster Mass Utilization Efficiency
λ_D	Debye Length
μ_o	Permeability of the Vacuum
ω_c	Cyclotron Frequency
ϕ_o	Per-Sheath Potential
ε_o	Permittivity of Free Space

Symbol	Description
φ_o	Reported Work Function
α	Thrust Correction Factor
γ	Total Thrust Correction
θ	Beam Divergence Angle
λ	Mean Free Path
ν	Collision Frequency
ρ	Charge Density of a Plasma
σ	Charge Density
σ	Spherical Cross Sectional Area of Atom
τ	Mean Time Between Collisions
ω	Frequency
ϕ	Potential Within the Plasma

Abbreviation	Description
BaO	Barium-oxide
BRICSAT-P	Ballistically Reinforced Communication Satellite
BIT-1	Busek Ion Thruster-1
CanX-2	Canadian Advanced Nanosatellite eXperiment-2
CEX	Charge Exchange Collisions
CSLI	CubeSat Launch Initiative

Abbreviation	Description
DC	Direct Current
ECR	Electron-Cyclotron Resonance
EP	Electric Propulsion
LEO	Low Earth Orbit
OPAL	Orbiting Automated Picosat Launcher
μ-CAT	Micro Cathode Arc Thruster
RF	Radio Frequency
SAPPHIRE	Stanford AudioPhonic Photographic IR Experiment
SQUIRT	Satellite Quick Research Testbed
SSDL	Satellite System Development Laboratory
STEM	Science, Technology, Engineering, and Math

CHAPTER 1

INTRODUCTION

Research Motivation

For more than a decade, CubeSats have provided an inexpensive and reliable platform for universities and other research focused organizations to conduct science in orbit. CubeSats are usually launched as secondary payloads to larger satellites. When the desired altitude is reached the 10-cm × 10-cm × 10-cm CubeSats are pushed out of a spring loaded box into orbit [1]. The liter sized CubeSat units or U's can be attached together to create larger systems; 2U, 3U, and some 6U satellites have been launched [2]. The success of these missions has created a call for the capabilities of CubeSats to be expanded; specifically in their ability to perform orbit changes with precise inclination and altitude control. CubeSats, with the exception of CanX-2 and the BRICSAT-P, have flown without any type of propulsion system [3] [4]. These control constraints have limited the science that can be performed on these satellites and constrains the orbit to free falling low earth orbit (LEO) trajectories with limited to no control over orbit altitude. For the duration of these missions without propulsion devices, positional control of satellites has thus far been limited to attitude. These constraints limit the capabilities of CubeSats and the scientific platforms they can support. With the size and weight constraints of a CubeSat being 10-cm × 10-cm × 10-cm and 1.33-kg per U [5], conventional propulsion techniques are limited in their applicability to this form. Unconventional propulsion technologies must be applied to better fill this need.

Electric propulsion (EP) is a low thrust, highly efficient technology that has the potential to be the solution to the CubeSat propulsion challenge. EP devices create beams of high energy, fast moving ions that can efficiently produce low impulse thrust. With the specific impulse, I_{sp} (ratio of thrust to propellant usage) of many of these devices being very high (over 3000-s) [6], the ability to produce thrust efficiently makes them ideal for small satellite applications. Because of the volume constraints, viable CubeSat propulsion must produce thrust efficiently, minimizing the propellant volume required to complete missions and allow room onboard for scientific payloads [3].

Several EP devices have been designed for the CubeSat platform, yet only two are known to have flown in orbit [3], [7]. To further the development of these technologies the focus must now turn towards their physical integration into spacecraft. EP devices present unique integration challenges inherent in the way they produce thrust. The beam of high energy ions created by these thrusters can negatively affect onboard electronics and payloads if not properly managed in flight. With larger satellites, sensitive equipment can be placed far away from the thruster and isolated in the event issues arise. With the small confined platform and limited mass constraints of a CubeSat, isolating the payload from the plume is not possible. Detailed analysis of the thruster beam is required to understand their performance and ensure payload survival during thruster operation. This research is focused on laboratory testing and modeling of a CubeSat ion thruster system.

Research Significance

Electric Propulsion has been studied in the United States since the mid-1960s [8]. Only in the last decade has this technology been adapted to CubeSats. In that time there have been many potentially viable propulsion systems created [9]. Now they must be evaluated and tested to understand their capabilities and limitations with respect to subsystems onboard the spacecraft.

The BIT-1 thruster is a 1-cm radio frequency (RF) ion thruster developed by Busek Co. Inc. as a propulsion system for CubeSats. While much effort went into designing this device, laboratory testing of the thruster by Busek Co. Inc. totaled less than 10 hours of operation. In general, significant efforts have gone into engineering propulsion technologies, but less work has been focused on their integration into CubeSat structures. The next investment of time and resources must be focused on defining how these propulsion devices can actually be used in space. Further development is necessary to ensure not only extended operation of the propulsion device but also how that system could inhibit the operation of spacecraft subsystems and components. The work presented in this thesis evaluates the plume of the miniaturized RF ion thruster, using laboratory testing with experimental probes and by modeling the magnetic field interaction between the thruster and current CubeSat technologies. This research was completed with the goal of evaluating the operating conditions of the thruster as well as potential CubeSat integration issues.

Organization

The introduction reviews the research topics covered by the thesis, their importance and purpose. Next a background is presented, which explores previous research, as well as provides an overview of relevant physics and topics related to the research presented. A description of the laboratory settings and experimental setup used to gather the presented research follows, along with a description of the experimental diagnostics used. The experimental results will be presented and discussed, and finally, future work and recommendations will be presented.

CHAPTER II

BACKGROUND

History and Development of CubeSats

The idea for CubeSats developed through a collaborative effort between Stanford University and California Polytechnic State University as an architecture that could yield a simplified, low cost approach to building a microsatellite capable of supporting research payloads [10]. At the time, the predominant thought was that designing a set of standards to build these devices would bring design cost down and create an opportunity for students across the country to gain experience building flight vehicles.

The recognition of the need to form these standards grew out of two satellite missions in the early 2000’s. The first of these microsatellites, designed in 1994 and launched in 2002, was called SAPPHIRE, (Stanford AudioPhonic Photographic IR Experiment) and was developed by both Stanford and Washington University [11]. Beginning in the mid-1990’s, Stanford University had founded the Stanford University Satellite System Development Laboratory (SSDL) and developed the Satellite Quick Research Testbed (SQUIRT). SAPPHIRE was the first SQUIRT satellite constructed; it weighed 25 pounds, was 18-in in diameter and 9-in tall, costing approximately $50,000 [11]. The second satellite designed at SSDL using the SQUIRT platform was called OPAL (Orbiting Automated Picosat Launcher). OPAL differed from SAPPHIRE because the mothership carried 6 picosatellites that were deployed in orbit a week after the satellite’s launch in 2000 from Vandenberg Air Force Base. These 6 4-in x 3-in x 1-in deployable picosatellites formed the foundation of what CubeSats would ultimately become [11].

CubeSat Design

From the success of the SAPPHIRE and OPAL missions, a set of standards for the first CubeSats and CubeSat deplorers were developed in 2001. The intent of the new design was to decrease the size and complexity from the initial SQUIRT platform, while still providing a simple set of standards to space qualify future missions with the capability to facilitate in-space experiments [11]. Researchers concluded that a deployable platform similar to that of the picosatellites in the OPAL mission would provide the best path forward.

The power generated by contemporary solar panels drove the size of these picosatellites. It was desired that each picosatellite would be able to produce at least 2-W from solar cells placed on all exterior sides of the satellite [11]. From the then-current solar cell technology, this surface area equated to roughly a 3.5-in × 3.5-in × 3.5-in cube [11]. Researchers determined that the standard CubeSat size would be slightly larger and be defined as a 10-cm cube, limited in weight to no more than 1-kg. The internal workings of CubeSats would be built upon a system of stacked circuit boards to manage and control all components onboard [11].

Current CubeSat Development

CubeSats have become a beneficial technology for many universities and other non-profit organizations across the United States. Because of their low cost and "off the shelf" components, many universities have developed and fostered communities and student teams devoted to designing, building and launching CubeSats [11]. The growth of these university CubeSat groups is strongly tied to NASA's CubeSat Launch Initiative (CSLI), which was created in 2010. CSLI was designed to grant launch opportunities to accredited educational organizations and nonprofit organizations as part of NASA's larger STEM (Science, Technology, Engineering, and Math) education initiatives [12]. CSLI reserves auxiliary payloads for CubeSats designed by educational and nonprofit organizations, thereby drastically reducing launch cost and increasing flight opportunity.

As of January 2016, CSLI has received 158 mission proposals and selected 110 for flight from 61 unique organizations: it has flown 36 CubeSats [12]. A majority of these CubeSat missions have been focused on low-cost technology development and other scientific research projects. From the success of CSLI, NASA continues to invest in advancing CubeSat technology, especially technologies related to CubeSat primary propulsion.

Magnetic Stabilization

Many control strategies have been implemented on spacecraft in orbit. For CubeSats, historically, these methods have primarily been comprised of momentum wheels and either passive or active magnetic stabilization to control spacecraft pointing [13]. Magnetic stabilization uses the earth's magnetic field to align the spacecraft [14].

The pointing direction or attitude of the satellite is then dependent on the Earth's magnetic field lines along the orbit path [13]. Passive magnetic systems use a set of permanent magnets on board to accomplish this pointing. These types of systems have been used on many CubeSats and are considered a flight-ready technology [13]. It is necessary to determine whether passive magnetic stabilization systems can be integrated into the same CubeSat as an EP system [15], [16], [17].

CubeSat Propulsion Technology Overview

Up to this point, CubeSats have primarily flown as university experiments with great success. This has led to interest from other parties, governmental and private industry, who want to expand the capabilities of CubeSats [3]. A well-developed CubeSat propulsion system could allow for expanded mission capabilities such as orbit changes, formation flying, fine attitude control and interplanetary missions [3]. A wide array of propulsion technologies that are applicable to CubeSats have been proposed and developed by industry, universities and NASA. Existing technologies like butane thrusters [18], pulse plasma thrusters [19], and vacuum arc thrusters [20] have been adapted in their current form to fit CubeSat structures and constraints. This research has also included older and larger propulsion systems like 'green propellant' monopropellant thrusters [21] and ion thrusters [22] [23], that have been adapted and shrunk down to fit within CubeSat architectures. There has also been an emergence of new technologies like micro electrospray thrusters that are highly scalable [24], [25], [26].

Ion Thruster Overview

Ion thrusters, sometimes referred to a gridded ion thrusters are characterized by their implementation of electrostatic acceleration grids to create a continuous, accelerated, stream of positive ions [6]. The first known operational space test of an ion thruster type system in the United States was the Space Electric Rocket Test 1 or (SERT 1) in 1964 [8]. This mission verified that a beam of high velocity ions and low velocity electrons could be produced continuously in orbit and create thrust. All ion thrusters must accomplish three basic tasks to function. First, the device must be able to generate plasma, second it must be able to accelerate the ions of the plasma, and lastly this beam of accelerated ions must be neutralized with the use of an electron source [6]. The widest variation in how different types of ion thrusters are designed is determined by the plasma generation method. There are three commonly accepted types of plasma generators currently employed on ion thrusters, direct current or DC electron discharges, microwave discharges, and radio frequency discharges. All three types of systems typically use a series of optically aligned, electrically biased, multi-aperture grids to accelerate the ions of the plasma. An externally mounted neutralizer cathode is commonly employed to produce electrons for neutralizing the ion beam. Neutralizing the plasma is necessary to maintain spacecraft and thruster potential, relative to the ambient space plasma potential, thus avoiding preferentially charging the spacecraft [8],[6].

Ion Accelerators

The method by which ions are accelerated in gridded ion thrusters is the same regardless of the type of ionization method used. The ionized gas is accelerated the electrostatically charged grids that bound one side of the discharge chamber [6]. As shown in Figure 1, adapted from the "Fundamentals of Electric Propulsion" by Goebel and Katz [6], the inner most grid, referred to as the screen grid, is responsible for extracting the ions from the discharge chamber by focusing the created ions through the apertures. The second grid is called the accelerator grid or accel grid, and is held at a negative potential relative to the potential of the spacecraft [6]. The ions are accelerated due to the potential drop between the grids. As the result of very precise optical grid design the accelerated ions will remain in a low divergence envelope that allows them to escape the apertures of both grids and be accelerated away, producing thrust. The negative bias on the downstream side of the grid decelerates the ions slightly, but prevents electrons from back streaming into the discharge chamber [6]. In some cases an additional third decelerator grid or decel grid is added past the downstream side of the acceleration grid. The decel grid is kept at ambient space potential to act as a physical shield that limits erosion on the downstream face of the accel grid and decreases overall beam divergence [8].

Direct Current Ion Thrusters

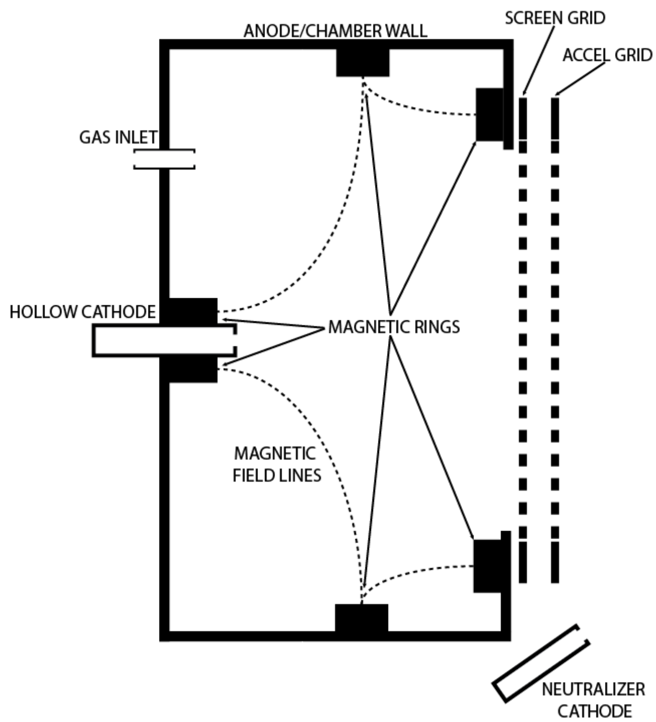

Figure 1: Schematic of typical DC Ion Thruster [6]

A typical DC ion thruster, shown in Figure 1, operates using four basic subsystems; a cathode inside the discharge chamber to produce electrons, magnetic rings to confine the electrons that induce ionization, a set of acceleration grids to produce the ion beam and a neutralizing cathode to neutralize the charge of the plasma beam [6]. Neutral propellant gas is introduced into the discharge chamber or body of the thruster from two pathways, directly into the discharge chamber and at a much smaller flow rate through the internal cathode [8]. The role of the internal cathode is to produce electrons for ionization. Typically hollow cathodes are used for this purpose. The specifics of how hollow cathodes produce the electrons and the ionization process will be reviewed in a later section. After electrons are produced by the internal cathode, they are confined by the magnetic field lines created by the constant DC magnetic coils positioned around the exterior of the discharge chamber [6]. For DC ion thrusters the design of this magnetic field configuration is crucial in determining how efficiently the thruster will operate. The magnetic field is implemented to confine energetic electrons and increase the ionization probability and efficiency of the discharge. The created magnetic field also controls electron loss to the anode, which is the wall of the discharge chamber [6]. The propellant flowing directly into the discharge chamber is ionized by these confined high energy electrons to produce plasma.

Microwave Ion Thrusters

Microwave ion thrusters use high microwave frequencies to create electromagnetic fields that induce ionization. There are multiple electron resonances that can be exploited for excitation: the electron-cyclotron resonance (ECR), and an upper and lower hybrid resonances. Microwave thrusters use both the ECR and the upper-hybrid resonance in concert to ionize propellant atoms [27]. In microwave thrusters conditions must be precisely controlled because the electromagnetic waves will only be absorbed by the plasma under specific conditions. Microwave radiation is difficult to control and harness. If conditions in a system are not ideal, the microwave energy can be completely reflected by the plasma [6].

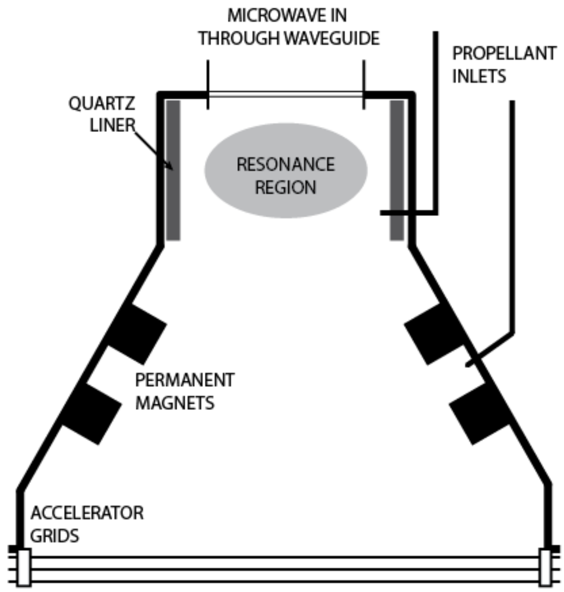

Figure 2: Diagram of Microwave Ion Thruster [6]

To create plasma using microwave energy with a sufficient density to sustain the discharge through the grids, high magnetic fields (100-G to 4000-G) and high microwave frequencies (1 to 10-GHz) are needed [6]. These conditions are too difficult to maintain over the volume of the entire discharge chamber, and the microwave ionization is confined to a resonance region. As seen in Figure 2, adapted from the "Fundamentals of Electric Propulsion" by Goebel and Katz [6], the resonance region is enclosed with a quartz liner to prevent high energy electrons from being lost to the wall of the thruster. Once created, the plasma is expanded to the grids with divergent magnetic fields created with permanent magnets placed around the discharge chamber [6].

Radio Frequency (RF) Ion Thruster

In RF ion thrusters a helical coil or antenna is positioned surrounding the discharge chamber. Energized at a low MHz frequency the RF coil is used to ionize neutral propellant gas [28]. This plasma generation technique is sometimes preferred over comparable DC systems because of its simplicity. In RF configurations there is no need for externally applied magnetic fields because sufficient containment for ionization is provided by the electromagnetic field induced by the coil [6]. Unlike DC ion thrusters the discharge chamber walls are nonconductive, physically isolating the RF coil from the coupled plasma [6]. As seen in Figure 3, adapted from the “Fundamentals of Electric Propulsion” by Goebel and Katz [6], there is also no need for an internal electron source within the discharge chamber of the thruster. With DC systems, the high energy electrons created with the internal cathode exhaust a majority of their energy during ionization collisions with the neutral propellant gas. After ionization the electrons are lost to the anode walls of the discharge chamber. The internal cathode is required to continuously supply new high energy electrons to sustain ionization [6].

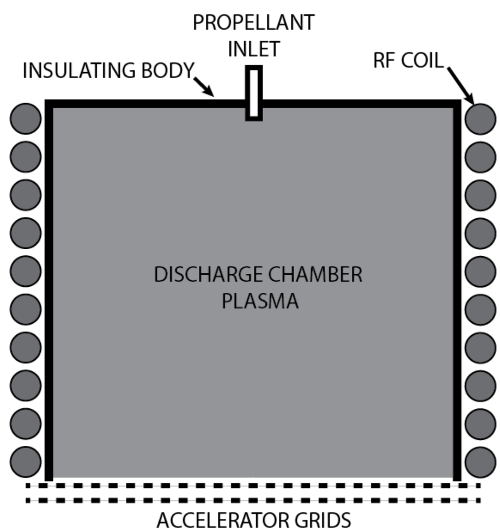

Figure 3: RF Ion Thruster Diagram [6]

With RF ion plasma thrusters, a constant source of new electrons within the discharge chamber is not necessary. When ionization of the neutral propellant occurs, additional free electrons from the ionization collision are introduced into the system. These newly free electrons are themselves coupled to the RF power of the coil and drive the ionization of other neutral propellant atoms. This chain reaction sustains the discharge [28]. While this configuration is ideal once the ionization chain reaction is underway, RF systems need free electrons to begin the ionization of neutral propellant flowing into the discharge chamber.

There are several accepted methods used to obtain these ‘seed’ electrons in RF thrusters. When operating RF systems in a vacuum chamber, under very idealized settings and high power, the few electrons naturally present within the system can be excited to begin ionization or cause field emission [6]. This process works only in vacuum facilities because unlike in space, at higher backpressures there are electrons naturally present within the chamber that can be excited. Field emission occurs when electrons are released from the discharge chamber materials induced by the applied electrostatic field [29]. A spark generator or a small cathode can also be used. The other commonly accepted method uses the external neutralizer cathode to provide the seed electrons [28]. The challenge is getting a sufficient number of these electrons from the external cathode into the discharge chamber to begin the ionization [28]. With the external grid of the thruster being normally held at a negative potential, neutralizer electrons are repelled. To attract the electrons into the discharge chamber the polarity of the accel grid can be switched momentarily, attracting the external electrons into the discharge chamber and allowing the ionization reaction to begin [28].

The RF current in the coil induces a time dependent electric and magnetic field in the discharge chamber that heats the Maxwellian electron distribution and provides the energy for ionization [6]. The power loss from or the power out of the plasma is equal to the RF power absorbed by the plasma. By adding all of the electron and ion loss terms the RF power that is coupled and absorbed by the plasma can be calculated [6],

$$P_{abs} = I_p U^{+} + I^{*} U^{*} + (I_s + I_w + I_b)\left(\frac{T_{eV}}{2} + \phi\right) + I_a(2T_{eV} + \phi). \tag{1}$$

The magnetic field produced by the RF coil can be modeled in the following way, where ω is the cycle frequency of the RF [6],

$$B_z = \frac{NI}{\mu_o} e^{i\omega t}. \tag{2}$$

An azimuthal electric field is also produced according to Equation 3, dependent on the distance from the axis, r, [6],

$$E_\theta = -\frac{i\omega r}{2} B_{zo} e^{i\omega t}. \tag{3}$$

Development of an RF circuit that can couple efficiently with the plasma it is producing is challenging. If an RF thruster is not designed properly, the energy from the RF voltage will be dissipated within the transmission circuit and not used for the excitation of electrons [30]. Ensuring that the RF energy is coupled with the plasma is referred to as impedance matching. RF ion thruster circuits can be modeled as a transformer to show how the system will interact with the plasma it creates and the quality of the matching circuit [31].

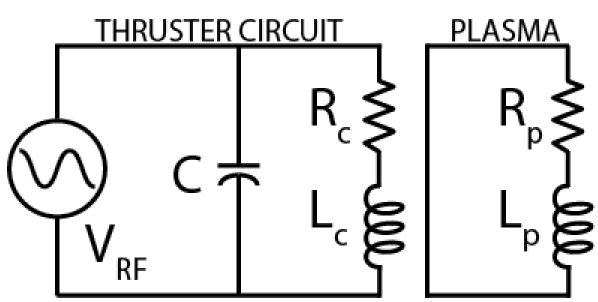

Figure 4: A Micro-RF Ion Thruster Circuit Model and Plasma [32]

Both adapted from "Numerical Modeling of a Radio-Frequency Micro Ion Thruster" by Tsay, [32] Figure 4 shows the primary circuit and Figure 5 shows the equivalent circuit of the thruster and plasma together [32]. This method was developed by Lieberman and Gudmundsson [33] and is one of several adapted by Tsay, et al. during the development of the BIT-1 [32].

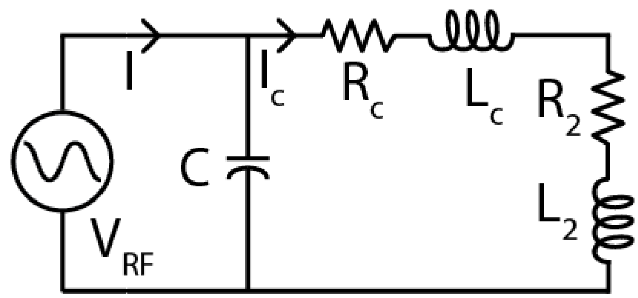

Figure 5: Equivalent Micro-RF Ion Thruster Circuit [32]

The total load impedance, is used to characterize the quality of the matching circuit [32],

$$Z = \frac{\left(\frac{1}{j\omega C}\right)(R_c + R_2 + j\omega L_c + j\omega L_2)}{\left(\frac{1}{j\omega C}\right) + (R_c + R_2 + j\omega L_c + j\omega L_2)}. \tag{4}$$

The quality of the impedance matching is expressed as the percentage of power reflected or the power not absorbed by the plasma, where the source impedance normally is 50 Ω [31],

$$PR = \left|\frac{Z - Z_o}{Z + Z_o}\right|^2 \times 100\%. \tag{5}$$

Hollow Cathodes

For DC and RF ion thrusters, cathodes are required to supply seed electrons for ionization, as well as neutralize the plasma plume of the thruster. In this research, hollow cathodes were used for both of these purposes. This section will review hollow cathodes and offer an explanation as to their functionality.

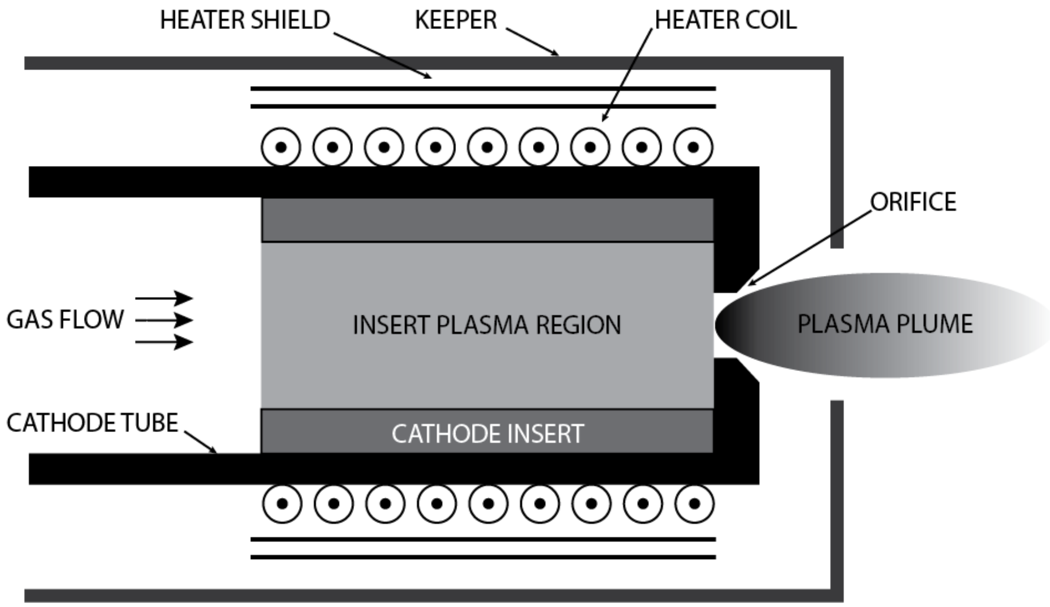

Figure 6: Diagram of a Hollow Cathode [6]

Figure 6, adapted from "Fundamentals of Electric Propulsion" by Goebel and Katz [6], shows the basic components in every hollow cathode. Electron source cathodes operate by heating an active electron emitter, called the insert. The insert is made of a material with a low work function that when heated releases electrons. These electrons ionize a neutral gas flowing through the cathode tube. The discharge current electrons from the cathode plasma are then extracted by a potential applied to the surrounding keeper [6]. Hollow cathodes differ from other cathode devices because once the discharge of a hollow cathode is ignited it can operate in what is called a self-heating mode, where the heater can be turned off and the discharge will continue [6]. Self-heating cathodes are ideal for spacecraft because of the lower power required to sustain the operation of the cathode during flight.

There are several different insert materials used in hollow cathodes. For the experiments and data collected and discussed in this thesis Barium-oxide (BaO) hollow cathodes were used. Discussion on cathode emitter material will be limited to this emitting material. BaO inserts are made with a porous tungsten matrix that is typically filled with an emissive mixture of four parts barium oxide, one part calcium oxide and one part alumina [6]. Electron emission occurs when chemical reactions in the pores of the tungsten matrix create a barium-oxide dipole. The work function of a material defines how much energy is required for it to release an electron. The work function for BaO emitting material above 800°C is about 2.06 eV. This value can be lowered by altering the chemical makeup of the insert [6]. To emit 10 A/cm^2 a typical BaO insert needs to reach 1000°C [6]. The current density emitted by an insert can be calculated with the following equation, where A is a constant depending on the material. For BaO the value of A is 120 A/cm^{2}K^2 [6].

$$J = Ae^{-e\alpha/k} T_{kelvin}^2 e^{-e\phi_o/kT}, \tag{6}$$

Ion Acceleration

The mechanism for ion acceleration fundamentally defines how an ion thruster creates propulsion [6]. The design of the gridded ion accelerator system characterizes the lifetime, performance, and size of the thruster [6]. The ion accelerator, or ion optics, serves several functions. The grid system limits neutral gas outlet flow, it extracts and accelerates ions from the discharge chamber, and it prevents electrons from the neutralizer reaching the screen grid [6].

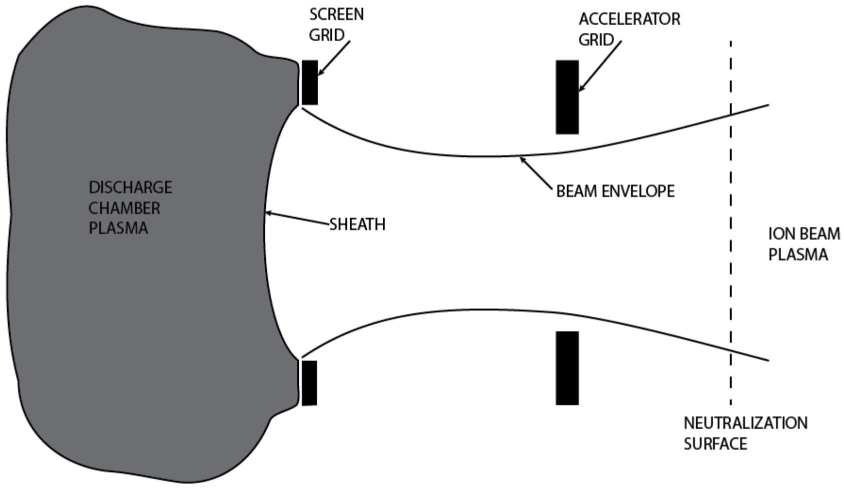

Figure 7: Schematic of a Single Aperture of an Ion Accelerator [6]

In typical ion acceleration systems there are two optically aligned grids encapsulating one end of the discharge chamber. Figure 7, adapted from "Fundamentals of Electric Propulsion" by Goebel and Katz [6], shows a single aperture pair of an ion accelerator. The design of these grid systems is complicated, but there are general rules that lead designers of ion optics systems towards idealized solutions. The transparency of the screen grid and space-charge limitations control the maximum number of ions that can be extracted from the plasma generator [6]. The screen grid aperture diameter is designed close to its maximum value. On the other hand, it is desirable to minimize the transparency of the accel grid to limit neutral gas losses [6]. For the optics to function properly, minimal direct contact between the formed beamlet of ions and the accelerator grid is desired. If designed properly, ion accelerator grids produce a highly directional focused beam of accelerated ions.

The Child-Langmuir law defines the maximum ion current that an ion accelerator can extract from the discharge chamber to form an accelerated beam for a given applied voltage. The Child-Langmuir Law is described by the following equation, [6]

$$J_i = \frac{4\varepsilon_0}{9}\left(\frac{2e}{M}\right)^{1/2}\frac{V^{3/2}}{d^2} \qquad (7)$$

This current limit for a set voltage is called the perveance. For round apertures, assuming a planar sheath, the perveance is defined by Equation 8 [6]. It is important to note that the perveance is not a current density value, rather it represents the relationship between the maximum current that can be extracted by grids at a set voltage [6],

$$P_{max} \equiv \frac{\pi\varepsilon_0}{9}\sqrt{\frac{2q}{M}}\left(\frac{D^2}{d^2}\right)\ \left[\frac{A}{V^{\frac{3}{2}}}\right]. \qquad (8)$$

From this, the maximum extraction capability can be increased by decreasing the spacing between the grids or by increasing the total acceleration voltage of the system. The total acceleration voltage, V_T, in two-gridded ion thrusters, is defined as the total potential drop between the screen grid potential and the accel grid potential. The magnitude of the total acceleration voltage is dependent on the magnitude of the accel grid voltage. The total acceleration voltage could also be amplified by increasing the potential of the screen grid. Changing the screen grid voltage will also change the net acceleration voltage and increase the ion beam velocity as shown in Figure 8, adapted from "Fundamentals of Electric Propulsion" by Goebel and Katz [6]. The ion beam velocity defines the specific impulse of the system and in practice this value is fixed. So the net acceleration voltage is usually never adjusted [6].

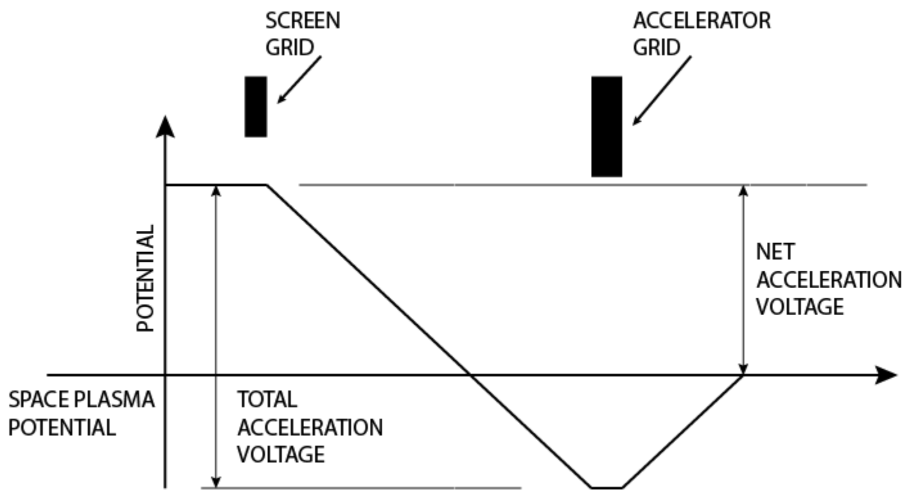

Figure 8: Potentials within Ion Accelerator Grids without Plasma [6]

Using the perveance relationship shown in Equation 8, it becomes possible to calculate the maximum current density that can be extracted from a gridded ion accelerator system. As depicted in Figure 7, the plasma sheath transition boundary within the aperture of the screen grid is curved. In this region the plasma electrons begin to be influenced by the negative potential of the accel grid and are repelled away from the aperture [34]. Because there is a distribution of energies between all the plasma electrons, the depth of the penetration into the ion accelerator systems is varied, resulting in a non-planar sheath boundary [34], [35]. The potential within a single aperture pair with plasma is highlighted in Figure 9, adapted from “Ion Extraction from a Plasma” by Aston, et al [34].

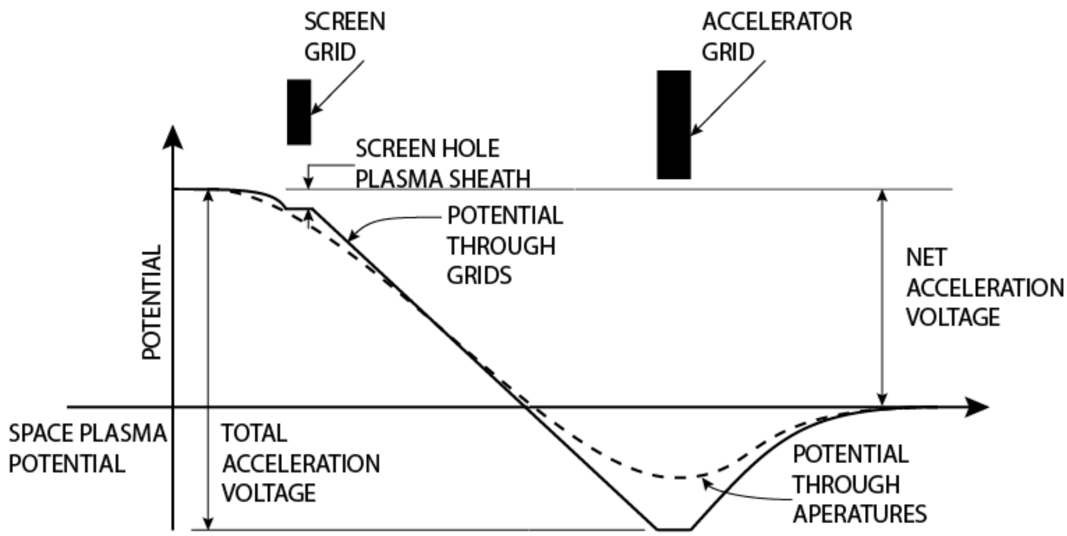

Figure 9: Potential Along a Single Aperture when Plasma Present [34]

Applying this modified sheath thickness, pictured in Figure 9, to the Child-Langmuir equation, the maximum current density can be calculated using the following equation [6],

$$J_{max} = \frac{4\varepsilon_o}{9}\sqrt{\frac{2e}{M}}\frac{V_T^{3/2}}{l_e^2}. \tag{9}$$

l_e, the modified sheath length represented in Figure 10, adapted from “Fundamentals of Electric Propulsion” by Goebel and Katz [6]. The modified sheath length is defined as the distance from the plasma sheath to the point of minimum electric potential between the grids, V_m. This distance is calculated using the following equation with the ion accelerator dimensions shown in Figure 10 [6],

$$l_e = \sqrt{\left(l_g + t_s\right)^2 + \frac{d_s^2}{4}}. \tag{10}$$

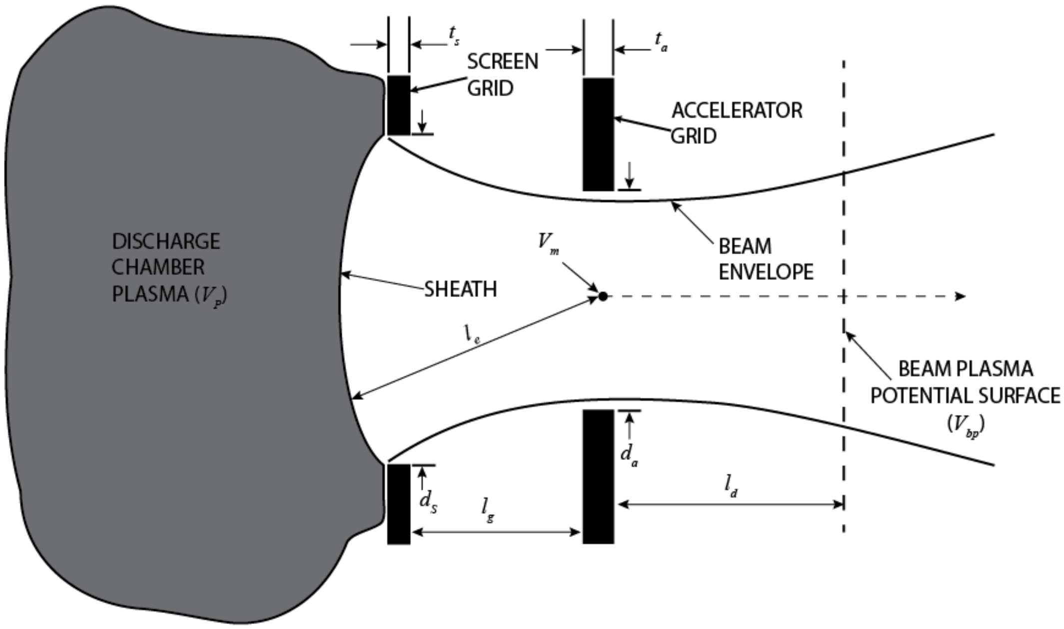

Figure 10: Ion Accelerator Dimension [6]

Expansion of Grid Apertures in Large and
Small Ion Thrusters

During operation of larger ion thrusters the grids will thermally expand due to heating from bombardment or direct contact with the discharge plasma. Thermal expansion of the grids will directly affect the optics and ion trajectories. Expansion must be accounted for in designing accelerator grid systems. Grids can be designed to be either convex (domed outwards from the thruster body) or concave (domed into the thruster body) to afford sufficient rigidity to avoid contact during launch and mission duration [36]. In convex grid systems the gap between the screen and accel grids shrinks as the grids expand. Since the screen grid is directly exposed to the discharge chamber plasma and designed to be as thin as possible to increase transparency, it will expand more than the accel grid [6]. This reduction in the grid gap at operating temperatures increases the perveance of the grids, altering the beamlet trajectories and leading to field emission and high voltage breakdown problems if the expansion is not properly accounted for [6]. Concave grids alternatively expand in the opposite direction. Screen grid expansion increases the grid gap distance and decreases the perveance [6].

For smaller ion thrusters, (≤ 3cm diameter) grid geometries are much more resistant to vibration and do not deform to the same degree as larger thrusters at operating temperatures. Flat grid systems are typically used in small ion thrusters [22]. Smaller grid diameters allow for smaller grid gaps and smaller accelerator grid apertures because of the drastic potential drop between the grids. In general, the closer together the grids in a thruster system are, the better the system is at confining unionized propellant in the discharge chamber and drawing a high current through the apertures. For this reason smaller thrusters have higher perveance limits and can produce higher thrust densities [22], [37].

Thrust and Ion Accelerators

In ion thrusters, all thrust is generated from the interaction between plasma ions and the electrostatic acceleration grids. The difference in voltage between the two grids creates an electric field across the gap separating the two grids. Within this gap two opposing forces from the screen grid and accel grid are applied to the ions. The force per unit area applied to the screen grid is equal to the charge density multiplied by the average electric field; which is equal to half the field outside the conductor [6].

$$F_{screen} = \sigma \frac{E_{screen}}{2} \tag{11}$$

This relationship can be further simplified to directly relate the electric field of the screen grid to the force on the grid. Assuming the grid is a perfect conductor, the surface charge density is equal to [6]

$$\sigma = \varepsilon_0 E_{screen}, \tag{12}$$

and the force on the screen is [6],

$$F_{screen} = \frac{1}{2}\varepsilon_0 E_{screen}^2. \tag{13}$$

The force on the accel grid is calculated in the same manner. Since the electric charge on the accel grid is negative, the direction of the force felt by the grid is in the opposite direction [6],

$$F_{accel} = -\frac{1}{2}\varepsilon_0 E_{screen}^2. \tag{14}$$

The net force applied to the ion engine is the sum of the force on the screen and accel grid [6],

$$F_{engine} = F_{screen} + F_{accel} = \frac{1}{2}\varepsilon_0 (E_{screen}^2 - E_{accel}^2). \tag{15}$$

This can be proven by solving for the force per unit area on the ions within the grid gap [6],

$$F_{ion} = \varepsilon_0 \int_{E_{screen}}^{E_{accel}} E dE = \frac{1}{2}\varepsilon_0 (E_{accel}^2 - E_{screen}^2). \tag{16}$$

The force felt by the engine is equal to, [6],

$$F_{engine} = F_{screen} + F_{accel} = -F_{ion}. \tag{17}$$

To calculate the thrust, basic rocket equations are converted to be applicable to electrostatic thrusters. The thrust of any rocket can be defined by the time rate of change of the momentum. The thrust is expressed as the flow rate of the propellant multiplied by the velocity of the propellant exhaust [6],

$$T = \dot{m}_p v_{ex}. \tag{18}$$

For ion thrusters, the velocity of the propellant exhaust is equivalent to the velocity of the accelerated ions in the beam [6]. The ion exhaust velocity is defined by the following equation [6],

$$v_i = \sqrt{\frac{2qV_b}{M}}. \tag{19}$$

The ion mass flow rate can then be related to the beam current by the following equation, where M is the mass of a single propellant ion [6],

$$\dot{m}_i = \frac{I_b M}{q}. \tag{20}$$

Combining equations 18 and 19 into Equation 17 gives an equation for thrust of an EP system [6],

$$T = I_b \sqrt{\frac{2MV_b}{q}}. \tag{21}$$

Two correction factors that must be used to accurately calculate thrust. The first correction is for the divergence of the plume. In thruster systems the accelerated exhaust will not be only in the axial direction. The angle at which the thruster exhaust spreads is called the beam divergence angle, θ. The beam divergence correction factor for non-uniform beams is calculated using the following equation [6],

$$F_t = \frac{\int_0^{r'} 2\pi r \, J(r) cos\theta(r) dr}{I_b}. \tag{22}$$

For uniform beams Equation 22 reduces to [6],

$$F_t = cos\theta. \tag{23}$$

The second correction required to calculate thrust is for multiply charged ion species within the plasma plume since doubly charged ions will be affected by the electric fields of the grids differently than singly charged ions. The total thrust for a multi-charged beam is found by calculating the thrust for singly and doubly charged ions independently and adding them together, as shown in Equation 23 [6].

$$T_m = I^+ \sqrt{\frac{2MV_b}{q}} + I^{++} \sqrt{\frac{MV_b}{q}} = I^+ \sqrt{\frac{2MV_b}{q}} \left(1 + \frac{1}{\sqrt{2}} \frac{I^{++}}{I^+}\right) = I^+ \sqrt{\frac{2MV_b}{q}} \alpha. \qquad (24)$$

The total thrust correction can be expressed by the following equation [6],

$$\gamma = \alpha F_t. \qquad (25)$$

And the corrected thrust can be calculated [6],

$$T = \gamma \dot{m}_i v_i = \gamma \sqrt{\frac{2M}{q}} I_b \sqrt{V_b}. \qquad (26)$$

Specific Impulse and Ion Accelerators

Specific impulse or I_{sp} is an essential characteristic of all thruster systems. It measures the ratio of thrust to propellant usage, providing a measure of thrust efficiency. I_{sp}, shown in Equation 26 is used to compare thruster systems [6],

$$I_{sp} = \frac{T}{\dot{m}_p g}. \qquad (27)$$

To convert the standard I_{sp} equation into a form that can be applied to ion thrusters and other electric propulsion devices Equation 18 must be used for thrust [6],

$$I_{sp} = \frac{v_i \dot{m}_i}{g \dot{m}_p}. \qquad (28)$$

Equation 28 leads to another efficiency term known as thruster mass utilization efficiency or the ratio of propellant flowing out of the thruster that is actually ionized. Another correction factor, α_m is required to account for doubly charged ions. While singly and doubly charged ions have the same basic mass unit they differ in the charge they carry. The ratio of single to doubly charged ions must therefore be incorporated [6].

$$\alpha_m = \frac{1 + \frac{I^{++}}{2I^{+}}}{1 + \frac{I^{++}}{I^{+}}} \tag{29}$$

The corrected thruster mass utilization efficiency is then [6],

$$\eta_m = \alpha_m \frac{\dot{m}_i}{\dot{m}_p} = \alpha_m \frac{I_b M}{q \dot{m}_p} \tag{30}$$

Adding thruster mass utilization, the total thrust correction from Equation 25, and substituting Equation 19 for the ion exhaust velocity, the final equation for I_{sp} in ion thrusters is [6],

$$I_{sp} = \frac{\gamma \eta_m}{g} \sqrt{\frac{2qV_b}{M}} \tag{31}$$

Ion Thruster Lifetimes

One of the main limiters of any gridded ion thruster's lifetime is the sputter erosion of the accelerator grid system. Sputter erosion occurs when ions with sufficient energy strike the surface of the grids ejecting atoms of the grid material. When designing ion thrusters engineers make specific choices to limit the erosion of the grids and extend the life of the thruster [6]. Since their invention this area has been constantly researched, developing strategies and operating points that limit and control erosion. Eroding of the grid system is detrimental because the grid apertures can become too large to prevent electron backstreaming or the grids from failing structurally [6].

Electron backstreaming refers to the flow of electrons from the downstream neutralizer cathode backwards into the discharge chamber. In un-eroded grid systems the negative potential of the accel grid creates a barrier that keeps all but the highest energy electrons out of the discharge chamber. Preventing electron backstream is critical because backstreaming electrons can overheating and damage thruster components [6]. If the accel grid material is sufficiently eroded the electron current to the screen grid will be several hundred times greater than the ion current and all of the electrical power of the thruster will be wasted [6].

The screen grid and accel grid erosion are caused in different ways. For the screen grid, the primary cause of erosion comes from direct ion bombardment by low energy ions from the discharge chamber [6]. Typically, ion bombardment can be controlled with proper thruster design. In DC thrusters, the energy level of the ions within the discharge chamber is controlled by the potential difference between the anode and internal cathode. Typically this can be kept below the sputter yield of the grid material [6]. If ions within the discharge chamber are doubly or even triply charged the same potential difference will induce high enough kinetic energy to erode the screen grid [8]. Erosion of the screen grid can also be limited by making it as thin as possible. A thin grid reduces the length of the acceleration region and leads to a high thrust density and a lower density of multiply charged ions within the plasma [8].

Erosion of the accel grid is primarily cause by a plasma event called a charge exchange collision (CEX), or resonant charge exchange. Accel grid erosion occurs in two regions, the gap between the screen and accel grid and the downstream face of the accel grid [6]. CEX's occur when a high energy ion impacts a slow moving neutral propellant gas atom escaping the grids. This impact will transfer an electron from the neutral atom to the high energy ion. This exchange converts the low energy neutral into a slow thermal ion, and the high energy ion into a high energy neutral [6]. These collision also change the direction of the particles. Removing the slow thermal ion from the well-developed beamlet. It is then free to be drawn into the accel grid which can lead to sputter erosion. Typically, these currents to the accel grid are small; around 1% of ions will interact with neutral gas atoms in such a way [8]. When these collisions occur between the grids, the newly created ions tend to impact the inside face of the accel grid apertures, increasing the diameter [6]. The widening of accel grid apertures is called barrel erosion. It negatively affects thruster operation because it leads to increased electron backstreaming. Electron backstreaming can be controlled during flight or extended operation by increasing the negative bias as the apertures widen to maintain the minimum potential to reject neutralizer electrons. The thruster fails when the maximum potential of the accel grid supply is reached and electron backstreaming can no longer be prevented [6].

The second region of grid erosion results from CEX downstream of the accel grid, before the beamlets merge to form a single plasma beam. These CEX ions are attracted back to the accel grid, causing erosion of the downstream face of the grid. This is called ‘pit and groove’ erosion, named for the pattern it creates on the grid face [6]. This type of erosion can lead to failure in two ways. It causes the grid to structurally fail and can also widen the grid apertures introducing electron backstreaming [6]. This erosion mode can be controlled or at least limited. The thickness of the accel grid does not significantly affect ion extraction performance and the accel grid is made thicker to allow more material to be eroded before a failure point is reached [8]. Furthermore, reducing the magnitude of the negative potential on the accel grid can limit the energy of the impacting ions and decrease erosion, but the potential must not be decreased to a level that allows electron backstreaming. This potential constraint is called the backstreaming limit. Defined as the voltage where the backstreaming electrons increase the current to the screen grid by 1% [6], the backstreaming limit can be calculated using the following equation [6],

$$\frac{I_{be}}{I_i} = \frac{exp\left[\frac{V_a + \Delta V + (V_{bp} - V_a)C - V_{bp}}{T_e}\right]}{2\sqrt{\pi \frac{m}{M}\frac{(V_p - V_{bp})}{T_e}}}. \tag{32}$$

ΔV is the voltage difference from the centerline to the accel grid barrel due to space charge [6],

$$\Delta V = \frac{I_i}{2\pi\varepsilon_o v_i}\left[\ln\left(\frac{d_a}{d_b}\right) + \frac{1}{2}\right], \tag{33}$$

and C is a geometric term defined by the variables in Figure 10 [6],

$$C = \frac{d_a}{2\pi l_e}\left[1 - \frac{2t_a}{d_a}\tan^{-1}\left(\frac{d_a}{2t_a}\right)\right] e^{\frac{-t_a}{d_a}}. \tag{34}$$

Erosion of the grids can also be manipulated with the addition of a third grid, the decal grid, downstream of the accel grid. The decel grid is maintained at or near the space plasma potential, and shifts erosion from the downstream face of the accel grid to the inner surface of the apertures causing barrel erosion. Barrel erosion is preferred to pit and groove erosion because the electron backstreaming can be controlled by changing the operating of the thruster during flight and barrel erosion takes longer to cause mechanical failure [6]. The addition of the decel grid also helps prevent spacecraft contamination. When the decel grid is present, only 12% of the sputtered material escapes the thruster;

compared to a two grid system where nearly all sputtered material is lost [8]. With the addition of a decel grid, a majority of the sputtered material is redeposited on the downstream face of the screen grid or the upstream face of the decel grid [8].

Challenges of Miniaturizing and Integrating an Ion Thruster

As stated previously the research presented in this document focuses on a miniaturized RF ion thruster applied to CubeSat propulsion. The task of engineering such a device is not trivial. Reducing the size of these types of RF devices presents many design challenges that make finding an optimal design problematic. For example, the shortest discharge chamber geometry would be ideal to minimize ion loss to the discharge chamber wall. To minimize the discharge chamber surface area the dimensions of the coil would also have to be reduced. By reducing the geometry of the coil, the inductance of the coil would also decrease and ohmic heating would become severe [28]. Using an RF frequency that produces an RF field that has a skin depth or penetrates 1/2 to 2/3 the radius of the discharge chamber is ideal [30]. This is not always possible because increasing the RF frequency increases the series effective resistance and in turn increases the ohmic heating of the coil [28]. For these reasons finding an optimal RF circuit design is difficult to achieve.

Since there is limited space onboard CubeSats all the components must function within close proximity to each other. This presents another design challenge because having EP thrusters near sensitive electronics onboard spacecraft is an area of concern. It has been shown with simulation [38] and in flight [39] that EP devices can influence the charge on larger spacecraft when the accelerated ion beam of the thruster is not properly neutralized. Charge exchange ions are shown to have the ability to significantly change the spacecraft floating potential [38]. In CubeSats, neutralization becomes even more crucial. The plume of any ion thruster contains more than ionized, accelerated propellant and neutralizing electrons. Neutral propellant gas, low energy charge exchange ions, and sputtered grid and thruster material are all contained within the plume [40]. On larger spacecraft solar panels, payloads and electronic controls can be placed far away, isolating them from the thruster plume. With CubeSats this is not possible; therefore, EP devices with low divergent plumes are ideal for CubeSat applications.

Plasma Motion in Ion Thrusters

A plasma, as defined by Chen, “is a quasi-neutral gas of charged and neutral particles which exhibits collective behavior.” [41] There are two central aspects to this definition. First aspect is the condition of quasi-neutrality, meaning that the density of electrons and the density of the ions within the plasma is relatively equal [41],

$$n_i \approx n_e. \tag{35}$$

The second aspect is the collective behavior of plasmas. Since particles within a plasma are charged, motion of a single particle has a collective effect on every other particle within the plasma. This shifting, push and pull, of each particle on one another creates momentary concentrations of positive and negative charges, leading to flowing currents in the plasma and inducing magnetic fields [41].

Plasmas in ion thrusters obey Maxwell’s four equations formulated in vacuum listed below [6],

$$\nabla \cdot E = \frac{\rho}{\varepsilon_0} \tag{36}$$

$$\nabla \cdot B = 0 \tag{37}$$

$$\nabla \times E = -\frac{\partial B}{\partial t} \tag{38}$$

$$\nabla \times B = \mu_o \left(J + \varepsilon_0 \frac{\partial E}{\partial t}\right) \tag{39}$$

Maxwell’s equations are the foundational equations that govern the electromagnetic physics of plasmas. Equations 36-39 are expressed in their differential form that describe point source situations.

Maxwell’s First Equation, Equation 36, referred to as Gauss’s Law, states that the divergence of an electric field from any point charge is proportional to the strength of the point charge. Similarly the electric flux out of any enclosed surface is proportional to the total charge enclosed by the surface [42].

Maxwell’s Second Equation, Equation 37, or Gauss’s Law for Magnetism, states that unlike an electric charge, the magnetic flux out of any point or surface is equal to zero. This intuitively should make sense while thinking about a magnetic dipole. The magnetic flux out of the north-pole is equal to the flux into the south, resulting in a net flux of the entire magnet equal to zero. This law also states that magnetic monopoles cannot exist, since the flux out of a magnetic monopole would not be equal to zero [42].

Maxwell’s Third Equation, Equation 38, or Faraday’s Law of Induction, states that the curl of any electric field around a point is equal to the negative rate of change of the magnetic field through that point. Three basic conclusions can be drawn from this law. Electric currents create magnetic fields, magnetic fields changing with time will create electric fields, and circulating electric fields will create magnetic fields changing with time [42].

Finally Maxwell's Fourth Equation, Equation 39, or Ampere's Law, states that the curl of a magnetic field around a closed loop is proportional to the electric current flowing through the loop [42].

Single Particle Motion in Plasmas

Plasmas exhibit two types of behavior; individual and collective motion. Plasmas can be evaluated as either a collection of individual particles or as a collective body like a fluid. The behavior of individual charged particles in the presence of electric and magnetic fields govern the particle motion behavior of plasmas [41]. Charged particles moving in a uniform magnetic field, will move around the lines of the magnetic field with a simple cyclotron gyration governed by the Lorentz force equation [6],

$$F = m\frac{d\mathrm{v}}{dt} = q(E + \mathrm{v} \times B). \quad (40)$$

The frequency of this gyration is called the cyclotron frequency [6],

$$\omega_c = \frac{|q|B}{m}. \quad (41)$$

The radius of the particle orbit is called the Larmor radius [6],

$$r_L = \frac{v_\perp}{\omega_c} = \frac{mv_\perp}{|q|B}. \quad (42)$$

A charged particle's velocity axial to a uniform magnetic field will not be changed by the field. Only the direction and frequency the particle orbits around a line of the magnetic field is dependent on the field. The particles will gyrate such that the induced magnetic field created by the particle motion will be opposite to that of the applied field, so ions and electrons orbit in opposite directions [41].

Charged particles moving in space, where both magnetic and electric fields are present, introduces additional complexity to the equations governing the particle motion. When a magnetic field, B, and an electric field, E, perpendicular to B are present, the center of the particle orbit moves. The center of rotation of a charged particle, called a guiding center, will drift in a direction perpendicular to both the E and B fields with a velocity of [41],

$$v_{gc} = \frac{E \times B}{B^2}. \tag{43}$$

As a particle cycles and moves perpendicularly to E, the orbit of the charged particle will be compressed and elongated as the particle moves in the positive E direction (elongation) and negative E direction (compression). This increase and decrease of the particle velocity in opposing directions creates an additional motion drift in the direction of the electric field called the electric field drift [41],

$$v_E = \frac{E[V/m]}{B[\text{tesla}]}. \tag{44}$$

Fluid Motion of Plasmas

When analyzing plasmas as a collective of charged particles, it becomes impractical to analyze the motion of individual particles because of countless collisions and interactions occurring. To simplify the motion calculations, the velocities of particles within a plasma are expressed using velocity distribution functions [6]. The Maxwellian velocity distribution in one dimension is commonly used to define the charge particles in ion thrusters [6],

$$f(\nu) = \left(\frac{m}{2\pi kT}\right)^{1/2} exp\left(-\frac{m\nu^2}{2kT}\right). \quad (45)$$

From this distribution, the average particle energy can be found [6],

$$E_{ave} = \frac{1}{2}kT, \quad (46)$$

along with the average speed per particle [6],

$$\bar{\nu} = \left(\frac{8kT}{\pi m}\right)^{1/2}. \quad (47)$$

The flux of *n* particles along a particular axis can also be calculated [6],

$$\Gamma_z = \frac{1}{4}n\left(\frac{8kT}{\pi m}\right)^{1/2}. \quad (48)$$

The collective motion characteristics of plasmas allow them to be analyzed as fluids of neutral particles and electrical charges [6]. Three forces are assumed to be acting on the plasma, the Lorentz force from the magnetic and electric field; the pressure gradient force; and the collisions transfer of motion. The fluid momentum equation with these three forces is [6],

$$mn\frac{d\mathrm{v}}{dt} = mn\left[\frac{\partial \mathrm{v}}{\partial t} + (\mathrm{v}\cdot\nabla)\mathrm{v}\right] = \underset{\text{(Lorentz)}}{\underline{qn(E + \mathrm{v}\times B)}} - \underset{\text{(Pressure)}}{\underline{\nabla\cdot p}} - \underset{\text{(Collision)}}{\underline{mn\nu(\mathrm{v} - v_o)}}. \quad (49)$$

Equation 49 must be solved for each individual species within the plasma fluid. The velocity of an ion in plasma is determined by both the ion and electron temperatures of the plasma. This velocity is called the ion acoustic velocity. It is solved for in Equation 50 [6],

$$v_a = \sqrt{\frac{\gamma_i k T_i + k T_e}{M}}. \tag{50}$$

Collisions

Ion thruster ionization is driven by collisions. The flow of ions through a sliced section with thickness *dx* of plasma is defined by the following flux equation [6],

$$\Gamma = \Gamma_o \exp(-n_a \sigma x) = \Gamma_o \exp\left(-\frac{x}{\lambda}\right). \tag{51}$$

The mean free path or how far a particle will travel in the plasma without a collision occurring. The mean free path helps define all other collision parameters. The mean time between collisions and the collision frequency are defined by Equation 52, using the average of the Maxwellian velocities [6],

$$\upsilon = \frac{1}{\tau} = n_a \sigma \bar{v} = \frac{\bar{v}}{\lambda}. \tag{52}$$

Collision and Ionization in RF Discharges

During the ignition of an RF ion thruster, electrons must collide with neutral propellant atoms to begin the discharge. RF discharges induce an oscillating electric field. Free electrons move at too high of a velocity to see this oscillation and can traverse the entire length of the discharge chamber many times over within a half-cycle of the RF field. Electrons within an RF discharge therefore experience a DC electric field and are accelerated in one direction since they travel the length of the discharge chamber before the polarity of the RF signal changes. The probability of an electron colliding with a neutral particle is given by the following equation, where x is the length of the discharge chamber [6],

$$P_{coll} = 1 - exp^{-x/\lambda} = 1 - exp^{-n_o \sigma x}. \tag{53}$$

Neutral density can be converted into pressure. The relationship between ionization probability and pressure, in pascals, within the discharge chamber can then be obtained, [6],

$$P_{Pa} = \frac{-k\, T_{Kelvin}}{\sigma\, x} \ln(1 - P_{coll}). \tag{54}$$

Plasma Sheaths

Plasma boundaries are the physical region where energy and particles enter and exit the plasma. To maintain particle balance or meet electrical conditions, the plasma will establish potential and density variations along the boundary. These potential and density variations will define how the plasma interacts with the physical boundaries of the thruster. The boundary region of the plasma is called the sheath [6]. This potential barrier forms to confine the mobile species within the plasma electrostatically, balancing the flux of ions and electrons that the reach the wall or physical boundary enclosing the plasma. The thickness of the sheath is expressed by the characteristic Debye length [6],

$$\lambda_D = \sqrt{\frac{\varepsilon_0 k T_e}{n_o e^2}}. \tag{55}$$

If a spherical test charge with a small potential was inserted into a quasi-neutral plasma, a potential boundary would form around the test charge. The potential within the plasma would fall, dependent on distance r away from the test charge by the following equation [6],

$$\phi = \frac{q}{4\pi \varepsilon_o r} exp\left(-\frac{r}{\lambda_D}\right). \tag{56}$$

The characteristic Debye length does not equate to the distance from the test electrode, where the potential within the plasma is negligible [6], rather in Equation 56, if the radial distance away from a test charge is equal to the Debye length, then the potential at that point would be, [6]

$$\phi = \frac{e}{4\pi\varepsilon_o r}\exp(-1) = \frac{e}{4\pi\varepsilon_o r} * .3678 = \frac{5 * 10^{-10}}{\lambda_D}[V]. \tag{57}$$

Outside of idealized situations, normal sheaths are several Debye lengths thick [6].

For situations where the potential difference between the electrode and plasma is on the same order of magnitude as the electron temperature, a region called the pre-sheath develops [6]. The pre-sheath is a region between the larger plasma body and the sheath boundary, where the ions of the plasma fall from the reference potential at the center of the plasma to the potential at the sheath boundary. This potential drop is called the pre-sheath potential [6]. This potential drop results from the fact that the ions must enter the sheath with enough energy to produce stable sheath behavior [6]. To create velocities of at least $\sqrt{kT_e/M}$, where M is the mass of the ion, a potential drop of $T_e/2$ is seen across the pre-sheath region. This velocity, called the Bohm velocity, is equal to the ion acoustic velocity and is found using Equation 50. From this potential drop the conditions of the ions as they arrive at the sheath edge can be calculated using the conservation of energy [6],

$$\frac{1}{2}M\nu_o = e\phi_o. \tag{58}$$

Once the ions pass the sheath edge, their velocity can be calculated in the following way, with ϕ being the plasma potential at a point within the sheath [6],

$$\nu = \sqrt{\frac{2e}{M}}\,[\phi_o - \phi]^{1/2}. \tag{59}$$

The ion density in the sheath can be calculated using the following equation, where n_o is the density far from the edge of the plasma [6],

$$n_{i,s} = n_o\sqrt{\frac{\phi_o}{\phi_o - \phi}}. \tag{60}$$

The current of ions leaving the plasma sheath to a collection area at the sheath boundary, called the Bohm current can then be calculated as [6],

$$I_i = \frac{1}{2} n_o e \sqrt{\frac{kT_e}{M}} A. \tag{61}$$

If the potential across a sheath boundary is too large for a majority of electrons to cross, the current flux out of the sheath is defined by the fixed potential and the Boltzmann relation, where *d* is the thickness of the sheath and *V* is the potential drop across it [6],

$$J_i = \frac{4\varepsilon_o}{9}\left(\frac{2e}{M}\right)^{1/2}\frac{V^{3/2}}{d^2}. \tag{62}$$

When using experimental probes in plasmas, the sheath-probe interactions must be accounted for to gain any useful information from probe measurements.

Experimental Probes

To analyze the plasma plume of the BIT-1 two experimental probes, a Faraday probe and a Langmuir probe, were used. This section will be devoted to describing how both of these probes function and what information about the plasma plume can be obtained from each. Both of these probes were directly inserted into the plasma plume to measure its properties. The presence of the probe in the plasma inherently changes the plasma in proximity to the probe.

Langmuir Probes

Langmuir probes in their simplest description are particle flux probes. To operate a Langmuir probe a sweeping voltage is applied to an electrode inserted into a plasma. The current drawn by the probe is measured and used to determine plasma properties. A typical Langmuir probe current-voltage trace is shown in Figure 11. Langmuir probes can be any shape [43]. All the Langmuir probe data in this thesis was measured using a cylindrical geometry. All discussion and equations presented will focus on this type of geometry.

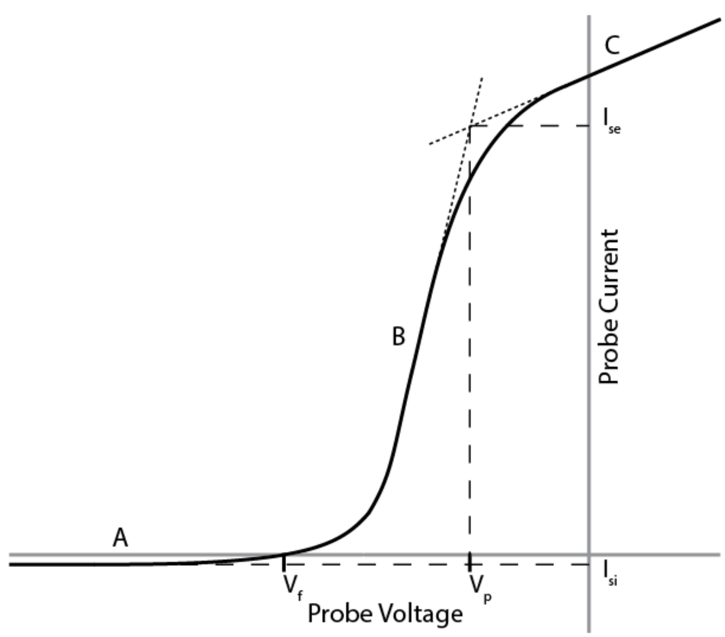

Figure 11: Typical Langmuir Probe Trace [43]

There are several plasma characteristics that can be obtained with a Langmuir probe, the first of which is the plasma's floating potential, V_f. If an isolated electrode was placed within a plasma, a charge would build up on the electrode to make the net electrical current seen by the electrode zero [43]. This potential to which the electrode floats is called the plasma floating potential. Looking at section A in Figure 11, adapted from "Principles of Plasma Diagnostics" by Hutchinson [43], the floating potential of the plasma is the voltage where the current collected by the probe is zero, meaning $J_e = J_i$ [43]. Below the floating potential, the probe will be collecting current from primarily the plasma ions. This current will be approximately constant and defined as half of Equation 48; since ions are only flowing into the probe and not out of it. This constant current is defined as the ion saturation current, I_{si} [43].

As the probe voltage is increased past the floating potential the probe begins to collect plasma electrons but is still negative compared to the surrounding plasma, Section B. The potential of the plasma without a probe present is called the plasma potential, V_p. The plasma potential is defined on a Langmuir probe sweep as the voltage where the collected current by the probe is equal to the electron current [44]. At voltages higher than the plasma potential, the probe is collecting its maximum number of electrons. This is because all of the electrons contacting the probe will be collected. This current is called the electron saturation current, I_{se}. In a Langmuir probe trace this is where the upper bend or elbow occurs [43]. If the probe continues to increase in voltage, the collected current will increase at a constant rate as the sheath expands, effectively increasing the collection area of the probe [43].

A Langmuir probe's effect on a plasma as well as the plasma's effect on the probe's measurements can be calculated. As explained earlier a charged electrode will induce a potential change within the plasma, as represented by the Debye length, Equation 55. Collisions within the plasma can have an effect on the probe measurements.

If the mean free path within the plasma is much greater than the length of the probe, it can be assumed that the measurements from the probe will be unaffected by collisions [43]. The numerical parameter relating the mean free path to the probe length is called the Knudsen number, [44],

$$K_n = \frac{\lambda}{r}. \tag{63}$$

Assume a Langmuir probe is held at a constant negative potential within a plasma. A sheath is formed around the probe as it is attracting ions and repelling most electrons. Assume that all particles that reach the probe are absorbed by the probe and are removed from the plasma. As mentioned in previous sections particle motion within a plasma can be considered a distribution. For the electrons within the plasma, the lower end of the energy distribution will be reflected by the potential of the probe. Only the highest energy electrons will have enough velocity to break through the potential barrier and reach the probe. This velocity limit is called the cutoff velocity [43].

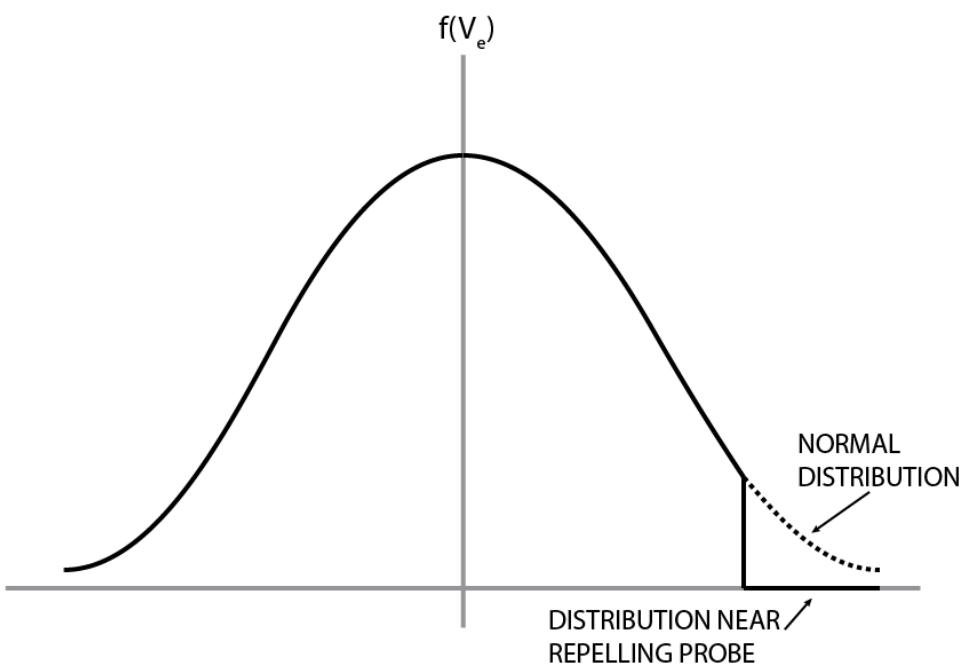

Figure 12: Electron Distribution Near a Negatively Biased (Repelling) Probe [43]

If all the electrons in a plasma are reflected and none are absorbed then the electron density at position x away from the probe would be [43],

$$n_e(x) = n_\infty exp\{eV(x)/T_e\}. \quad (64)$$

When evaluating the electron density, with the distribution in Figure 12 close to a probe adapted from "Principles of Plasma Diagnostics" by Hutchinson [43], the following equation is used [43],

$$n_e(x) = n_o \exp\left\{\frac{eV(x)}{T_e}\right\}\frac{1}{2}\left(1 + erf\{[V(x) - V(0)]e/T_e\}^{1/2}\right). \quad (65)$$

Where the error function is [43],

$$\mathrm{erf}(t) \equiv \frac{2}{\sqrt{\pi}}\int_0^t e^{-y^2}. \quad (66)$$

Ion saturation current is determined by the expansion of sheath size. This relationship in sheath size to probe size and probe voltage is determined in the following way [43],

$$A_s \approx \left(A_p\left(1 + \frac{x_s}{r}\right)\right). \quad (67)$$

The sheath thickness is determined by the following equation [43],

$$\frac{x_s}{\lambda_D} = \frac{2}{3}[2\exp(1)]^{1/4}\left[\left(\frac{-eV_o}{T}\right)^{1/2} - \frac{1}{\sqrt{2}}\right]^{1/2}\left[\left(\frac{-eV_o}{T}\right)^{1/2} + \sqrt{2}\right]. \quad (68)$$

The total current drawn by the probe is given by the Bohm value [43],

$$I_i = n_\infty e A_p\left(\frac{T_e}{m_i}\right)^{1/2}\left[\frac{1}{2}\left(\frac{2m_i}{\pi m_e}\right)^{1/2}\exp\left(\frac{eV}{T_e}\right) - \frac{A_s}{A_p}exp\left(-\frac{1}{2}\right)\right]. \quad (69)$$

This current is the current measured by a probe. When the voltage is swept, measuring plasma conditions become more complex [43].

Orbital Motion Limited Analysis

To obtain a full exact solution for the number density of ions, further analysis is required. The type of analysis performed will depend on the plasma's parameters compared to the probe. If the Debye length of the probe is greater than the radius of the probe, the sheath approximations will not be valid [43]. Instead, this type of situation will be dominated by orbital effects of the plasma. The probe is said to be orbital motion limited (OML) because not all particles that enter the sheath will be collected by the probe [44]. Laframboise developed techniques to analyze plasma probe data in such situations [45], [46]. By assuming that a cylindrical probe is instead measuring a stationary, cold, collisionless plasma, the sheath dimensions can then be assumed to change as the probe potential increases, altering the collected ion current. The OML method can be applied to plasmas where $r/\lambda_D < 3$ [44].

The floating potential is still the voltage applied to the probe where the collected current is equal to zero. This is relatively straight forward to solve for, and it can be accomplished by using Equation 69 and setting the current equal to zero [44],

$$\frac{eV_f}{T_e} = \frac{1}{2}\left[ln\left(2\pi\frac{m_e}{m_i}\right) - 1\right]. \tag{70}$$

Voltage measurements below the floating potential, section A in Figure 11, are used to determine the ion number density. In the analysis, a portion of section A is used. The slope of the ion current squared over the bias voltage is used to determine the ion number density, demonstrated in the following equation [44],

$$n_{i,OML} = -\frac{1}{A_p}\sqrt{\left(\frac{d(I_i^2)}{dV}\right)\frac{2\pi M_i}{1.27e^3}}. \tag{71}$$

In section B from Figure 11, the electron temperature is calculated by taking the inverse slope of the natural log of the electron current versus probe voltage [44],

$$T_e = \frac{V_2 - V_1}{\ln(I_2/I_1)}. \tag{72}$$

The plasma potential can then be found by [44],

$$V_p = \ln\left(\sqrt{\frac{m_e}{m_i}}\right) kT_e + V_f. \tag{73}$$

Thin Sheath Method

In situations where r/λ_D>10, the thin sheath method is instead used [44]. In thin sheath analysis, the orbital motion of the particles can be ignored since the probe is significantly larger than the Debye length of the plasma. In the thin sheath method the electron temperature of the plasma is calculated in the same manner as OML using Equation 72. The ion saturation current is measured as the average of the current values in section A of Figure 11.

The next step in the process is an iterative one to find the Debye length. First, the ion number density is calculated using the probe area as the initial A_s [44],

$$n_{i,thin} = \frac{\mathrm{I}_{se}}{0.61 A_s e} \sqrt{\frac{M_i}{T_e}}. \tag{74}$$

The Debye length is then calculated using Equation 55 by assuming quasi-neutrality, n_e=$n_{i,thin}$. A new sheath area is then calculated using Equations 67 and 68, and a new ion number density is calculated based on the new sheath area. This process repeats until the sheath area converges. The ion number density at this converged point accounts for sheath expansion [44]. The plasma potential can then be calculated with Equation 73.

Faraday Probes

Faraday probes are used to directly measure the ion current and current density within a plasma. Faraday probes operate by equally negatively biasing two concentric electrodes: an inner collector and an outer ring guard, and measuring the current that is seen by the inner collector. The concentric electrode creates a uniform sheath across the entire collector surface repelling electrons. For the experiments performed, a nude Faraday probe was used. The back of the probe's inner collector was coated with alumina and did not contribute to the collected current.

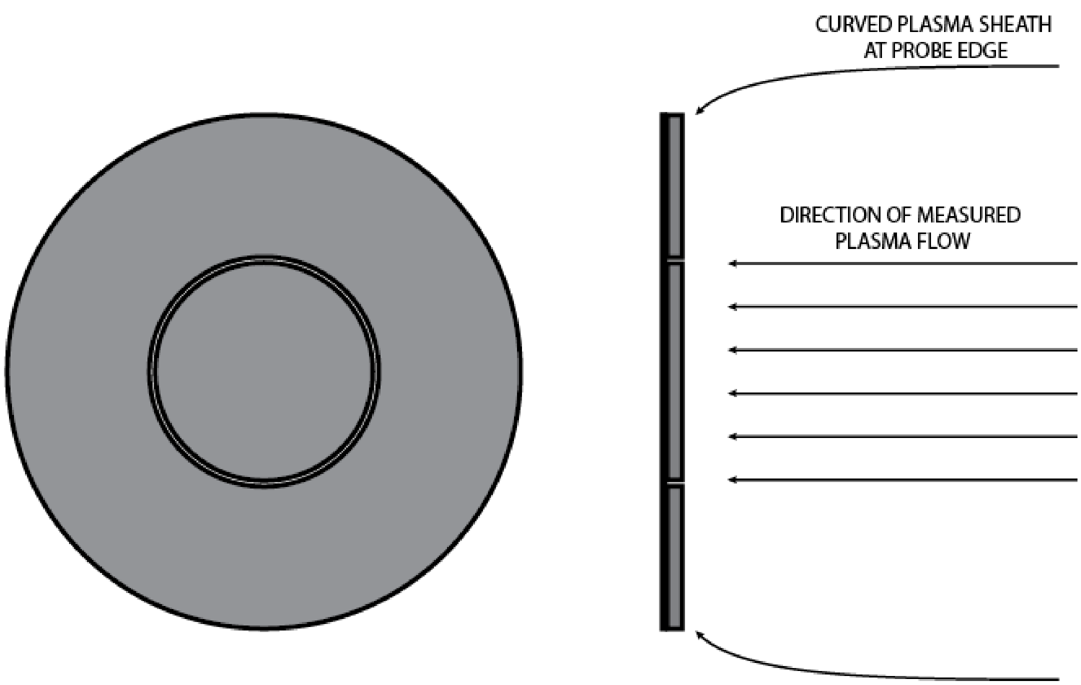

Figure 13: (Left) Front and (Right) Side View of a Nude Faraday Probe [47]

As shown in Figure 13, adapted from Low-Power Magnetically Shielded Hall Thrusters by Conversano [47], the ring guard is necessary to prevent any curving within the measured sheath. Without the ring guard, the collector would measure artificially higher currents due to the bending within the sheath at the electrode's edge. The collected current is then divided by the surface area of the exposed inner collector to calculate the current density of the plasma ions, J_i [48],

$$J_i = \frac{I_{probe}}{A_{probe}}. \tag{75}$$

CHAPTER III

EXPERIMENTAL SETUP AND DIAGNOSTICS

The data reported in this document were collected using two different experimental setups in two different locations. Analysis of the BIT-1 plume using a Langmuir probe was conducted in Kalamazoo, Michigan, at Western Michigan University in the Aerospace Laboratory for Plasma Experiments (ALPE). A Faraday probe and a beam target were used at the Jet Propulsion Laboratory (JPL) in Pasadena, California. This section will focus on the description of both experimental setups.

Vacuum Chambers

The vacuum chamber, referred to as 'Little Green', shown in Figure 14, at JPL is 36 inches in diameter and 84 inches long. It is equipped with two 10-inch CTI cryopumps that produce a total pumping speed for xenon of 1250 l/s.

Figure 14: Little Green Vacuum Chamber at JPL

The chamber at Western Michigan University, shown in Figure 15, the 'ALPE Chamber', is 40-inches in diameter and 69.25-in long. It uses a single Leybold Turbovac 1100 C with an argon pumping speed of 980 l/s and 1050 l/s for nitrogen [49].

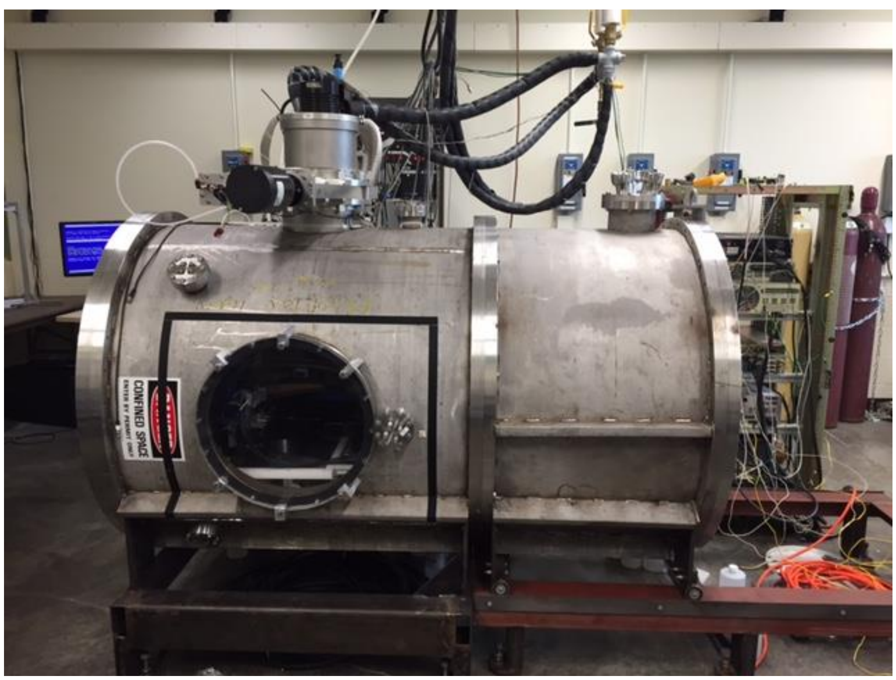

Figure 15: The Western Michigan University ALPE Chamber

BIT-1 Thruster

The Busek Ion Thruster–1 or BIT-1, is an RF ion thruster designed by Busek Co. Inc. The thruster operates at around 10 W of RF power and can produce 100 µN of thrust [50]. To supply sufficient power to the thruster, three power feedthroughs were used: two high voltage feedthroughs for the screen and accel grids and an SMA feedthrough for the RF power. The block diagram describing the power inputs of the thruster is shown in Figure 16.

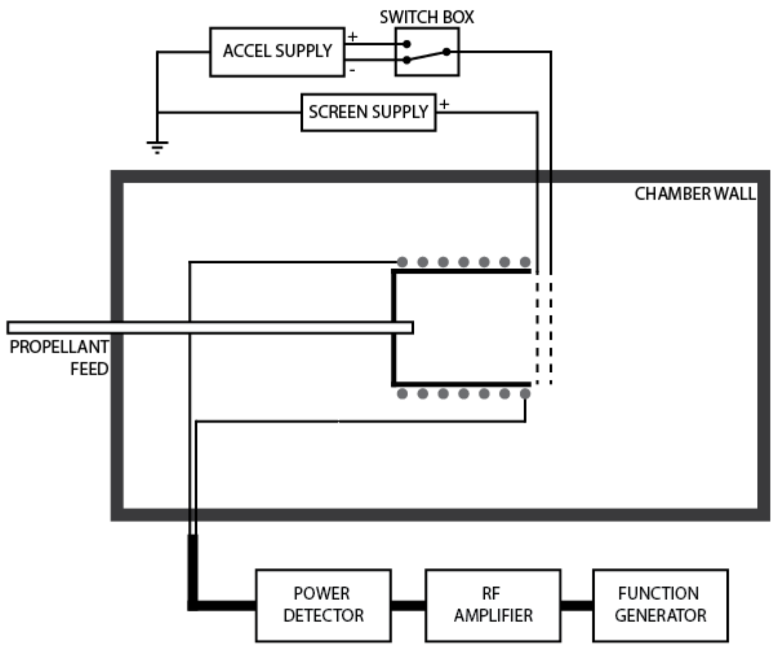

Figure 16: Circuit Diagram of BIT-1

RF Power

A Tektronix AFG2021 function generator was used to create an RF signal with a frequency of approximately 8.5 MHz. This frequency selected was the RF frequency required to create the lowest reflected or reverse power possible, indicating a high power coupling efficiency between the coil and the plasma. To determine this frequency at

ALPE, an HP 8935 CDMA Spectrum Analyzer and a return loss bridge were used. While at JPL, an Agilent Technologies E5061A Network Analyzer was used. The analyzer was hooked up to the thruster circuit in place of the function generator and the RF amplifier. A sweeping RF signal was applied to the thruster circuit. The forward and reflected powers were measured at each frequency. The frequency with the lowest measured reflected power was selected as the operating frequency. This process was repeated every time the thruster was started.

During thruster operation, the selected RF signal was amplified by 40 dB, with an ENI 603L Amplifier. After the signal was amplified, the power level of the signal was measured using a bi-directional coupler, ZFBDC20-61HP-S+ and two power detectors, ZX47-40-S+ from Mini Circuits, as shown in Figure 17.

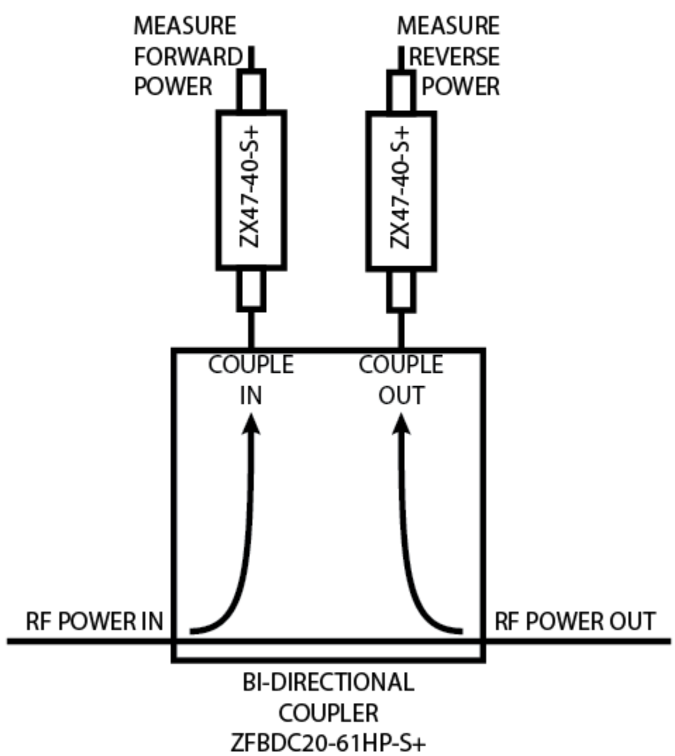

Figure 17: Bi-Directional Coupler Diagram

The measured forward and reverse power measurements were then sent to an NI USB-6366 data acquisition system (DAQ) and recorded.

Acceleration and Screen Grids

To ignite the RF plasma discharge, the polarity of the accel grid had to be switched from negative to positive to allow seed electrons from the neutralizer cathode into the discharge chamber. This was accomplished by using two Gold Control DC solid state relays inside a switching box, shown in Figure 18. After the relay, a 100-Ω resistor was placed into the electrical circuit to measure the current to the accel grid with a Fluke 114 Multimeter. The current and voltage for the screen and negative accel grid supply were monitored and recorded with the DAQ using LabVIEW.

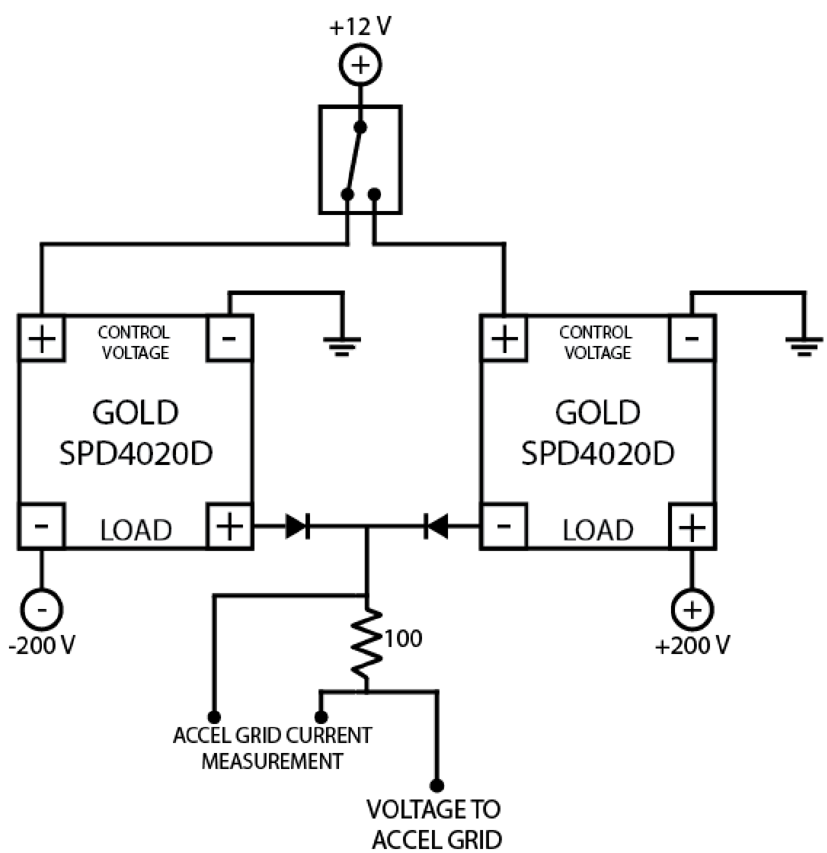

Figure 18: Accel Grid Switching Box Circuit Diagram

Propellant Feed

The Xenon propellant feed to the thruster and cathode were controlled with Alicat Scientific mass flow controllers limited to 10-sccm and 100-sccm, respectively. A diagram of the thruster and cathode propellant feed systems at ALPE is shown in Figure 19 and a photo of the propellant feed used at JPL is shown in Figure 20.

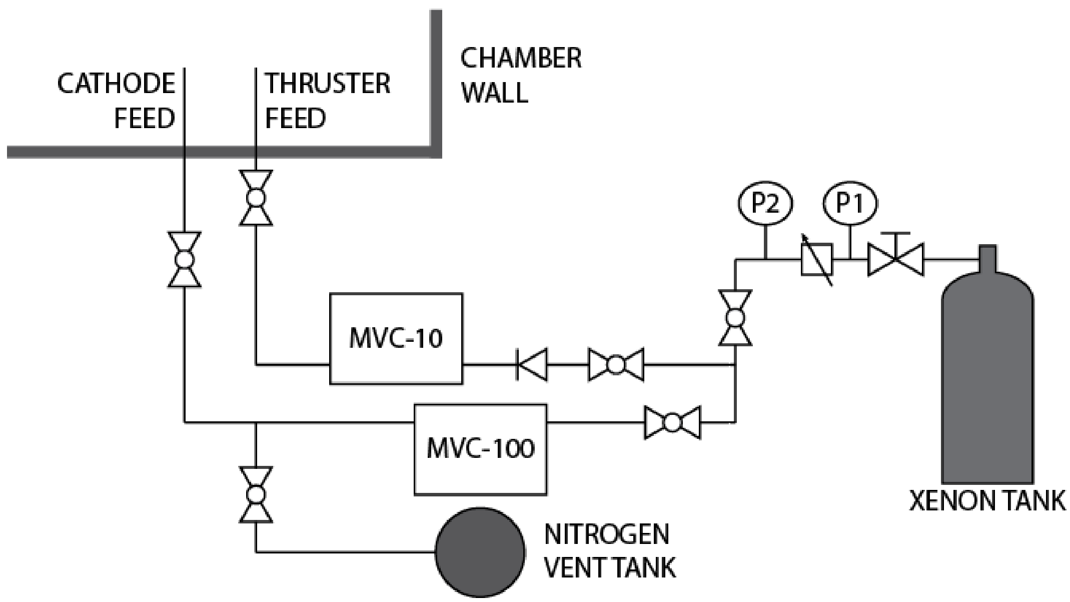

Figure 19: BIT-1 and Cathode Propellant Feed Diagram used at ALPE

Figure 20: Propellant Feed System used at JPL

Neutralizer Cathodes

For each experimental setup, different hollow cathodes were used to provide seed electrons and to neutralize the thruster beam. At JPL a BaO cathode developed for the 25-cm XiPS© thruster [51] was used, and at ALPE an 1/8" BaO cathode developed by E Beam, Inc. was used. Figure 21 shows both experimental setups with their respective cathodes. The left image is the experimental setup at JPL and the right image is the experimental setup at ALPE.

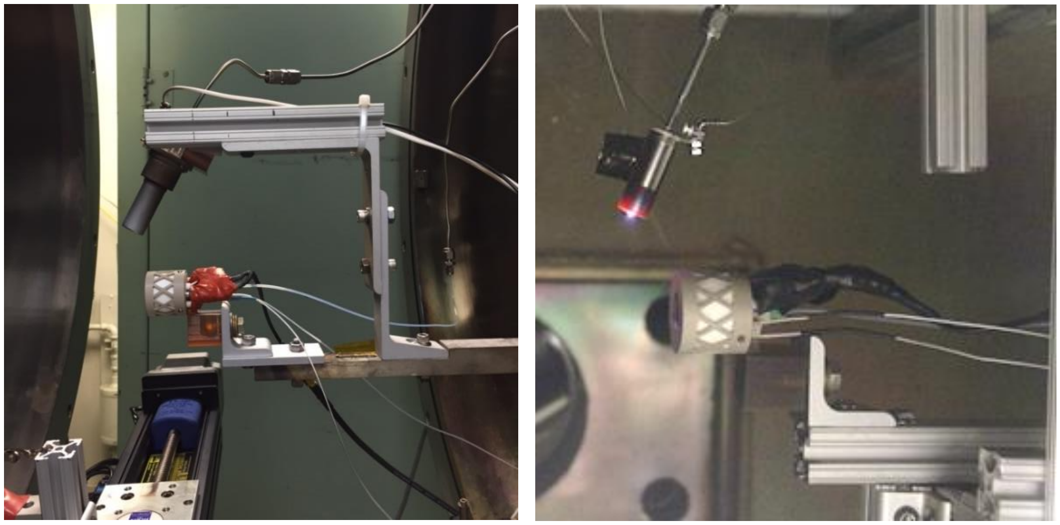

Figure 21: (Left) JPL Experimental XiPS Cathode and BIT-1 Configuration, (Right) ALPE Experimental E Beam Cathode and BIT-1 Configuration

Experimental Probe Setup

JPL Experimental Setup

At JPL, a Faraday probe with a collector diameter of 2.75-mm and a ring guard with an outer diameter of 6.3-mm placed on an X-Y motion stage system was used. Behind the Faraday probe was a 30.48-cm molybdenum beam target used to collect the total beam current of the thruster to ground. The molybdenum beam target was placed at two locations; 41.275-cm away from the thruster when the Faraday probe was present, and 25.4-cm away from the thruster when the Faraday probe was not in the chamber. All of the beam target data presented in this thesis were collected with the molybdenum target in the 25.4-cm away configuration as seen in Figure 22.

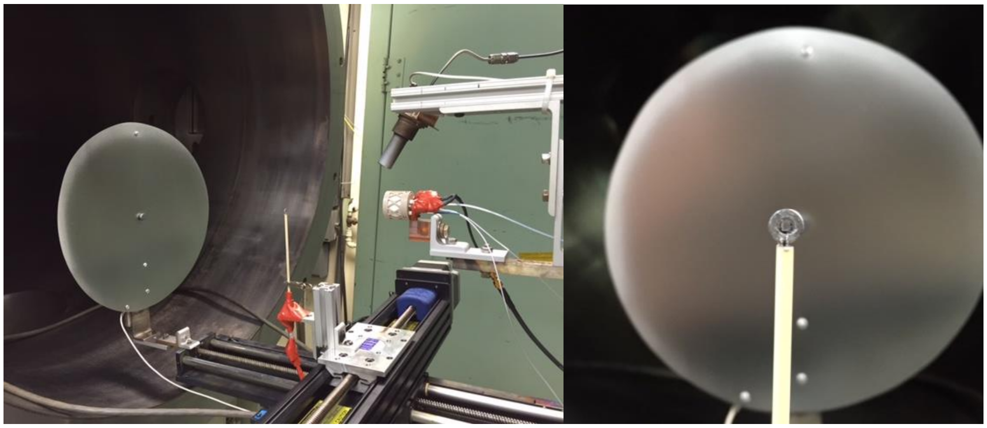

Figure 22: (Left) JPL Experiment Setup with Beam Target and Faraday Probe, (Right) Close Up of Faraday Probe and Beam Target Used In Experiments at JPL

The XiPS© cathode was placed in two slightly different locations for each of these probe configurations, as shown in Figure 22. First, with just the beam target installed, the XiPS© cathode was positioned above the thruster 5.58-cm, laterally off axis 1.59-cm and 1.27-cm in front of the thruster at a 60° angle. All distances are measured from the center of the cathode orifice to the center of the thruster face. When the Faraday probe and motion tables were added the height of the cathode above the thruster was reduced to 5.08-cm to increase the number of seed electrons from the cathode into the discharge chamber during startup.

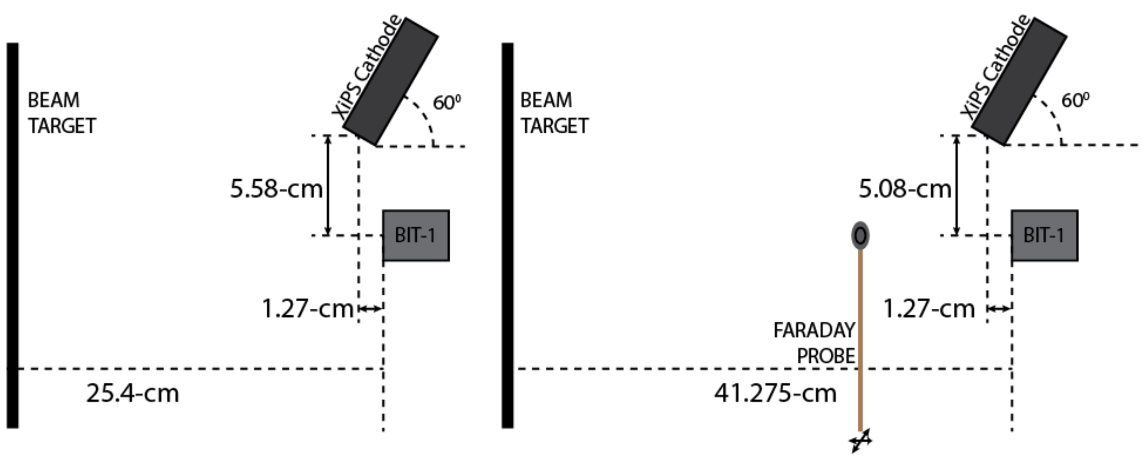

Figure 23: Position of the XiPS Cathode with Respect to the BIT-1 with (Left) Only The Beam Target, and (Right) the Beam Target and Faraday Probe Present Downstream of the BIT-1

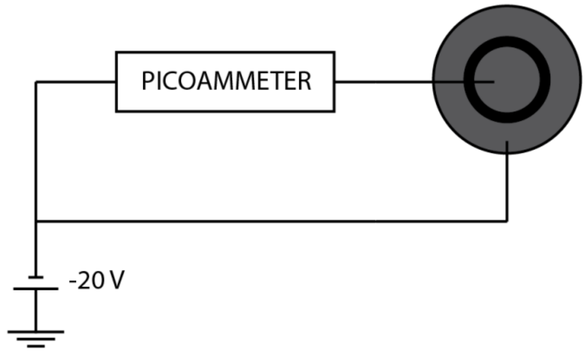

Figure 24: Faraday Probe Circuit Diagram

To operate the Faraday probe shown in Figure 23 and Figure 24, -20 V was applied to both the inner and outer electrodes. The current through the center collector to ground was measured with a Picoammeter and recorded. This current was divided by the area of the inner collector to determine the ion current density at each measurement location. The beam target measured the total current from the plasma to ground as shown in Figure 25. Faraday probe data tends to be prone to facility effects, specifically on the edges of the plume closer to the walls of the vacuum chamber [48]. Background pressure, charge exchanges, electron bombardment and secondary electron emission can also effect Faraday probe measurements [52]. Therefore, all Faraday probe measurements were normalized to the peak measured current.

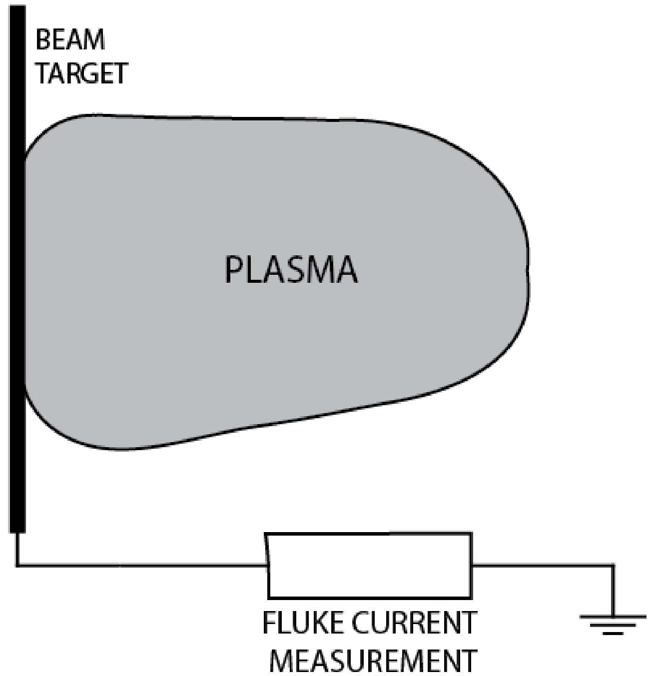

Figure 25: Beam Target Circuit Diagram

ALPE Experimental Setup

In the laboratory testing performed at ALPE, a Langmuir probe with a diameter of 0.23-mm and a length of 6.24-mm was mounted to a rotation table. As seen in Figure 26, the rotation table was attached to an X-Y axis motion stage system positioned in front of the thruster. The cathode was mounted directly above the thruster 5.08-cm and at an angle of 70°. The thruster was pointed axially down the chamber, attached to a fixed rotation point, and connected to a linear stage allowing the thruster to be rotated and simulate thrust vectoring.

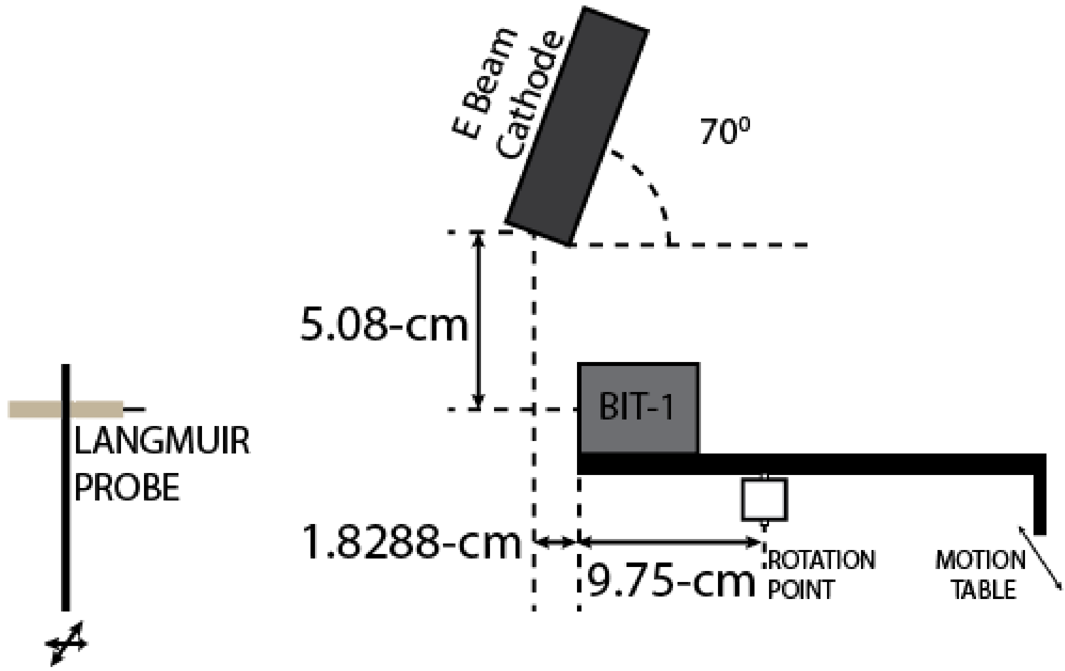

Figure 26: ALPE Experimental Setup with BIT-1 thruster, E Beam cathode, and Langmuir Probe

Figure 27 shows the method used to achieve simulated thrust vectoring. The BIT-1 was tested at three different vector angles, 0°, 2.5° and 5°.

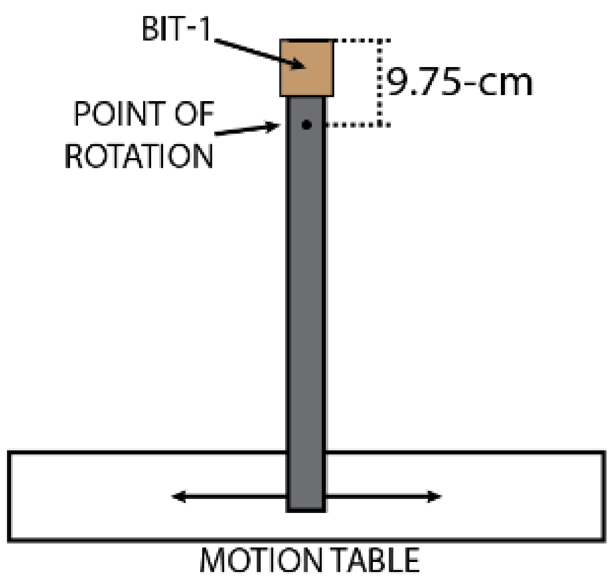

Figure 27: Top View of Thrust Vectoring Experimental Setup

The point of rotation was 9.75-cm behind the face of the thruster. Because of this at the 2.5° and 5° conditions the center of the thruster shifted laterally, 0.42-cm, and 0.85-cm respectively.

To operate the Langmuir probe setup shown in Figure 26, the circuit shown in Figure 28 was used; all data were collected and recorded using LabVIEW. A saw tooth waveform created by the DAQ was amplified by a bipolar BOP 500M power supply and sent to the Langmuir probe circuit box diagramed in Figure 28. The voltage and resultant current from the probe were measured and recorded using LabVIEW.

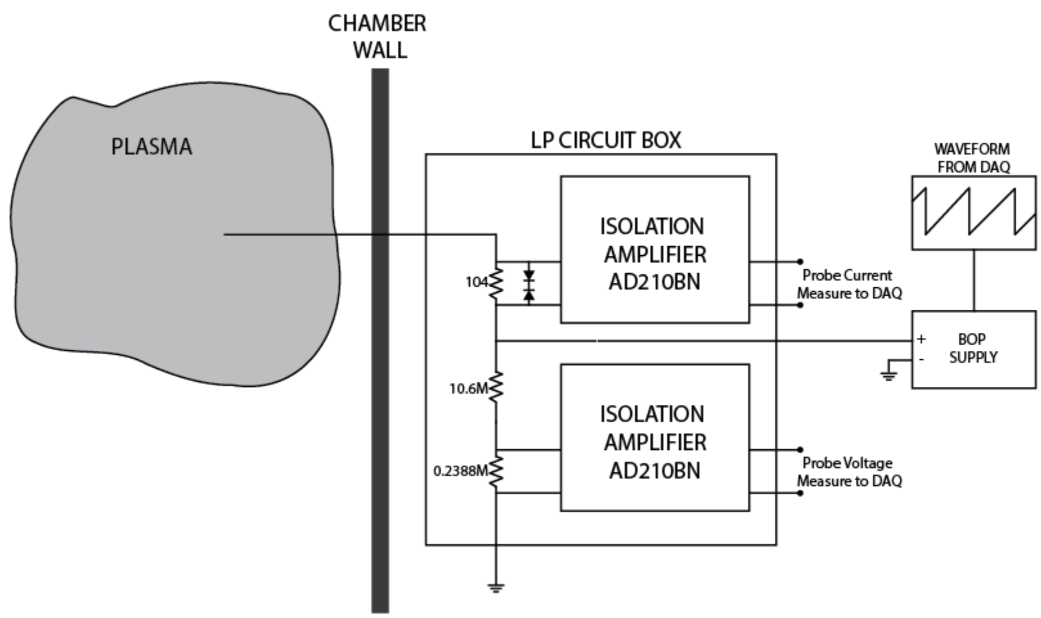

Figure 28: Langmuir Probe Circuit Diagram

Absolute number density measurements of Langmuir probes are traditionally given error estimates of around 50% [43] and 20% for electron temperature [53]. While potential measurements tend to be much less and vary only by several volts [48], [54].

Magnetic Field Modeling

Computer modeling of the BRFIT-1, an early version of the BIT-1, was completed using the finite element analysis and simulation software COMSOL Multiphysics 4.4. An RF coil, the approximate dimensions of the BRFIT-1 thruster coil, was placed within a 3U CubeSat-sized platform with four permanent magnets. The permanent magnets were designed to approximate the magnetic field of the passive stabilization system used on KySat-1 [13].

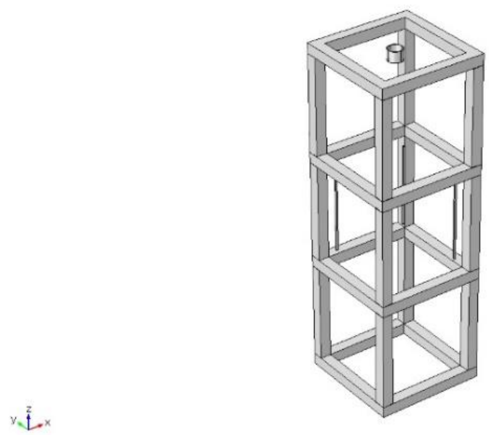

Figure 29: Geometric Model of BRFIT-1 and 3U CubeSat System created in COMSOL

The purpose of this model was to demonstrate the potential for interactions between the magnetic field of the thruster coil and the permanent magnets of a passive attitude stabilization system. The geometric model shown in Figure 29 of a 3U CubeSat was created in COMSOL. The dimensions of the CubeSat skeleton were 30-cm × 10-cm × 10-cm with the cross section of the ribs being a 1-cm × 1-cm square.

A hollow cylinder was positioned within the model at one end of the structure to simulate an RF coil. The coil was assumed to have 10 turns and excited with a 22.5-V signal oscillating at 8-MHz. Four permanent magnets were placed at three different positions within the CubeSat structure to simulate 1U, 2U and 3U platforms. With the magnets placed in each of the structure's four corners ±35-mm from the centerline. The magnets were assigned a total magnetic dipole of 0.5884-Am^2 [13]. This was accomplished using COMSOL's Magnetic Fields physics package. The calculations were completed with two successive studies, a Coil Geometry Analysis and then a Frequency Domain study. The result created a simulation of the interaction between the magnetic field of the thruster and permanent magnets at the three different conditional positions.

CHAPTER IV

EXPERIMENTAL RESULTS

Faraday Probe Measurements

Current Density Measurements

This section discusses the data collected with a Faraday probe, using the JPL experimental setup. Figure 30 shows the BIT-1 operating in Little Green at JPL.

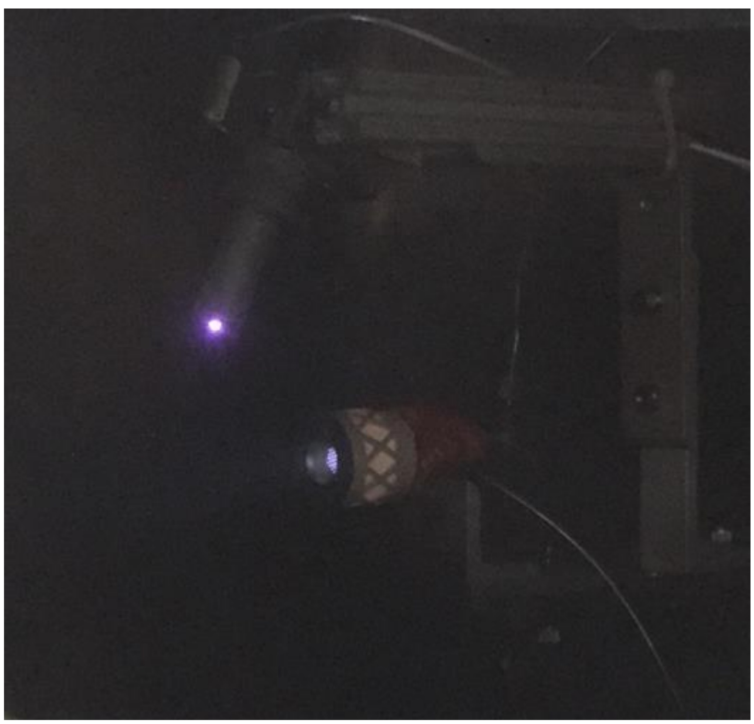

Figure 30: BIT-1 Operating in JPL Facility with XiPS Cathode

To operate the Faraday probe, both electrodes were biased to -20-V. The current to the inner electrode was then divided by the exposed surface area to calculate the ion current density (A/m^2). The exposed surface area of the probe was dependent on the position of the probe. As shown in Figure 31, the further off-axis the probe was positioned from the thruster, the smaller the adjusted probe area became.

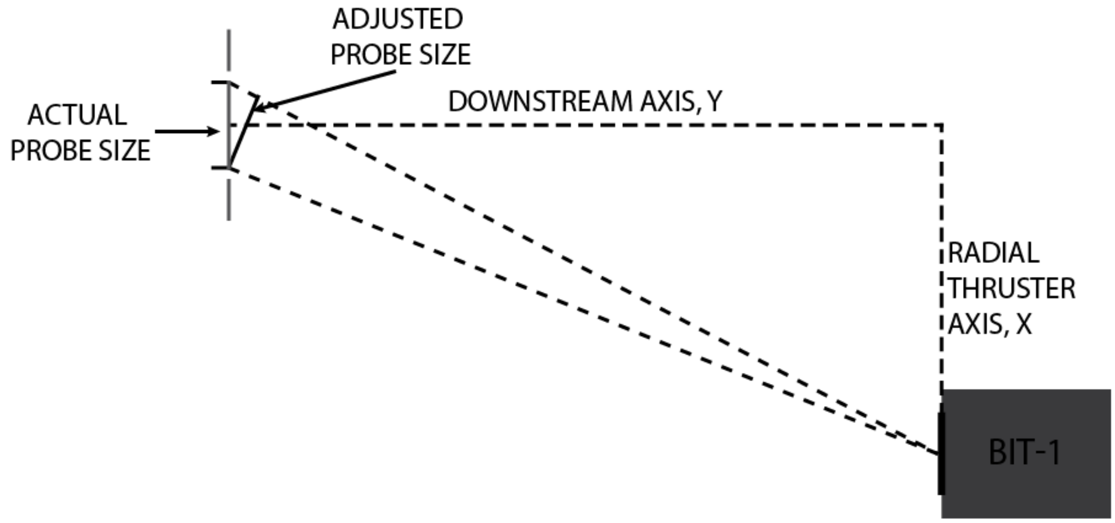

Figure 31: Diagram of Faraday Probe Surface Area Correction

The corrected surface area of the probe, dependent on its position, can be defined by the following equation,

$$A_{corrected} = \pi \left(\frac{D_{probe} \cos\left(\tan^{-1}\left(\frac{X}{Y}\right)\right)}{2} \right)^2 . \qquad (76)$$

The measured current was then divided by the corrected area, and the ion current density for that position was obtained.

$$J_i = \frac{I_{measured}}{A_{corrected}} \qquad (77)$$

Using this method of area correction, a more accurate reading of the current density can be obtained. As current was measured farther off-axis from the BIT-1's centerline, small currents were exaggerated, and the results were distorted. Before the area correction was performed, each measured current value was compared to the current measured at the centerline of the thruster at the same Y position, (referencing Figure 31). If the current measured at the far radial position was less than 5% of the maximum current measured at the same downstream distance, the probe was assumed to be out of the thruster plume, negating the current density measured at that position. This process reduced the extent to which small measured currents at far radial positions, produced by noise or facility effects, were exaggerated by the area correction in Equation 76. The measured current densities were then normalized to the maximum measured current density. The data were graphed using Tecplot 360 and displayed in Figure 32. The conditions of the thruster, cathode, and chamber during these measurements are shown in Table 1.

Table 1: Thruster and Cathode Conditions for Faraday Probe Data

		Start	End
Screen Voltage	**V**	1600	1600
Screen Current	**A**	1.55	1.5
Accel Voltage	**V**	-200	-200
Accel Current	**mA**	0.51	0.49
RF Freq	**MHz**	8.495	8.495
Forward Power	**W**	8.16	8.16
Reverse Power	**W**	1.345	1.355
Thruster Flow	**sccm**	0.19	0.19
Keeper Voltage	**V**	17.5	17.2
Keeper Current	**A**	1.3	1.3
Cathode Flow	**sccm**	6	6
Pressure	**Torr**	3.03E-05	3.03E-05

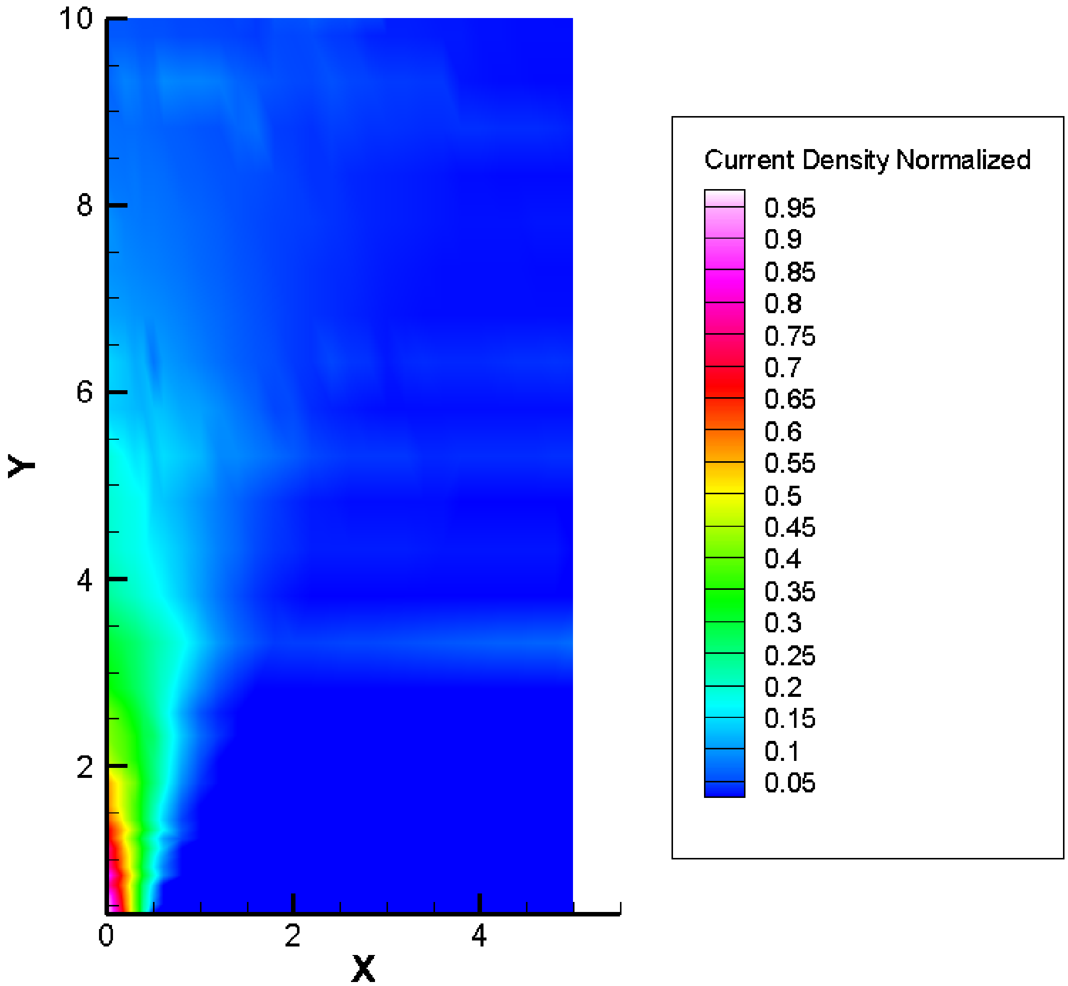

Figure 32: Faraday Probe Data, X and Y Axis are Measured in cm

Beam Divergence Calculations

Figure 33 is a collection of Faraday probe sweeps at varying downstream positions, these values were normalized compared to the maximum measured current. As shown in the data, the peak intensity of the current decreases, and the current profile widens as the probe is moved axially away from the thruster.

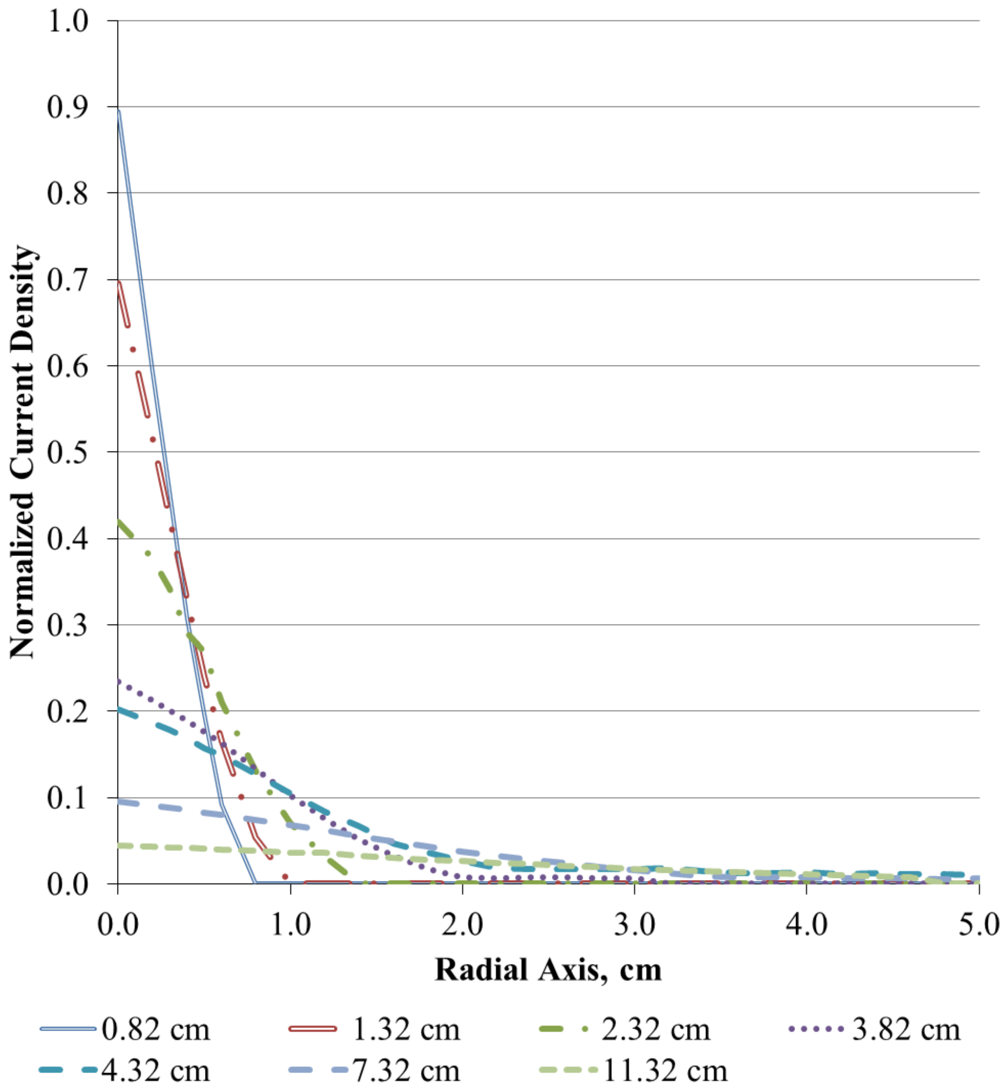

Figure 33: Faraday Probe Data Sweeps at Varying Positions Downstream of the BIT-1

The probe currents were integrated over a selection of probe sweeps. The angle that encompassed 95% of the beam is considered the edge of the thruster exhaust. This angle is the thruster's beam divergence angle [55]. The integration of these current density sweeps is plotted in Figure 34.

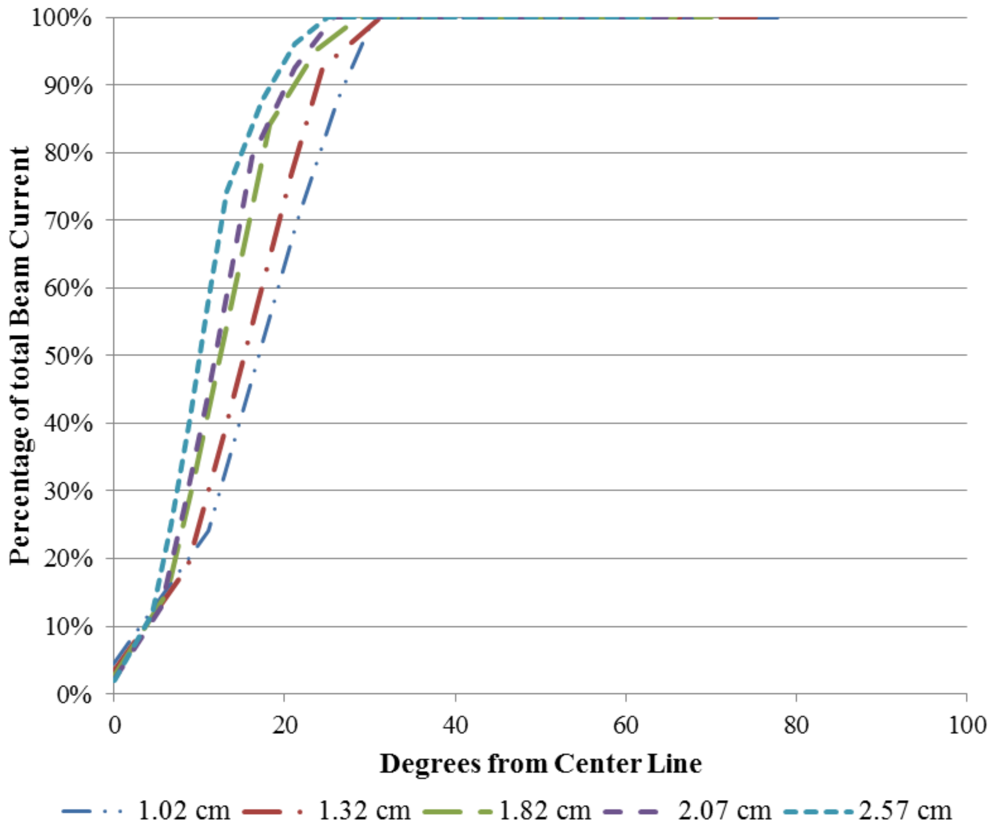

Figure 34: Percentage of Total Beam Current versus Beam Angle for a variety of positions downstream of the BIT-1

As the sweep's downstream distance increased, the beam divergence angle decreased. The beam divergence reported in Table 2 was found by interpolating the integrated current density sweeps.

Table 2: Beam Divergence Angle Calculation

Distance downstream cm	**Upper Limit Divergence Angle**	**Lower Limit Divergence Angle**	**Upper Limit Percentage of Total Current**	**Lower Limit Percentage of Total Current**	**Interpolated Beam Divergence Angle (95% of Current)**	**Thrust Correction Factor**
1.02	30.466°	26.114°	100%	87.63%	28°	0.877
1.32	31.218°	24.444°	100%	92.62%	26°	0.894
1.82	28.786°	23.787°	100%	95.09%	23°	0.915
2.07	25.784°	21.130°	100%	92.45%	22°	0.922
2.57	21.261°	17.290°	96.11%	87.65%	20°	0.932
				AVG	24°	0.926

Beam Target Measurements

The data presented in this section will encompass experiments performed at JPL, using a 30.48-cm molybdenum beam target. The beam target was used to test the XiPS cathode and thruster at various conditions and to measure the system's total beam current. First the current to the beam target was measured with only the cathode operating. The current on the XiPS© cathode keeper was increased from 1.4-A to 3-A. The beam target current based on the cathode conditions is shown in Figure 35.

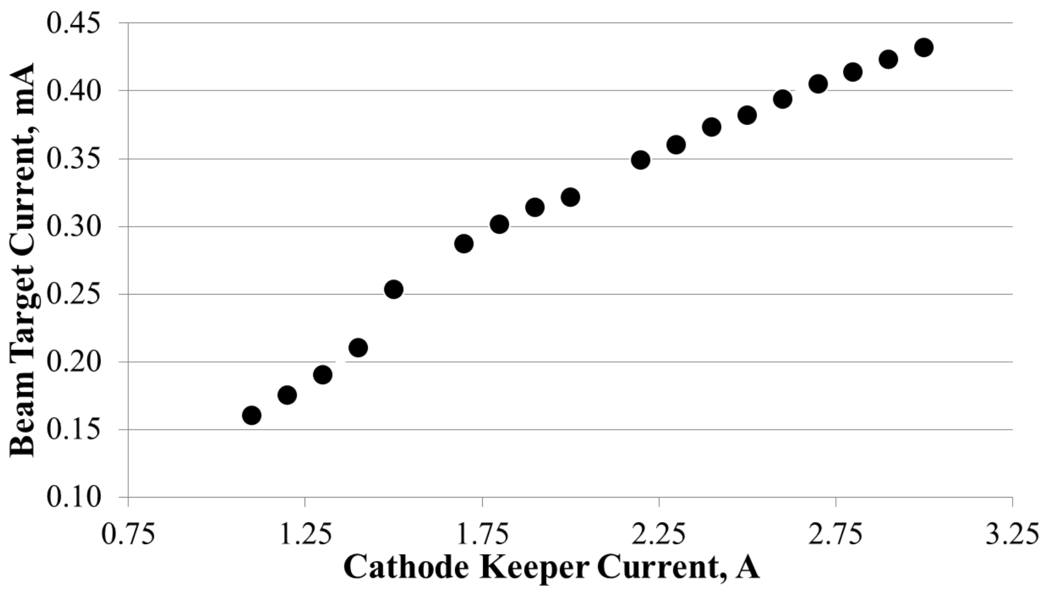

Figure 35: Beam Target Current with from XiPS Cathode Alone

Figure 35 shows the data obtained from the beam target with only the XiPS cathode operating for keeper currents ranging from 1.1 A to 3.0 A as well as the cathode keeper voltage condition during the test.

Table 3: Beam Target Current with Cathode Alone

Keeper Voltage	Keeper Current	Beam Target Current
V	A	mA
18.6	1.1	0.16
18.3	1.2	0.175
18.1	1.3	0.19
17.8	1.4	0.21
17.8	1.5	0.253
17.2	1.7	0.287
17.0	1.8	0.301
16.7	1.9	0.314
16.3	2.0	0.321
16.2	2.2	0.349
15.9	2.3	0.36
15.7	2.4	0.373
15.5	2.5	0.382
15.3	2.6	0.394
15.2	2.7	0.405
15.0	2.8	0.414
14.9	2.9	0.423
14.8	3.0	0.432

Varying Cathode Keeper Current

Next, with the thruster operating at a stable condition, the cathode keeper current was varied from 1.1-A to 2.8-A. For each cathode condition the total beam target current was reduced by the current value in Table 3. The remaining difference was assumed to be the current produced by the thruster.

Table 4 shows the average conditions of the thruster while the keeper current was varied. BIT-1 thrust was calculated from the corrected beam current, using Equation 26 and the beam divergence angle determined earlier, assuming all singly charged ions.

Table 4: Average Thruster Operating Conditions for Beam Target Experiments with Varying Cathode Keeper Current

Cathode Flow	Thruster Flow	Screen Volts	Accel Volts	Accel Current	RF Freq	Forward Power	Reverse Power	Pressure
sccm	sccm,	V	V	mA	MHz	W	W	Torr
6.7	0.193	1800	-200	0.062	8.51	8.24	0.638	3.34E-05

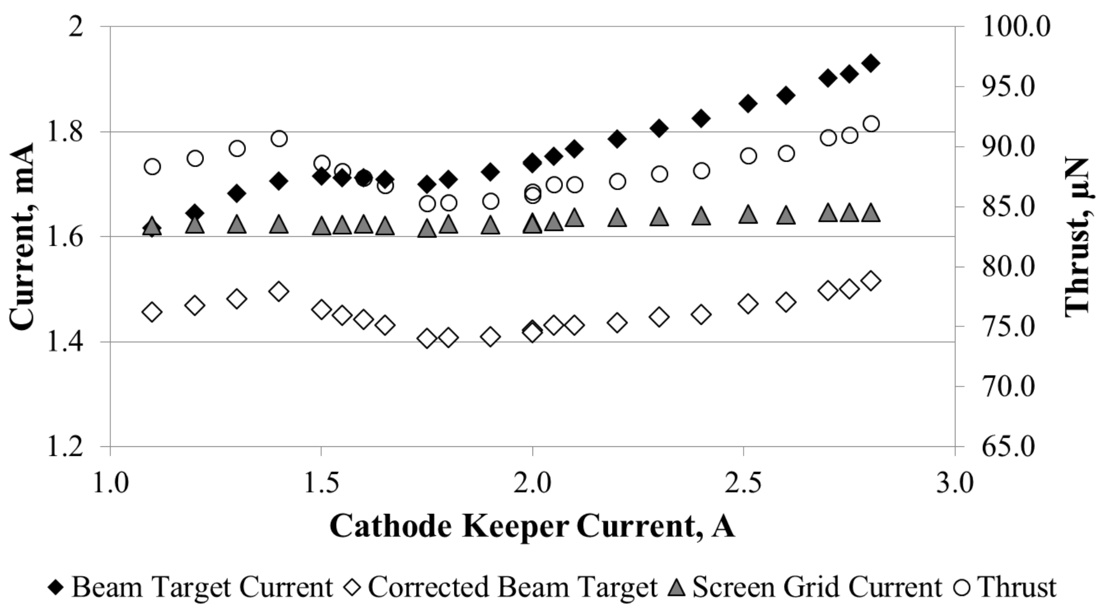

Figure 36: Collected Beam Target Current as a Function of Cathode Keeper Current

Figure 36 shows the data collected by the beam target while varying the cathode keeper current. The current measurements for the screen grid of the thruster, the beam target current and corrected beam target current are all shown along with the calculated thrust level using the corrected beam target current as the total beam current.

Varying Forward Power

Next, the forward RF power into the thruster was varied from 8.23-W down to 6.379-W, where the thruster was no longer able to sustain the discharge and turned off. Table 6 shows the operating conditions of the BIT-1 during these experiments. Figure 36 shows the current collected by the beam target, the corrected current accounting for the cathode keeper current collected by the beam target, the current collected by the screen grid, and the thrust as a function of thruster forward RF power. Figure 37 shows the data collected for this test.

Table 5: Conditions for Test Varying Forward Power

Cathode Flow	Thruster Flow	Screen Voltage	Accel Voltage	Accel Current	RF Freq.	Keeper Voltage	Keeper Current	Pressure
sccm	sccm	V	V	mA	MHz	V	A	Torr
6.7	0.3	1800	-200	0.06	8.51	18.8	1.1	3.34E-5

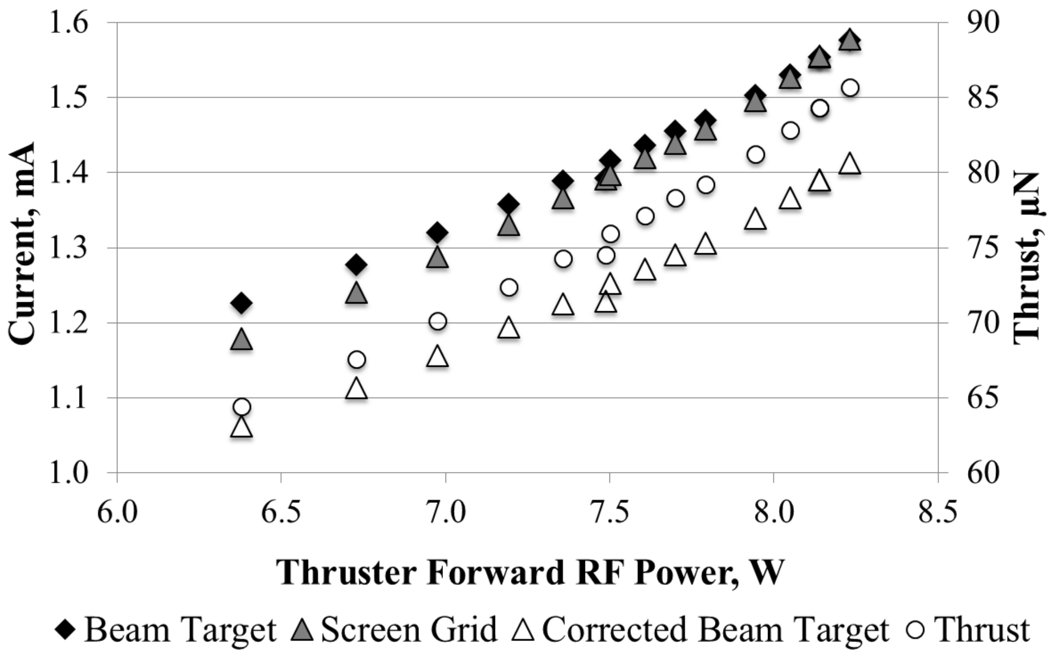

Figure 37: Change in Thrust by Varying Thruster Forward Power

Varying Screen Grid Voltage

Finally, the screen grid voltage was varied from 1200-V to 1600-V, while all other conditions were controlled and held constant. Table 6 shows the conditions of the thruster and cathode during this test. Figure 38 shows the measure current to the screen grid and beam target.

Table 6: Conditions for Test Varying Screen Current

Cathode Flow	Keeper Voltage	Keeper Current	Accel Voltage	Accel Current	RF Freq	Thruster Flow	Forward Power	Reverse Power	Pressure
sccm	V	A	V	mA	MHz	sccm	W	W	Torr,
6.7	11.7	3.0	-200	0.053	8.51	0.3	8.24	0.638	3.34E-5

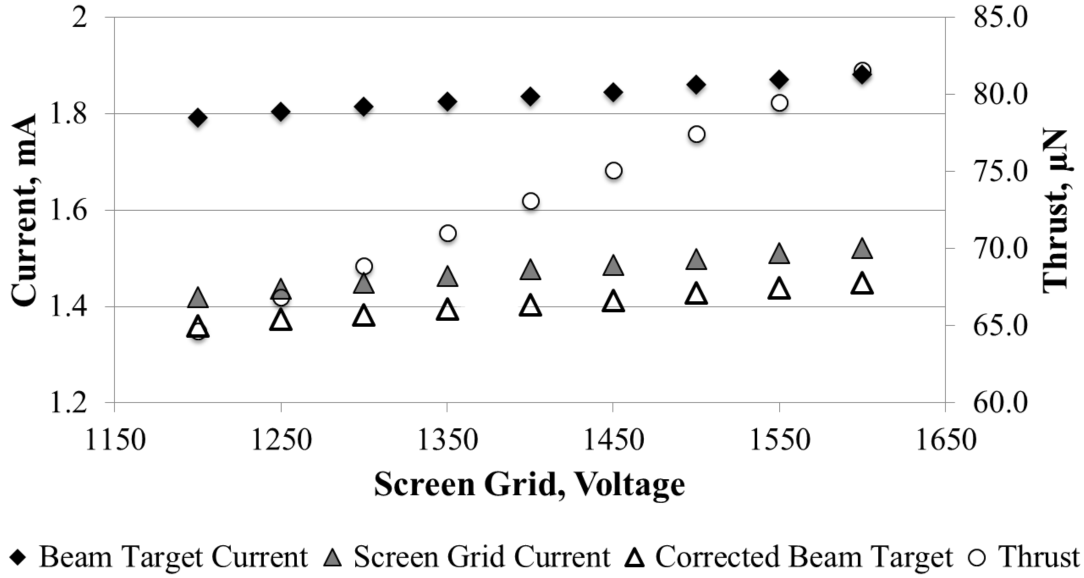

Figure 38: Thruster Performance Based on Varying Screen Grid Current

Langmuir Probe Measurements

The Langmuir probe data presented in this section were collected at ALPE. The Langmuir probe sweeps varied from -50-V to between 60-V and 150-V. The higher limit of the voltage sweep was decreased when the probe position was in the higher density regions of the thruster plume.

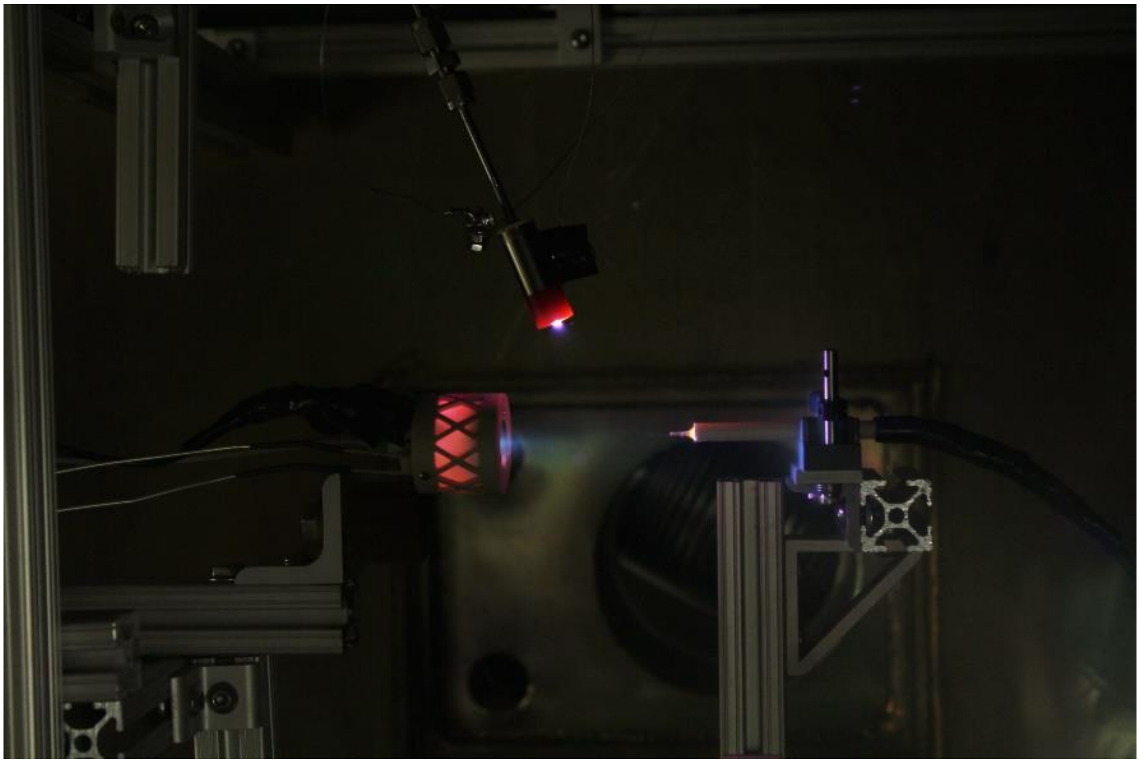

Figure 39: BIT-1 Operating at ALPE with the Langmuir Probe Downstream

Using the experimental setup shown in Figure 39, the thruster plume was evaluated at three different vectored angles; 0°, 2.5° and 5°. Where in 0° condition the thruster was pointed axially down the center of the vacuum chamber. The data for each condition were collected on separate days, and the thruster and cathode were shut down between tests. On each of the testing days, the thruster and cathode were operated at as close to the same conditions as possible.

Table 7 shows all of the conditions for each of these tests.

Table 7: Table of Thruster Operating Conditions

		0° Test		2.5° Test		5° Test	
		Start	End	Start	End	Start	End
Keeper Voltage	V	36.85	35.77	39.49	39.95	39.37	41.81
Keeper Current	A	0.3	0.3	0.3	0.3	0.3	0.3
Cathode Flow Rate	SCCM	0.5	0.5	0.5	0.5	0.5	0.5
Forward Power	W	12.2	12.3	12.2	11.9	10.9	11.09
Reflected Power	W	1.75	1.67	1.5	1.5	1.25	1.25
Screen Grid Voltage	V	1800	1800	1800	1800	1800	1800
Screen Grid Current	mA	2.2	2.12	2.25	2	2.2	2.1
Accel Grid Voltage	V	-200	-200	-200	-200	-200	-200
Accel Grid Current	mA	0.4	0.25	0.15	0.15	0.2	0.175
Thruster Flow	SCCM	0.2	0.2	0.2	0.2	0.2	0.2
Pressure	Torr	6.50E-05	5.59E-05	6.10E-05	5.20E-05	5.77E-05	5.33E-05

The Langmuir probe point measurements were then graphed in contour plots, using Tecplot. In the contour plots presented, the thruster was positioned relative to the graph as shown in Figure 40, with the plume of the thruster extending down the X Position axis and the exact orientation being modified as the thrust was vectored. All position values are presented in millimeters.

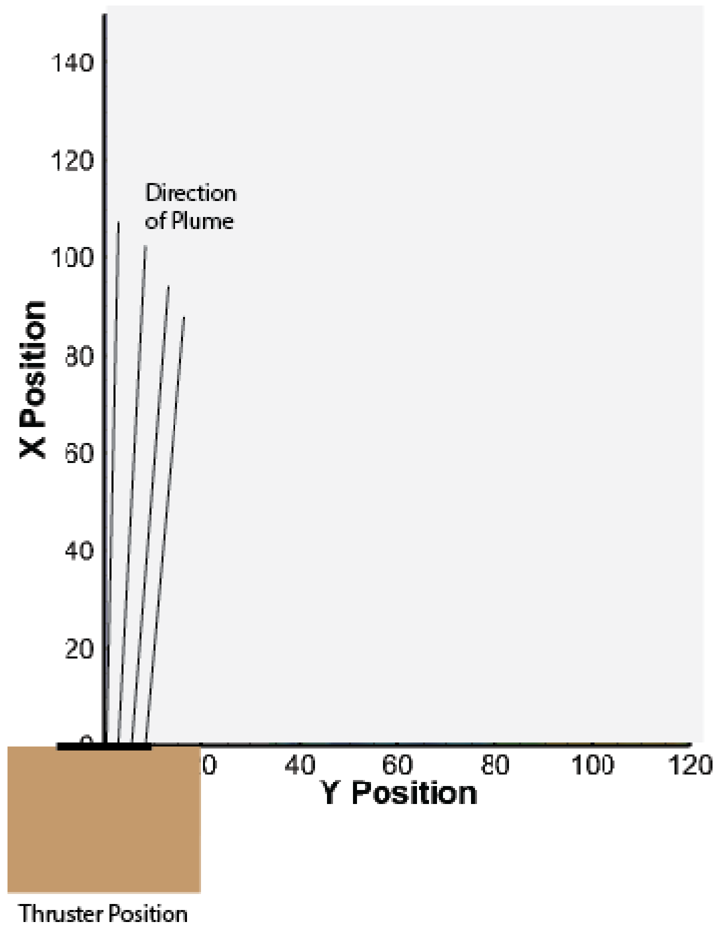

Figure 40: Position of Thruster on Langmuir Probe Plots

The point of rotation for the thrust vectoring was not directly below the front face of the thruster. When the thrust angle was increased, the center of the thruster face moved down the Y Position axis. During the experiment, the thruster rotated about 15° around its attachment point, as shown in Figure 41. The center of the thruster moved 7.37-mm down the Y Position axis. For the 0°, 2.5° and 5° conditions the center of the thruster was consequently positioned at 7.37-mm, 11.63-mm and 15.9-mm on the Y position axis, respectively. On the following data plots a dashed line will indicate the direction at which the thruster was pointing during each test.

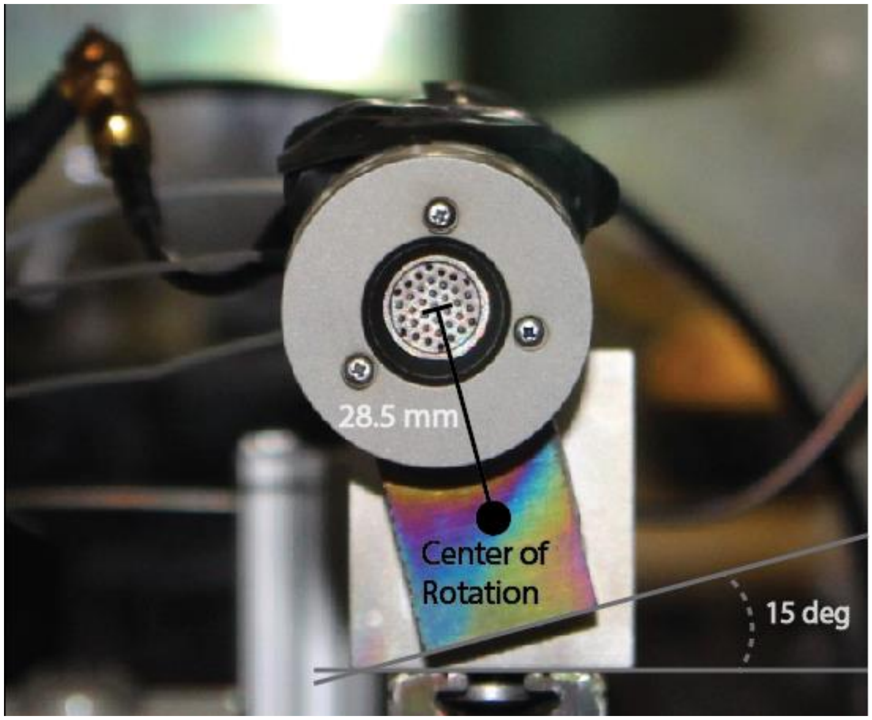

Figure 41: Rotation Experience by Thruster during Langmuir Probe Testing at ALPE

Floating Potential

The floating potential of the plume for the 0°, 2.5° and 5° thrust vector angles is displayed in Figure 43 and Figure 44 respectively. An increase in floating potential is seen as the probe is moved away from the thruster's centerline, indicated by the dashed line. An observed increase in floating potential is an indicator of a lower concentration of electrons. As the thrust vector angle is increased, the floating potential along the Y-position axis rises. The high floating potential is an indicator for high ion concentration. High ion concentration away from the central beam could be the result of charge exchange collisions. It is also possible that this pattern seen in the data is the result of facility effects. Further testing is required to confirm whether or not these measurements indicate the presence of low energy ions resulting from charge exchange collisions.

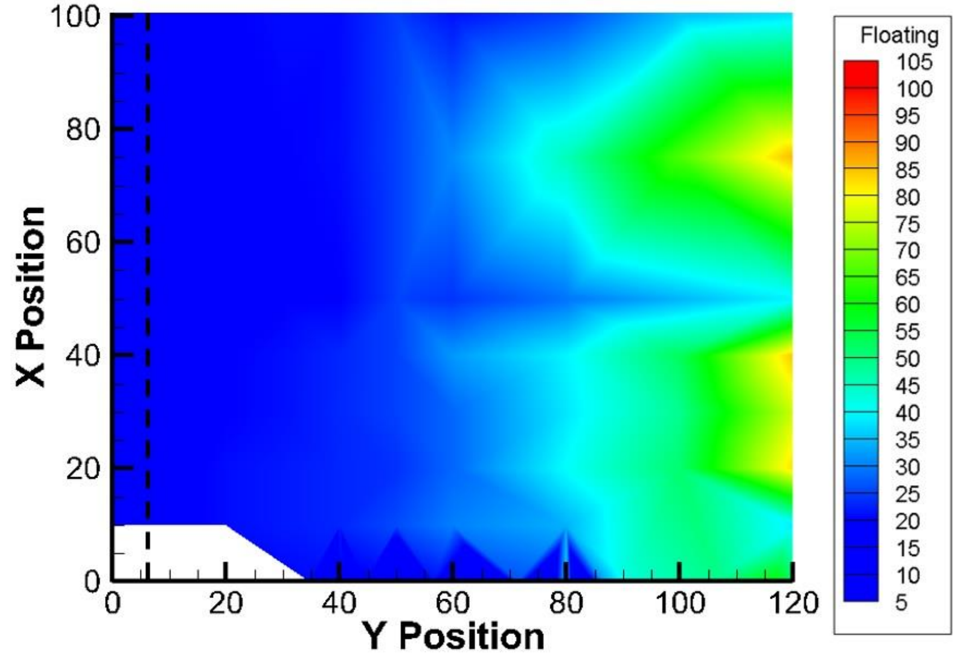

Figure 42: Floating Potential in Volts for 0° Thrust Vector, All Axis Values in mm

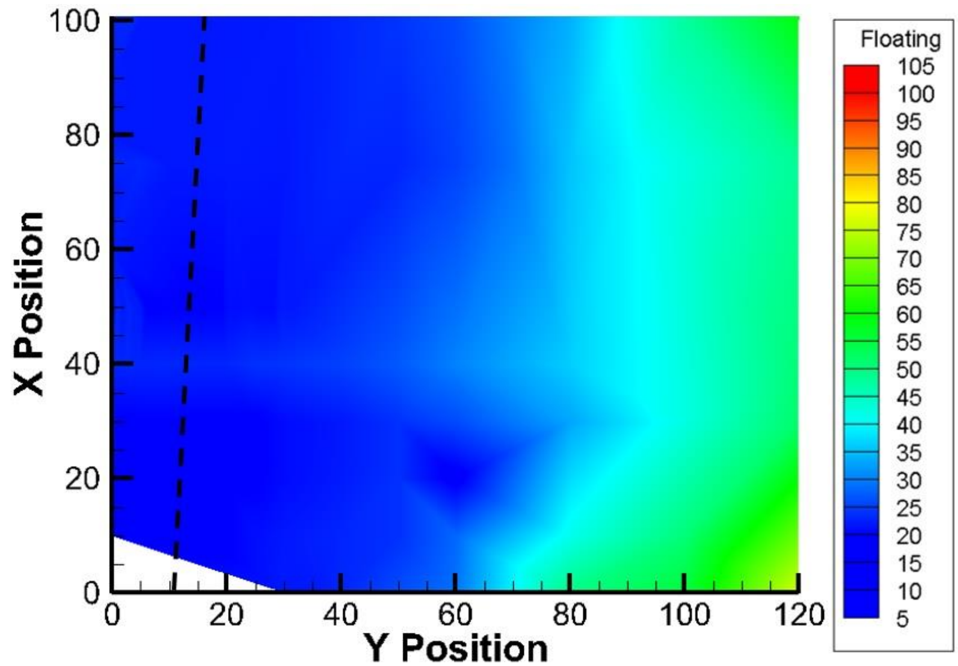

Figure 43: Floating Potential in Volts for 2.5° Thrust Vector, All Axis Values in mm

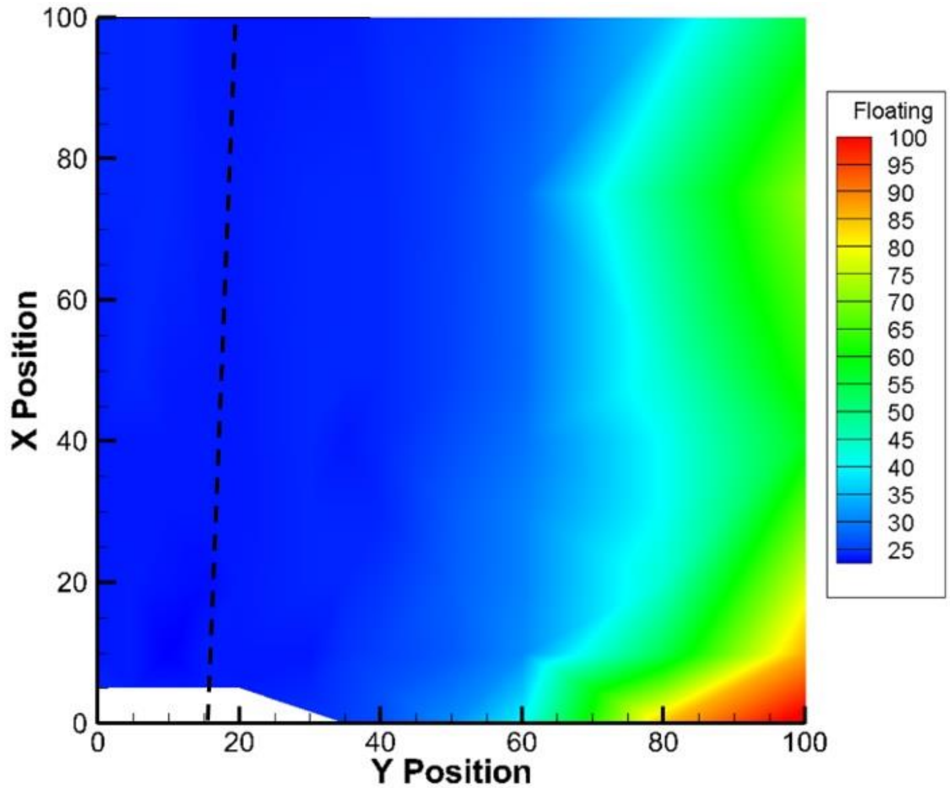

Figure 44: Floating Potential in Volts for 5° Thrust Vector, All Axis Values in mm

Plasma Potential

The trends present in the floating potential plots are seen in the plasma potential data shown in Figure 45, Figure 46, and Figure 47. In the 2.5° and 5° thrust vector plots the beam can clearly be seen turning. The high potential on the 5° thrust vector plot is interesting to note because again this higher concentration of ions could potentially lead to issues with spacecraft charging and interference with electronics.

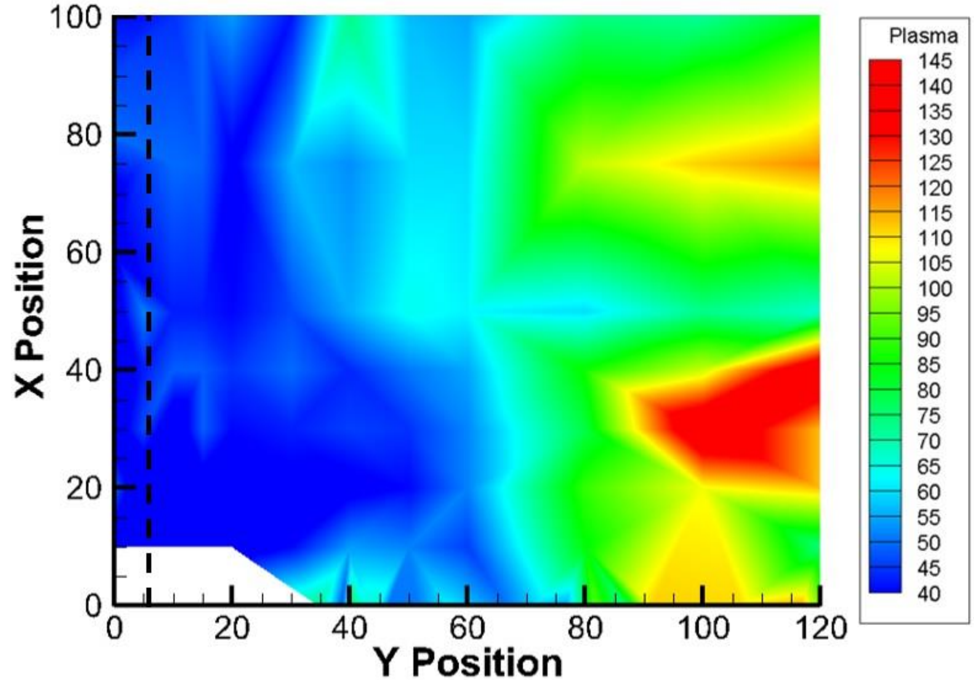

Figure 45: Plasma Potential in Volts for 0° Thrust Vector, All Axis Values in mm

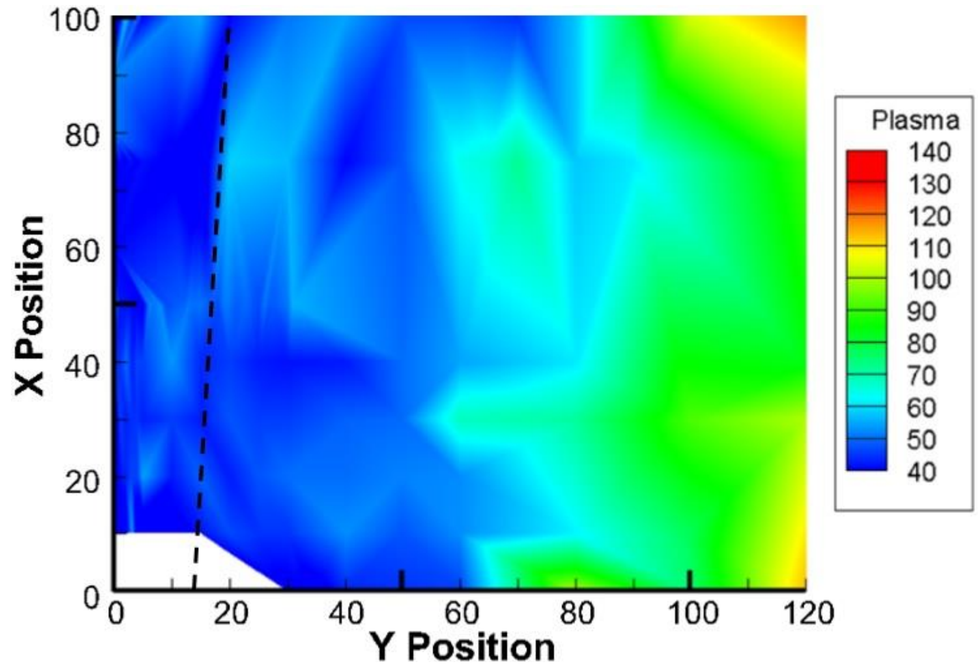

Figure 46: Plasma Potential in Volts for 2.5° Thrust Vector, Singular Point Removed, All Axis Values in mm

In the plasma potential plot in Figure 46, a singular point was removed. It is clear that it was generated because of an error, but the origin of this error is unknown. The data graphed without the point removed is shown in the Appendix.

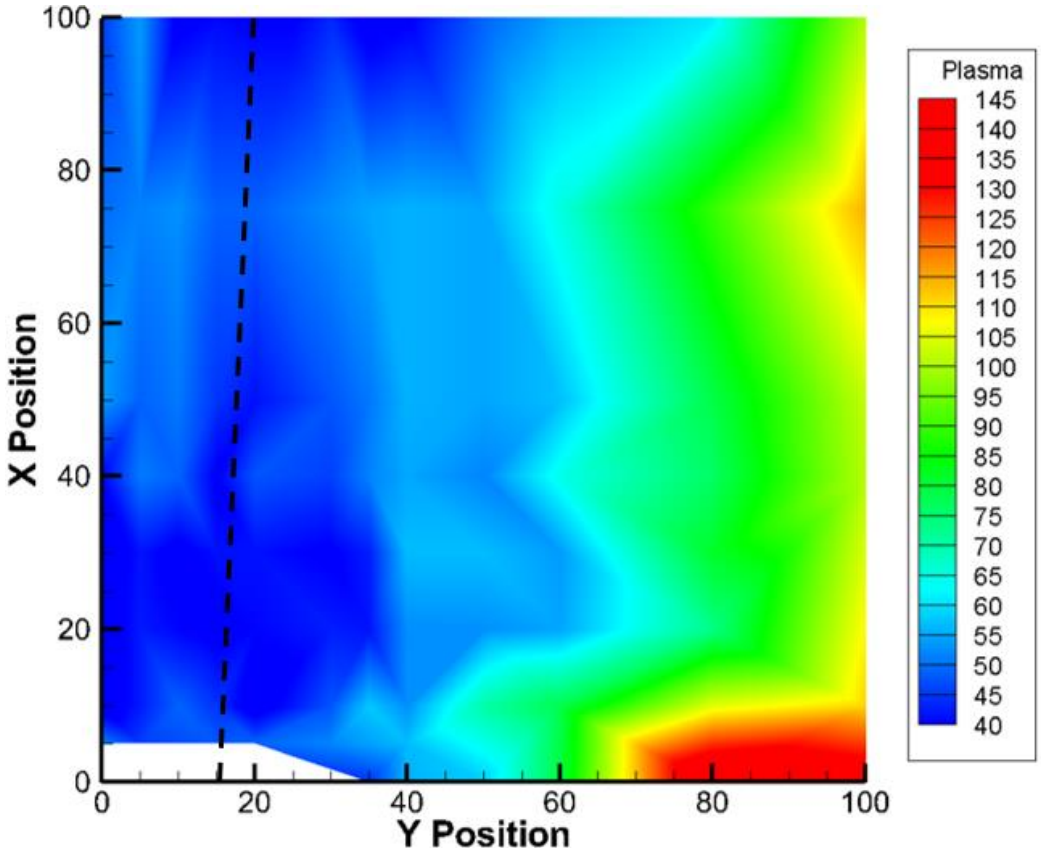

Figure 47: Plasma Potential in Volts for 2.5° Thrust Vector, All Axis Values in mm

OML Density

The inverse of the Knudsen number is used to determine whether or not the OML or thin sheath method should be used to calculate ion number density. The ratio between probe radius and Debye length determined that the OML calculation method was valid. Plots of the probe radius to Debye length ratio are shown in the Appendix for all three thrust vector conditions. For the 0° condition, the OML density again confirms a highly collimated beam, but there is evidence of ions in lower density surrounding the thruster exit, particularly from 20 to 40-mm on the Y position axis, at an x-location of 20-mm-downstream.

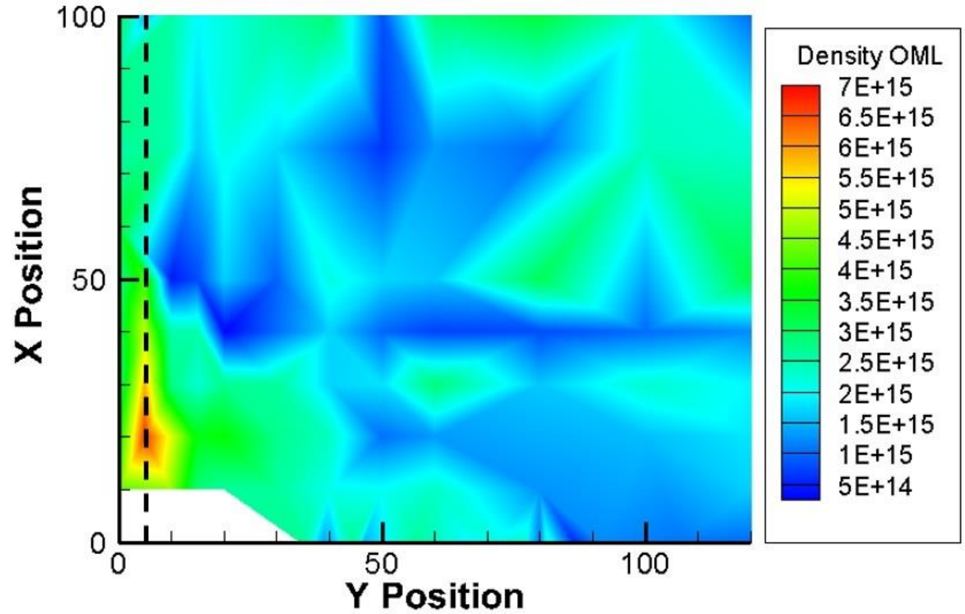

Figure 48: Ion number density (m^{-3}) for 0° Thrust Vector. All Distances Are in mm.

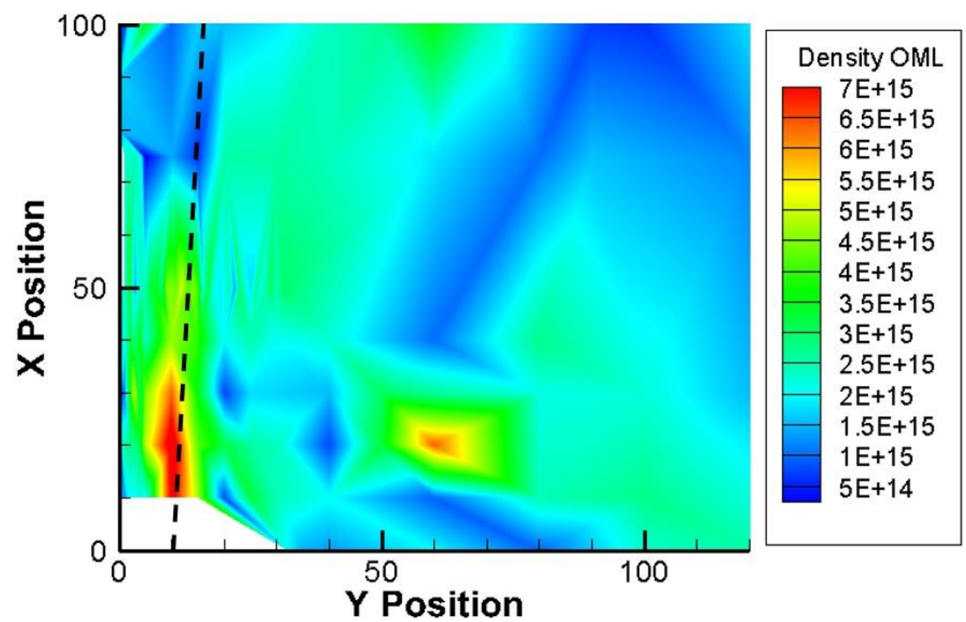

Figure 49: Ion number density (m^{-3}) for 2.5° Thrust Vector. All Distances Are in mm.

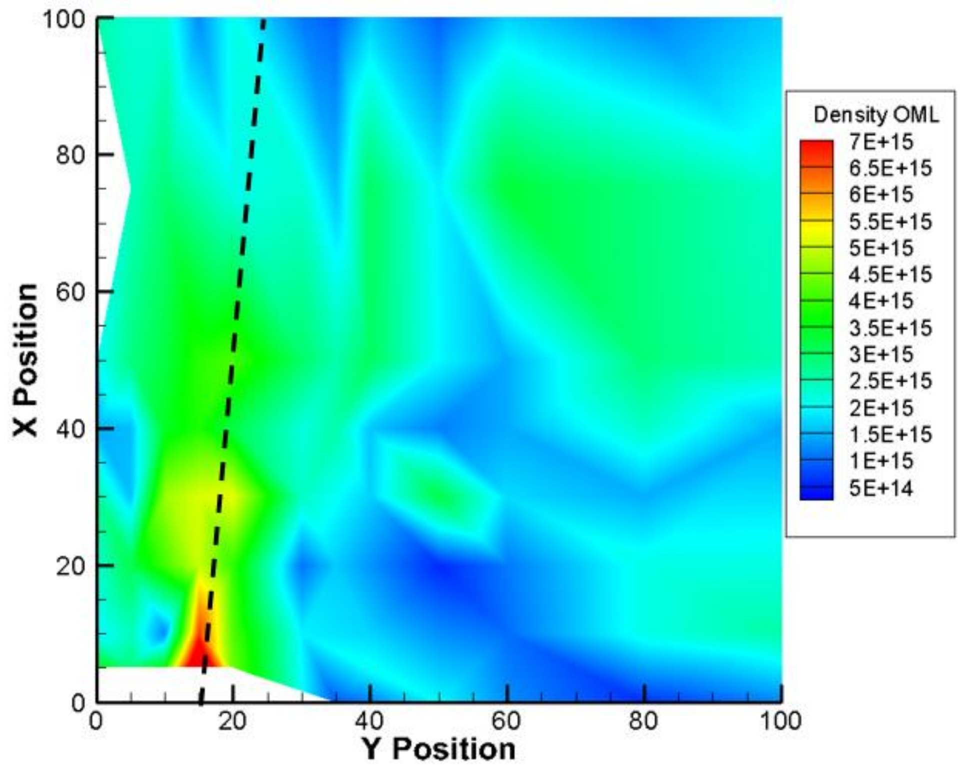

Figure 50: Ion number density (m^{-3}) for 5° Thrust Vector. All Distances Are in mm.

Micro RF Ion Thruster and Passive
Magnetic Stabilization

The magnetic field of the RF thruster coil was simulated by modeling an 8 MHz RF signal into the coil at 10 W of forward power. The resulting magnetic field interaction was calculated and used to determine a minimum CubeSat size that allowed for unaffected thruster operation and magnetic stabilization.

It is important to note that the model is an approximation of the BRFIT-1, and that the BRFIT-1 is an early version of the BIT-1 thruster. One of the main design differences between the two thrusters is that the BIT-1's RF coil and discharge chamber is enclosed within a Faraday cage. This analysis is only valid as an approximate simulation of the earlier BRFIT-1. The plots and simulations presented serve to show the importance of studying the interactions between these types of systems.

Independent Thruster Operation

First, the RF thruster was modeled without the permanent magnets present. The values of the flux density were normalized, compared to the maximum flux density calculated when the permanent magnets were present. In this way, all graphs are normalized to the same reference value. Figure 51 shows the directionality and normalized magnitude of the thruster's magnetic field.

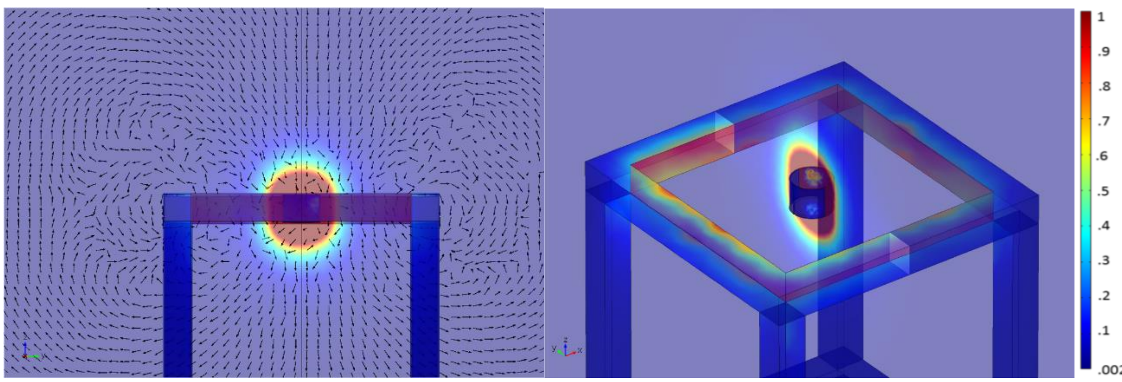

Figure 51: Normalized Magnetic Flux Density in of Isolated Thruster Operation

Figure 52 is a graph of the magnetic flux density down the center line of the structure and thruster coil. The zero position is defined as the base of the coil.

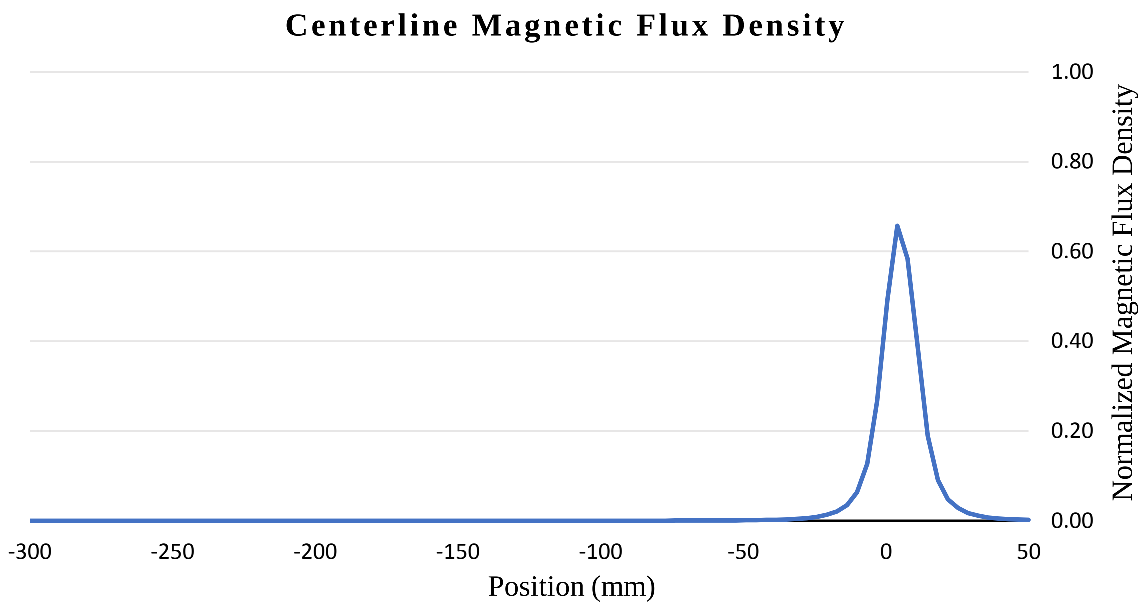

Figure 52: Normalized Thruster Magnetic Flux Density in the Radial Direction

1U CubeSat Configuration

The next simulation performed, shown in Figure 53 and Figure 54, measured the magnetic flux density of the system in a 1U CubeSat configuration, where the permanent magnets were placed in the corners of the first 100 mm × 100 mm × 100 mm cube.

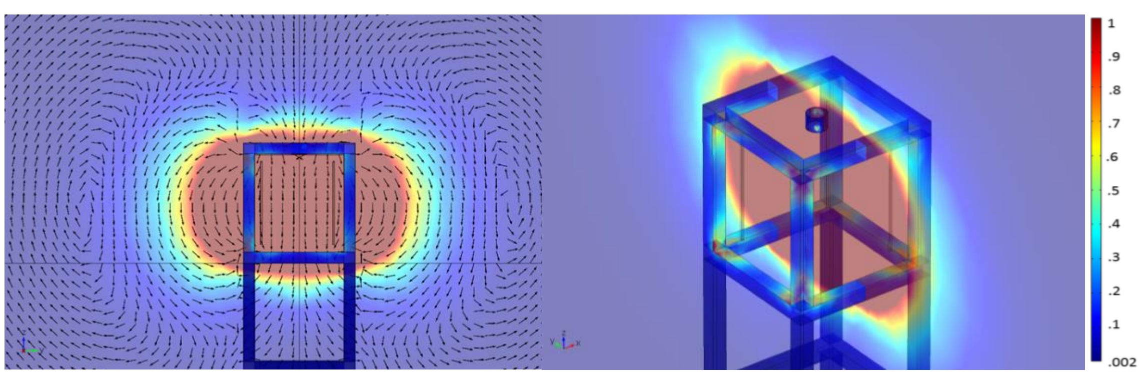

Figure 53: Normalized Magnetic Flux Density, 1U CubeSat Configuration

From these calculations, it can be observed that there was significant interaction between the permanent magnets and the magnetic field lines of the RF thruster.

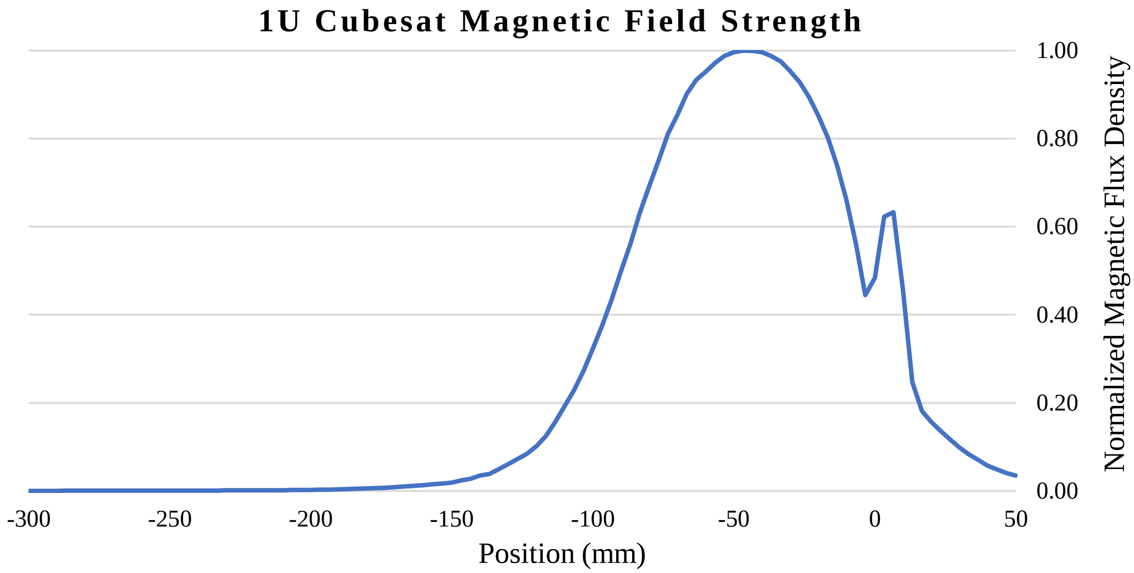

Figure 54: Normalized Magnetic Flux Density 1U Configuration in the Radial Direction

2U CubeSat Configuration

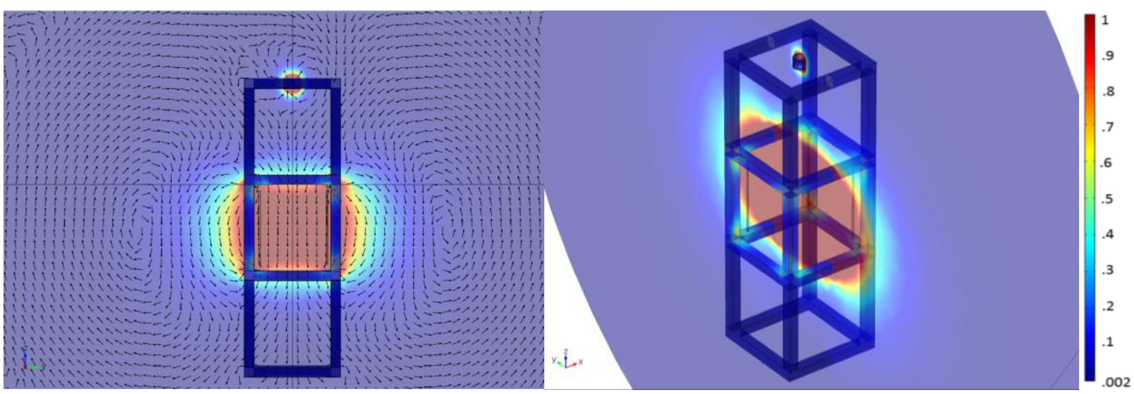

Figure 55: Normalized Magnetic Flux Density, 2U CubeSat Configuration

A 2U (100 mm × 100 mm × 200 mm) CubeSat configuration was then studied. Interactions between the two magnetic systems was greatly reduced from the 1U configuration but was still observed. Figure 55 and Figure 56 show the results of this simulation.

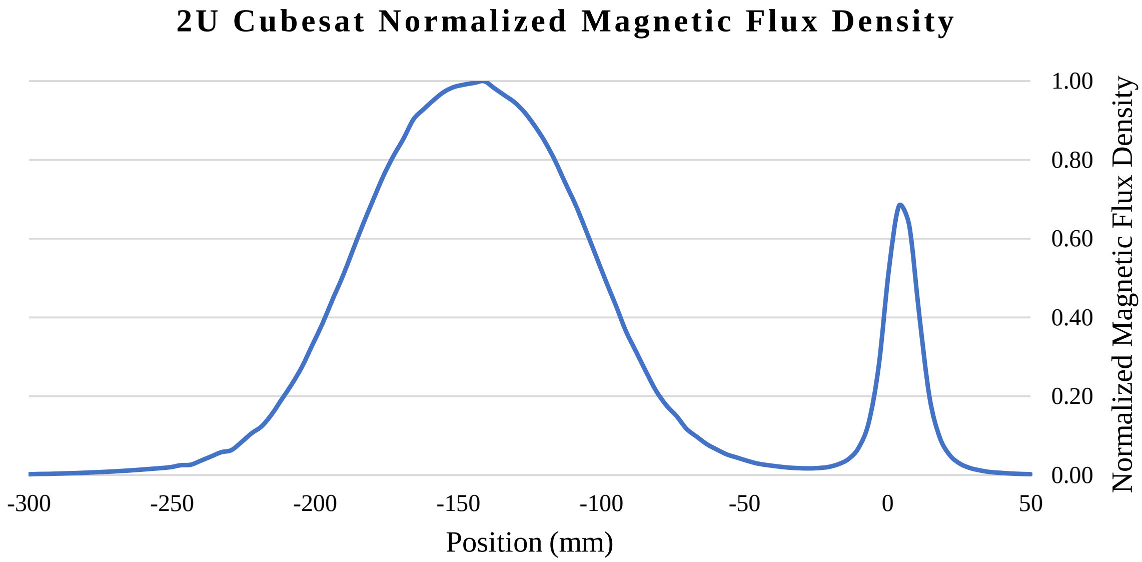

Figure 56: Normalized Magnetic Flux Density 2U Configuration in the Radial Direction

3U CubeSat Configuration

A 3U (100 mm × 100 mm × 300 mm) CubeSat was the final configuration studied, and the results are shown in Figure 57 and Figure 58. From the simulation performed it is clear that in this configuration the permanent magnets have no effect on the thruster coil magnetic field. In the space between the permanent magnets and the thruster, the magnetic flux density drops to a negligible value, indicating that the two systems are operating independently.

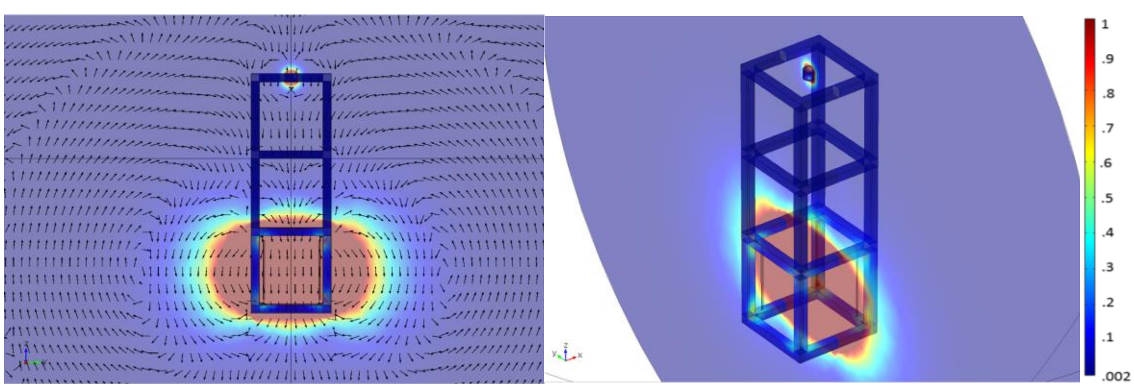

Figure 57: Normalized Magnetic Flux Density, 3U CubeSat Configuration

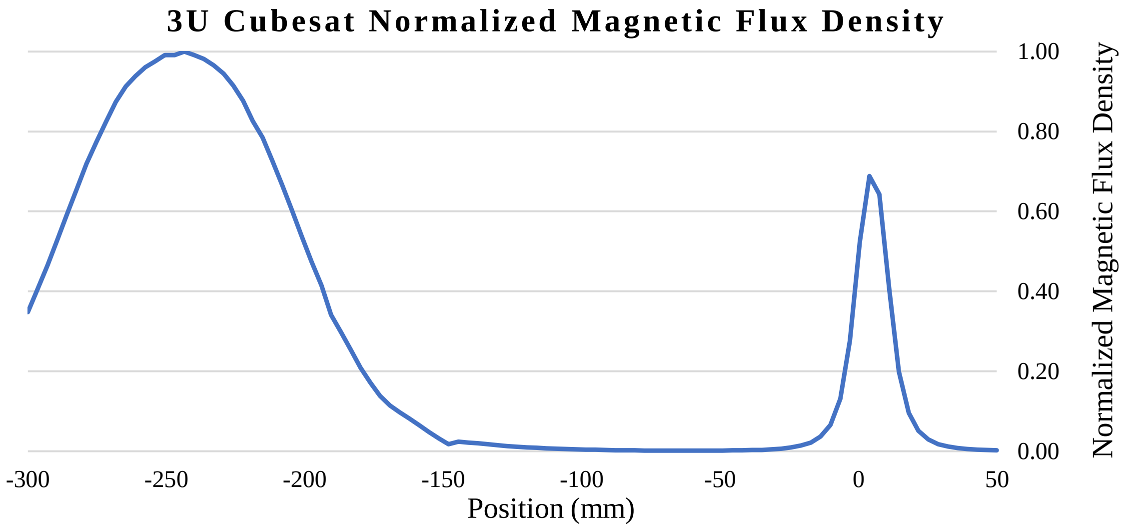

Figure 58: Normalized Magnetic Flux Density 3U Configuration in the Radial Direction

CHAPTER V

CONCLUSION

Discussion

The BIT-1 thruster was tested under laboratory conditions and operated at 8.16 W of forward power. A Faraday probe was used to measure the thruster beam current density. Through interpolation, divergence angles of the beam were found at five downstream distances. These five values were averaged to obtain a 24° beam divergence angle for the thruster.

A beam target was then used to collect the total beam current of the thruster. The 30.48-cm beam target was placed 25.4-cm downstream of the thruster. With a beam divergence angle of 24°, the total beam current was collected by the beam target. By varying the RF power into the thruster, it was demonstrated that it is possible to precisely vary the thrust output. Varying the forward power from 6.975-W to 8.23-W produced an increase in thrust from 70.1-μN to 86.7-μN. The thruster was also tested over a range of other operating conditions. The neutralizing cathode keeper current was varied from 2.8-A to 1.1-A, and the screen grid current was swept from 1200-V to 1600-V.

The plume of the BIT-1 was analyzed, using a Langmuir probe at three different thrust vector conditions, 0°, 2.5°, and 5°. The floating potential, plasma potential, and ion number density were measured as a function of downstream position within the plume. Both the plasma and floating potentials were found to increase as the probe was moved radially away from the centerline of the thruster. The increasing potentials may indicate a higher ion concentration relative to the number of electrons near the radial wings of the thruster but could also be the result of facility effects. Further investigation is to determine the cause. The 5° condition produced an interesting result, whereby an increase in both floating and plasma potential along the Y position axis perpendicular to the thruster face was observed.

Modeling, using the simulation and finite element analysis software COMSOL Multiphysics 4.4, was also performed. The model and simulation analyzed the interactions of an RF coil modeled after the BRFIT-1 without any magnetic shielding and a typical passive magnetic stabilization system. While the 3U configuration showed little interaction between the two magnetic fields, the 2U and 1U simulations showed interference in the flux density between the two systems. Further analysis and laboratory testing are required to determine the extent to which this interaction is reduced with the addition of a Faraday cage.

Future Work

This research does not definitively resolve the issues surrounding the integration of EP devices into CubeSat platforms. However, it will serve as a resource and foundation for these types of investigations in the future. There are many questions that still remain unanswered. Determining the extent to which charge exchange collisions can effect small space craft operation remains a key next step. The data presented in this research indicates that there are ions present within the plume of the BIT-1 that could be the result of CEX collisions. Further analysis of the thruster plume is necessary to determine if this is in fact the case. If CEX collisions are occurring, it would be beneficial to know where they are occurring. If a high number of these collisions are happening outside the thruster body, then space charging issues could potentially develop. A higher resolution of the distance between measurement positions to further the understanding of the physics at the edges of the plume, as well as measuring the energy levels of the ions leaving the thruster are all areas of significant interest. Integrating and testing this thruster on a CubeSat platform with solar panels and other CubeSat systems in a laboratory setting is necessary. The development of some standard or qualification test for these types of propulsion devices would be beneficial.

Recommendations

While working on this project, the real challenge of scaling down EP devices was made clear. In concert, testing these devices can be equally as challenging. The ALPE facility was limited by the pumping capacity of its vacuum facility. Before the acquisition of the 1/8-in BaO cathode from E Beam Inc., there were unsuccessful attempts to operate the thruster with larger cathodes that required higher flow rates. Higher flow rates produced higher operating pressures within the vacuum chamber facility. The higher pressures made it difficult to sustain pressures within the operating range of the thruster ($< 5\times10^{-5}$ Torr). In the future, it is recommended that a vacuum facility with a pumping speed of at least 1250 l/s be used for testing the BIT-1. Attempts to operate the thruster at higher pressures resulted in either short continuous operation or no ignition of the thruster. During the short lived operations, the thruster grids and discharge chamber would become coated with sputtered material. The thruster would then have to be disassembled and cleaned using a glass bead blaster.

Even while testing the thruster with the smaller BaO cathode, the area around the accel grid became dirty and coated with sputtered material during operation. It is still unknown if this sputtering is the result of normal thruster operation, if it comes from the cathode, or if it is a result of the vacuum facility. The use of a smaller cathode or facility with a higher pumping capacity may resolve this issue. To operate this thruster at a stable condition, the system dictated a flow rate three times higher than the flow rate reported from other experiments. The reason for this discrepancy is unclear, but again it is possible a lower operating pressure could provide the solution.

BIBLIOGRAPHY

[1] G. D. Chandler, D. T. Mcclure, S. F. Hishmeh, J. E. Lumpp, J. B. Carter, B. K. Malphrus, D. M. Erb, W. C. Hutchison, G. R. Strickler, B. Green, J. W. Cutler, and R. J. Twiggs, "Development of an Off-the-Shelf Bus for Small Satellites," 2007.

[2] J. Straub, "CubeSats : A Low-Cost , Very High-Return Space Technology," *AIAA Reinventing Sp. Conf. 2012*, 2012.

[3] J. Mueller, R. Hofer, M. Parker, and J. Ziemer, "Survey of Propulsion Options for Cubesats," *57th JANNAF Propuls. Meet.*, pp. 1–56, 2010.

[4] C. K. Castonguay, S. Haque, G. Teel, J. Lukas, M. Keidar, C. Dinelli, I. B. Maloney, E. A. S. Hanlon, and J. S. Kang, "Quad - channel Micro - cathode Arc Thruster Electric Propulsion Subsystem for the Ballistically Reinforced Communications Satellite (BRICSat - P)," in *Propulsion and Energy Forum*, 2014, pp. 1–11.

[5] S. Lee, A. Hutputanasin, A. Toorian, W. Lan, and R. Munakata, "CubeSat Design Specification," San Luis Obispo, 2009.

[6] D. M. Goebel and I. Katz, *Fundamentals of Electric Propulsion: Ion and Hall Thrusters*. New Jersey: John Wiley & Sons, INC, 2008.

[7] S. Hurley, G. Teel, J. Lukas, S. Haque, M. Keidar, C. Dinelli, and J. Kang, "Thruster Subsystem for the United States Naval Academy ' s (USNA) Ballistically Reinforced Communication Satellite (BRICSat - P)," pp. 1–10, 2015.

[8] P. J. Wilbur and V. K. Rawlin, "Ion Thruster Development Trends and Status in the United States Introduction," *J. Propuls. Power*, vol. 14, no. 5, 1998.

[9] J. Mueller, R. Hofer, and J. Ziemer, "Survey Of Propulsion Technologies Applicable To Cubesats," pp. 1–58.

[10] J. Puig-Suari, C. Turner, and W. Ahlgren, "Development of the Standard CubeSat Deployer and a CubeSat PicoSatellite," *IEEE Aerosp. Conf. Proc.*, vol. 1, 2001.

[11] H. Heidt, P. J. Puig-suari, P. A. S. Moore, P. S. Nakasuka, and P. R. J. Twiggs, "CubeSat: A new Generation of Picosatellite for Education and Industry Low-Cost Space Experimentation," in *USU Conference on Small Satellites*.

[12] S. Higginbotham, "CubeSat Launch Initiative." Human Exploration and Operations Mission Directorate, 2016.

[13] S. Rawashdeh, "Passive Attitude Stabilization for Small Satellites," pp. 1–72, 2009.

[14] A. C. Stickler, "Elementary Magnetic Attitude Control System," vol. 13, no. 5, pp. 282–287, 1975.

[15] I. Garrick-bethell, R. P. Lin, H. Sanchez, B. A. Jaroux, M. Bester, P. Brown, D. Cosgrove, M. K. Dougherty, J. S. Halekas, D. Hemingway, P. C. Lozano, F. Martel, and C. W. Whitlock, "Lunar magnetic field measurements with a cubesat,"

in *Proc. SPIE 8739, Sensors and Systems for Space Applications VI*, 2013, vol. 8739, pp. 1–26.
[16] G. Moore, W. Hoelmans, A. Huang, J. Lee, M. Mcmullen, J. White, R. Twiggs, B. Malphrus, N. Fite, D. Wilt, J. Lyke, S. Davis, W. Bradley, 2Lt. Thomas Chiasson, and P. Patterson, "3D Printing and MEMS Propulsion for the RAMPART 2U CUBESAT Conference on Small Satellites," in *24th Annual AIAA/USU Conference on Small Satellites*, 2010.
[17] W. H. Steyn and V. Lappas, "Cubesat solar sail 3-axis stabilization using panel translation and magnetic torquing," *Aerosp. Sci. Technol.*, vol. 15, no. 6, pp. 476–485, 2011.
[18] D. Gibbon and C. Underwood, "Low cost butane propulsion systems for small spacecraft," in *15th AIAA / USU Conference on Small Satellites*, 2001.
[19] F. Guarducci, M. Coletti, and S. B. Gabriel, "Design and Testing of a Micro Pulsed Plasma Thruster for Cubesat Applicaiton," in *The 32nd International Electric Propulsion Conference*, 2011, pp. 1–10.
[20] F. Rysanek, J. W. Hartmann, R. Binder, and J. Schein, "MicroVacuum Arc Thruster Design for a CubeSat Class Satellite," in *16th Annual/USU Conference on Small Satellites*, 2002, no. 217, pp. 1–7.
[21] D. T. Schmuland, C. Carpenter, and R. K. Masse, "Mission Applications of theMRS-142 CubeSat High-Impulse Adaptable Monopropellant Propulsion System (CHAMPS)," in *48th AIAA/ASME/SAE/ASEE Joint Propulsion Conference & Exhibit*, 2012, no. August, pp. 1–9.
[22] R. Wirz, M. Gale, J. Mueller, and C. Marrese, "Miniature Ion Thrusters for Precision Formation Flying," in *40th AIAA/ASME/SAE/ASEE Joint Propulsion Conference and Exhibit*, 2004.
[23] M. Tsay, K. Hohman, and L. Olson, "Micro RF Ion Engine for Small Satellite Applications," in *23rd Annual AIAA/USU Conference on Small Satellites*, pp. 1–6.
[24] C. M. Marrese-Reading, J. Mueller, and W. C. West, "Microfluidic Electrospray Thruster," US8850792 B2, 2014.
[25] D. Spence, E. Ehrbar, N. Rosenblad, N. Demmons, T. Roy, S. Hoffman, D. Williams, V. Hruby, and C. Tocci, "Electrospray Propulsion Systems for Small Satellites," in *27th Annual AIAA/USU Conference on Small Satellites*, 2013, pp. 1–7.
[26] L. Perna, P. Lozano, and F. Martel, "Miniature Ion Electrospray Thrusters And Performance Tests On Cubesats," in *26th Annual AIAA/USU Conference on Small Satellites*, 2012, pp. 1–6.
[27] E. A. Bering, F. Chang-Diaz, and J. Squire, "The Use of RF Waves in Space Propulsion Systems," *Radio Sci. Bull.*, vol. 310, no. 310, pp. 92–106, 2004.
[28] M. Tsay, K. Hohman, N. Rosenblad, E. Ehrbar, and M. Robin, "Micro Radio-Frequency Ion Propulsion System," no. August, pp. 1–11, 2012.
[29] R. Gomer, *Field Emission and Field Ionization*. Cambridge, Massachusetts: Harvard University Press, 1961.
[30] M. M. Tsay, "Two-Dimensional Numerical Modeling of Radio-Frequency Ion," Massachusetts Institute of Technology., 2010.
[31] M. M. Tsay, "Numerical Modeling of a Radio-Frequency Micro Ion Thruster," Massachusetts Institue of Technology, 2006.

[32] M. Tsay and M. Martinez-Sanchez, "Simple Performance Modeling of a Radio-Frequency Ion Thruster," *Proc. to 30th …*, pp. 1–10, 2007.
[33] J. T. Gudmundsson and M. A. Lieberman, "Magnetic induction and plasma impedance in a cylindrical inductive discharge," *Inst. Phys. Electron. Journals*, vol. 540, 1997.
[34] G. Aston and P. J. Wilbur, "Ion Extraction from a Plasma," *J. Appl. Phys.*, vol. 52, no. 4, pp. 2614–2626, 1981.
[35] P. J. Wilbur, J. R. Beattie, and J. Hyman Jr., "An approach to the parametric design of ion thrusters," in *Spacecraft Propulsion and Power*, 1988, pp. 467–475.
[36] J. S. Snyder and J. R. Brod, "Performance Characterization and Vibration Testing of 30-cm Carbon-Carbon Ion Optics," *40" AIAA/ASME/SAE/ASEE Jt. Propuls. Conf. Exhib.*, 2004.
[37] K. Nishiyama, S. Hosoda, Y. Shimizu, H. Kuninaka, and R. Tsukizaki, "Feasibility Study on Performance Enhancement Options for the ECR Ion Thruster μ10," *44th AIAA/ASME/SAE/ASEE Jt. Propuls. Conf. Exhib.*, no. July, pp. 1–12, 2008.
[38] M. Tajmar, "Electric Propulsion Plasma Simulations and Influence on Spacecraft Charging Introduction," *J. Spacecr. Rockets*, vol. 39, no. 6, 2002.
[39] R. C. Olsen, "Modification of Spacecraft Potentials by Plasma Emission," *J. Spacecr.*, vol. 18, no. 5, pp. 462–469, 1980.
[40] C. Charles, "Plasmas for spacecraft propulsion," *J. Phys. D. Appl. Phys.*, vol. 42, no. 16, p. 163001, 2009.
[41] F. F. Chen, *Introduction to Plasma Physics and Controlled Fusion Volume 1: Plasma Physics*. Plenum Press, 1984.
[42] P. Monk, *Finite Element Methods for Maxwell's Equations*. Oxford: Clarendon Press, 2003.
[43] I. H. Hutchinson, *Principles of Plasma Diagnostics*, Second. New York: Cambridge University Press, 2002.
[44] K. M. Lemmer, "Use of a Helicon Source for Development of a Re-Entry Blackout Amelioration System by," The University of Michigan, 2009.
[45] J. G. Laframboise and L. W. Parker, "Probe Design for Orbit-Limited Current Collection," *Phys. Fluids*, vol. 16, no. 5, 1973.
[46] J. G. Laframboise and J. Rubinstein, "Theory of a cylindrical probe in a collisionless magnetoplasma," vol. 1900, no. 1976, 2016.
[47] R. W. Conversano, "Low-Power Magnetically Shielded Hall Thrusters," University of California Los Angeles, 2015.
[48] D. L. Brown, "Investigation Of Low Discharge Voltage Hall Thruster Characteristics And Evaluation Of Loss Mechanisms," The University of Michigan 2009, 2009.
[49] "TURBOVAC 1100 C." [Online]. Available: https://leyboldproducts.oerlikon.com/us/us/produktkatalog_04.aspx?cid=1839.
[50] B. C. Inc., "1cm RF Ion Thruster BIT-1."
[51] W. G. Tighe, K. Chien, and R. Spears, "XIPS © Ion Thrusters for Small Satellite Applications," in *21st Annual AIAA/USU Conference on Small Satellites*.
[52] D. M. Bui, "PLUME CHARACTERIZATION OF BUSEK 600W HALL THRUSTER," Air Force Institute of Technology, 2012.
[53] J. E. Foster and A. D. Gallimore, "The effect of an auxiliary discharge on anode

sheath potentials in a transverse discharge" vol. 3422, no. 1997, 2016.
[54] F. Stanley and G. Iii, "Examination Of The Structure And Evolution Of Ion Energy Properties Of A 5 Kw Class Laboratory Hall Effect Thruster At Various Operational Conditions," Univ. of Michigan, 1999.
[55] G. Aston, H. R. Kaufman, and P. J. Wilbur, "Ion Beam Divergence Characteristics of Two-Grid Accelerator Systems," *AIAA*, vol. 16, no. 5, pp. 516–524, 1978.

Appendix A

Electron Temperature Plots from Langmuir Probe Data

ELECTRON TEMPERATURE PLOTS FROM LANGMUIR PROBE DATA

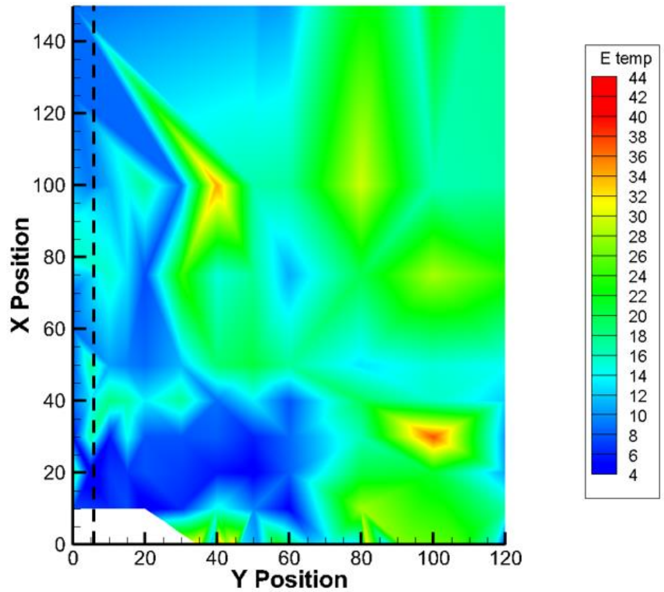

Figure 59: Electron Temperature in eV for 0° Thrust Vector

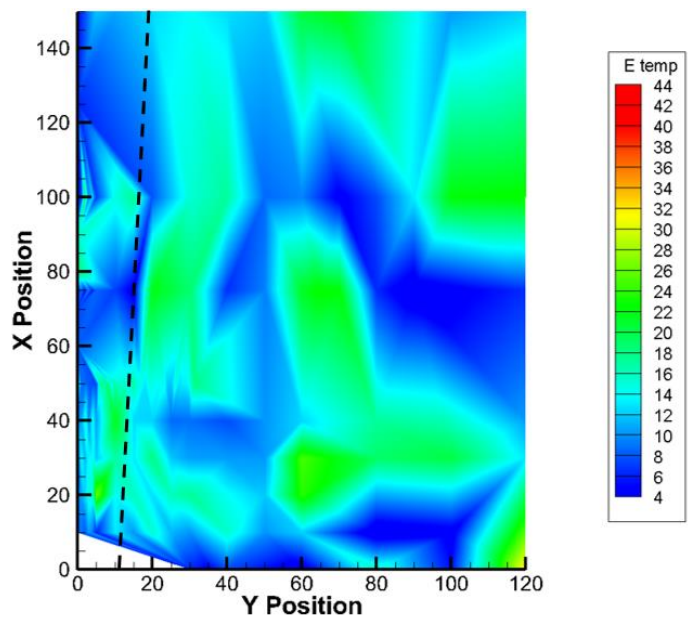

Figure 60: Electron Temperature in eV for 2.5° Thrust Vector

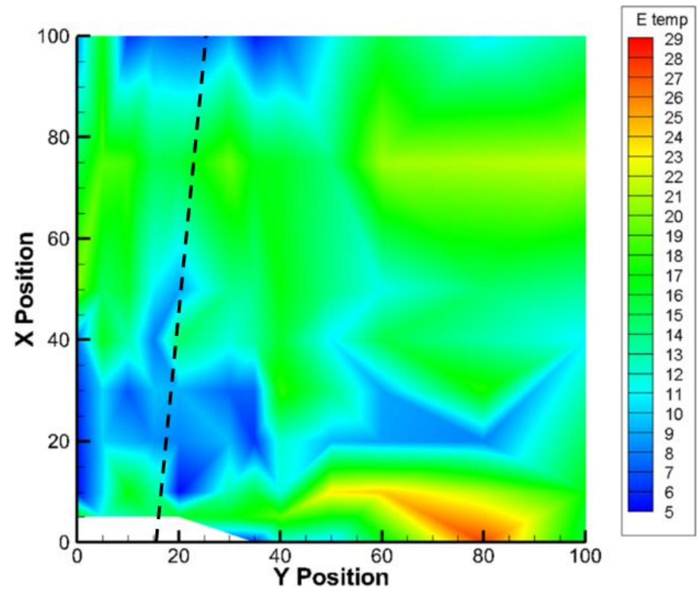

Figure 61: Electron Temperature in eV for 5° Thrust Vector

Appendix B

Ratio Probe Radius to Debye Length

RATIO PROBE RADIUS TO DEBYE LENGTH

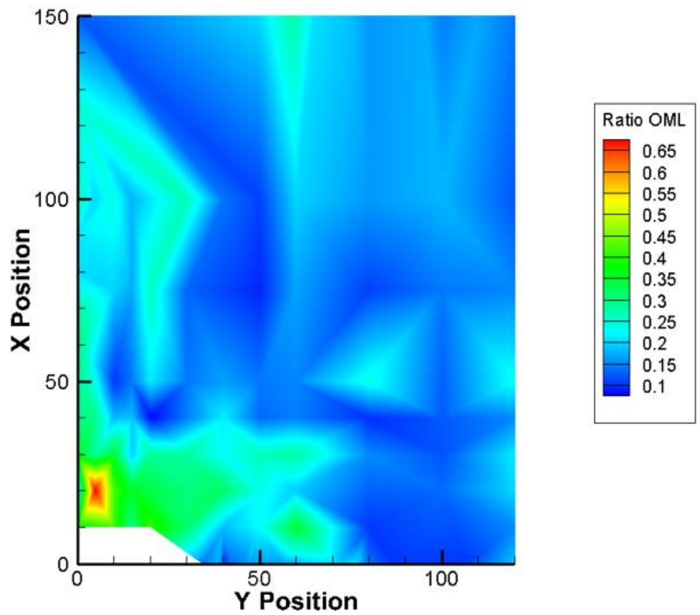

Figure 62: 0° Thrust Vector Ratio Probe Radius to Debye Length

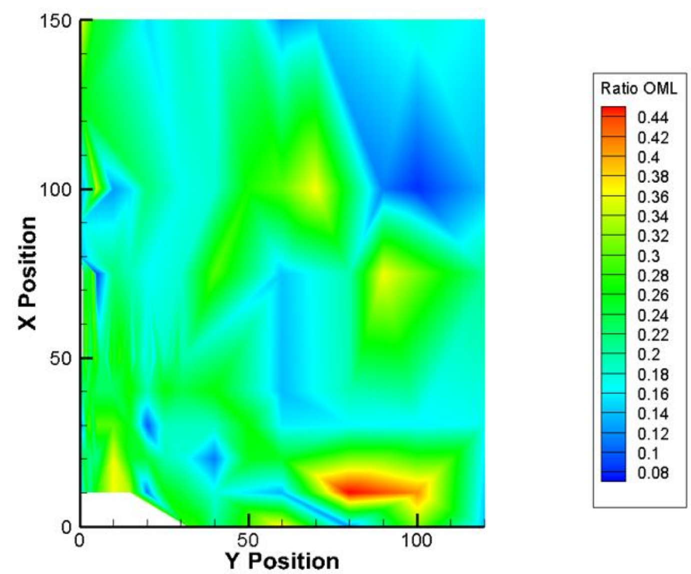

Figure 63: 2.5° Thrust Vector Ratio Probe Radius to Debye Length

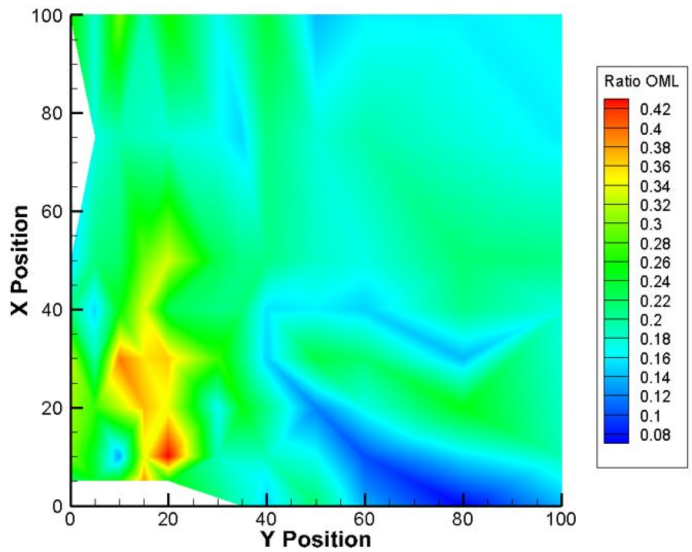

Figure 64: 5° Thrust Vector Ratio Probe Radius to Debye Length

Appendix C

Uncorrected Langmuir Probe Plot

UNCORRECTED LANGMUIR PROBE PLOT

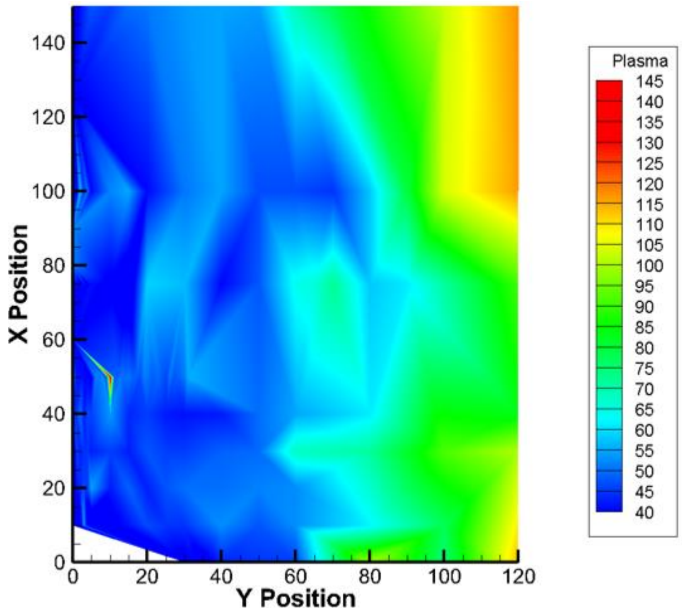

Figure 65: Plasma Potential 2.5° Thrust Vector

Appendix D

Data from Beam Target Experiment

DATA FROM BEAM TARGET EXPERIMENT

Table 8: Change in Thrust as a Function of Thruster Power

Forward Power	**Reverse Power**	**Screen Current**	**Beam Target**	**Calc Thrust**
W	**W**	**mA**	**mA**	**μN**
8.23	0.7	1.601	1.594	86.7
8.23	0.638	1.578	1.577	85.7
8.14	0.58	1.554	1.554	84.3
8.14	0.582	1.555	1.554	84.3
8.05	0.582	1.527	1.53	82.8
7.943	0.53	1.496	1.503	81.2
7.791	0.53	1.458	1.47	79.2
7.698	0.484	1.439	1.455	78.3
7.606	0.484	1.42	1.436	77.1
7.488	0.441	1.392	1.393	74.5
7.5	0.441	1.397	1.416	75.9
7.358	0.441	1.367	1.389	74.3
7.191	0.403	1.331	1358	72.4
6.975	0.367	1.288	1.32	70.1

Table 9: BIT-1 Operation Based on Varying Screen Grid Voltage

Screen Grid Voltage	Screen Grid Current	Beam Target Current	Corrected Beam Target Current	Calc Thrust
V	mA	mA	mA	µN
1200	1.420	1.792	1.36	65.2
1250	1.437	1.805	1.373	67.5
1300	1.450	1.814	1.382	69.5
1350	1.463	1.826	1.394	71.7
1400	1.477	1.836	1.404	73.7
1450	1.487	1.845	1.413	75.7
1500	1.498	1.861	1.429	78.1
1550	1.510	1.871	1.439	80.2
1600	1.522	1.882	1.450	82.3

Table 10: Collected Beam Target Current as a Function of Cathode Keeper Current

Keeper Voltage	Keeper Current	Beam Target	Corrected Current	Screen Current	Calc Thrust
V	A	mA	mA	mA	µN
12.5	2.8	1.93	1.516	1.646	91.9
12.6	2.75	1.91	1.536	1.646	93.2
12.6	2.7	1.902	1.505	1.646	91.3
12.9	2.6	1.869	1.475	1.642	89.5
13	2.51	1.854	1.472	1.643	89.3
13.3	2.4	1.825	1.452	1.64	88.1
13.5	2.3	1.807	1.447	1.639	87.8
13.8	2.2	1.786	1.437	1.637	87.2
14	2.1	1.767	1.432	1.637	86.8
14.3	2.05	1.753	1.432	1.629	86.8
14.4	2	1.743	1.394	1.628	84.5
14.5	2	1.739	1.379	1.625	83.6
17.2	1.9	1.724	1.41	1.623	85.5
16.8	1.8	1.709	1.408	1.625	85.4
17.1	1.75	1.7	1.406	1.617	85.3
17.3	1.65	1.71	1.49475	1.622	90.7
17.7	1.6	1.712	1.442	1.625	87.5
18	1.55	1.712	1.51375	1.623	91.8
18.2	1.5	1.715	1.486	1.622	90.1
18.9	1.4	1.706	1.487	1.625	90.2
19.2	1.3	1.683	1.482	1.625	89.9
19	1.2	1.645	1.469	1.625	89.1
19	1.1	1.617	1.453	1.622	88.1

Appendix E

Langmuir Probe Experiment Data

Data for 0° Thrust Vector

X	Y	Floating	Plasma	E temp	Density OML	Ion Sat Current	Density thin sheath
100	0	18.79649	41.12026	10.38445	3.07977E+15	-7.26216E-06	1.74585E+15
100	30	20.72931	41.32247	8.473798	2.57284E+15	-6.56411E-06	2.02257E+15
100	50	24.85485	56.57794	16.61942	8.30475E+14	-7.36372E-06	8.59231E+14
100	5	19.67087	41.16563	9.201464	1.57928E+15	-7.99132E-06	2.46727E+15
10	10	19.84856	37.27467	6.396331	4.59672E+15	-1.1463E-05	6.7312E+15
10	15	19.82459	39.24704	7.576565	2.84145E+15	-8.30038E-06	3.39303E+15
10	20	20.83508	33.05717	3.757759	2.61528E+15	-6.13746E-06	5.12635E+15
10	30	21.80508	40.2215	6.344225	2.62539E+15	-5.73556E-06	2.42357E+15
150	0	19.70812	42.09635	8.772492	5.52901E+14	-8.37508E-06	2.83487E+15
20	0	19.86698	48.44482	18.67903	3.66024E+15	-1.20193E-05	1.66683E+15
20	100	51.49621	106.864	20.91085	1.56225E+15	-5.33421E-06	3.16903E+14
20	10	19.70947	35.2335	6.878882	5.11602E+15	-1.3366E-05	7.71449E+15
20	15	19.7589	35.30637	6.769197	3.52958E+15	-1.1687E-05	6.48178E+15
20	20	20.84308	37.34808	7.69693	3.6462E+15	-9.89275E-06	4.33976E+15
20	30	21.7845	38.27514	6.991902	2.72844E+15	-9.3948E-06	4.52711E+15
20	40	22.79472	37.15007	5.648	2.38486E+15	-8.69784E-06	5.22536E+15
20	50	23.81375	40.29938	4.440434	1.04144E+15	-6.83433E-06	4.8799E+15
20	5	19.90545	29.0733	3.353749	6.68804E+15	-1.46119E-05	1.79928E+16
20	60	27.93712	51.50732	8.275046	1.31649E+15	-6.69678E-06	2.15795E+15
30	0	19.86278	34.18319	5.569043	2.88683E+15	-1.0481E-05	7.03763E+15
30	100	48.59664	146.9496	37.29915	2.27517E+15	-5.0994E-06	1.00599E+14
30	10	19.89407	32.11575	5.538983	2.77912E+15	-1.13107E-05	7.87019E+15
30	20	19.85561	40.22286	7.82852	2.70916E+15	-7.15218E-06	2.58148E+15
30	30	20.94777	42.41368	7.841272	2.62947E+15	-5.80206E-06	1.85068E+15
30	40	22.90483	45.39532	8.150435	1.71523E+15	-6.54748E-06	2.12617E+15
30	50	24.94871	44.30127	6.033579	1.78843E+15	-6.73773E-06	3.30668E+15
30	5	19.7283	46.56035	17.08426	5.80552E+15	-1.32907E-05	2.26698E+15
30	60	27.98289	51.65928	8.555467	2.85626E+15	-5.05991E-06	1.2794E+15
40	100	52.57537	102.8581	15.63598	1.00771E+15	-6.70456E-06	8.05154E+14
40	10	18.68868	48.38983	18.00316	2.51766E+15	-1.15943E-05	1.66033E+15
40	120	84.4633	146.9909	12.19149	1.22959E+15	-6.11448E-06	1.02306E+15
40	15	19.91642	48.39809	17.00196	2.52589E+15	-1.22773E-05	1.99885E+15
40	20	19.82324	44.45756	13.22267	3.17521E+14	-1.23246E-05	2.97257E+15
40	40	22.81314	43.40102	8.736782	1.69469E+15	-1.03533E-05	3.9564E+15
40	50	24.99882	50.63226	13.2847	9.7389E+14	-8.05449E-06	1.43179E+15
40	5	18.7625	42.32294	13.23885	4.92079E+15	-1.19005E-05	2.80523E+15
40	60	32.01525	54.69807	7.833679	7.12141E+14	-1.08607E-05	4.88281E+15
40	80	39.37218	86.31581	19.54741	7.86344E+14	-6.93809E-06	5.89994E+14
50	10	18.90349	42.44375	10.52677	4.64051E+14	-9.16651E-06	2.54699E+15
50	15	18.69979	42.24154	9.436024	7.90593E+14	-8.46957E-06	2.61305E+15
50	30	19.72003	46.5483	11.37027	9.52108E+14	-7.95996E-06	1.77657E+15
50	50	24.95791	63.91022	20.32113	1.72529E+15	-6.95226E-06	5.54386E+14
75	100	65.94678	111.8377	28.26445	2.38598E+15	-3.90059E-06	1.01253E+14
75	120	85.3255	118.0269	24.01017	2.28426E+15	-4.2583E-06	1.61878E+14
75	15	18.7973	48.48586	12.86707	1.63939E+15	-8.31234E-06	1.58566E+15
75	20	18.87152	38.25767	7.546063	2.13529E+15	-7.83618E-06	3.12269E+15
75	5	18.64345	45.41388	12.34235	2.62674E+15	-8.35386E-06	1.70293E+15
75	60	31.09239	59.6231	11.0648	1.30443E+15	-7.28036E-06	1.59527E+15
75	80	45.27587	101.7749	19.94112	9.93498E+14	-7.40065E-06	6.40441E+14
75	30	19.87701	56.49153	24.16561	1.74575E+15	-7.68279E-06	4.81067E+14
100	0	17.72261	33.96893	6.398797	3.1813E+15	-6.39254E-06	2.83183E+15
100	0	17.72532	33.79245	5.736345	2.84638E+15	-6.91711E-06	3.66329E+15
10	0	16.67704	33.12597	7.514744	4.18813E+15	-1.45744E-05	7.89038E+15
10	130	20.71265	39.7923	6.630734	2.19028E+15	-7.86298E-07	7.03224E+13
10	130	25.01331	46.45187	8.403135	1.60606E+15	-6.21331E-06	1.87428E+15
10	135	23.80535	41.33534	5.282992	2.34497E+15	-5.12686E-06	2.58874E+15
125	0	18.73338	37.25977	8.487993	2.23193E+15	-6.85699E-06	2.16318E+15
125	0	18.77604	38.93336	8.387966	2.45988E+15	-7.62717E-06	2.60113E+15
150	0	18.75816	38.16381	7.15442	8.11508E+14	-7.6736E-06	3.24082E+15
175	0	19.70148	42.20023	8.370996	1.9865E+15	-7.01318E-06	2.28519E+15
200	100	38.09921	111.7115	28.23479	1.48253E+15	-7.14435E-06	3.18783E+14
200	10	21.72138	40.19225	6.833922	2.86019E+15	-6.30591E-06	2.54389E+15
200	120	44.22231	99.51373	17.85814	2.01488E+15	-6.02569E-06	5.33787E+14
200	20	21.76567	41.18175	6.668368	2.04951E+15	-7.11225E-06	3.16004E+15
200	25	22.89806	39.14099	5.679162	3.2692E+15	-5.41055E-06	2.56061E+15
200	30	22.82438	39.15142	4.907498	2.94892E+15	-5.84501E-06	3.45491E+15

X	Y	Floating	Plasma	E temp	Density OML	Ion Sat Current	Density thin sheath
200	35	23.90733	38.077	4.689892	3.6109E+15	-4.98093E-06	2.87991E+15
200	40	23.8862	44.23598	6.687926	2.4352E+15	-6.63778E-06	2.8326E+15
200	45	23.81984	39.26248	3.318151	2.41947E+15	-6.50321E-06	6.33014E+15
200	50	26.03694	44.35002	5.175993	1.9061E+15	-6.92145E-06	4.15466E+15
200	55	27.05326	42.40623	3.598945	1.67571E+15	-6.42468E-06	5.71911E+15
200	5	20.82114	40.1871	6.543321	2.57314E+15	-6.67939E-06	2.9422E+15
200	60	27.85667	45.24526	4.346489	2.14345E+15	-6.43368E-06	4.5869E+15
200	70	31.01559	58.7586	11.22201	2.14827E+15	-6.68281E-06	1.353E+15
200	90	35.05351	77.95976	13.68862	1.64983E+15	-6.94874E-06	1.0616E+15
20	0	16.74937	27.03199	4.010898	3.33929E+15	-1.32363E-05	1.34659E+16
20	0	15.63391	29.09104	4.343509	5.28552E+15	-6.86335E-06	5.03432E+15
225	0	23.88052	45.27912	11.59877	2.28086E+15	-7.03747E-06	1.40355E+15
30	0	15.78208	48.35055	16.17603	3.60065E+15	-8.8037E-06	1.22493E+15
40	0	16.7923	36.04531	8.752751	3.11587E+15	-1.06605E-05	4.12723E+15
40	0	16.62842	37.18149	8.332366	3.53819E+15	-8.38378E-06	3.04183E+15
50	0	16.84119	35.02886	8.250812	2.8269E+15	-1.13956E-05	4.91907E+15
60	0	16.74652	38.0881	8.487363	3.31045E+15	-7.46128E-06	2.47282E+15
70	0	16.62043	37.15156	8.289346	2.70868E+15	-7.42948E-06	2.53639E+15
70	0	16.709	63.58855	30.6055	2.26043E+15	-7.80073E-06	3.24855E+14
75	0	17.78044	43.39614	11.55263	2.54623E+15	-7.73571E-06	1.6544E+15
75	0	17.69972	60.63644	27.6375	2.06432E+15	-8.03956E-06	4.12587E+14
80	0	17.78139	49.28385	15.62475	2.76943E+15	-6.97679E-06	8.64391E+14
90	0	17.79656	46.27417	14.50136	2.75004E+15	-7.12748E-06	1.01192E+15
90	0	17.83327	46.17246	13.57494	2.52768E+15	-7.4428E-06	1.21031E+15
0	34.5	20.68299	72.92801	32.39415	2.6589E+15	-4.96357E-06	1.2442E+14
0	40.5	20.65522	74.93261	35.43297	1.54355E+15	-6.25367E-06	1.63614E+14
0	44.5	19.29097	67.18061	31.68045	2.65414E+15	-1.05235E-06	6.15805E+12
0	56.5	20.85906	61.03977	22.38112	2.61792E+15	-3.12329E-07	1.10305E+12
0	71.5	26.29562	58.47148	13.96155	2.1462E+15	-2.82485E-06	2.00235E+14
0	86.5	32.41588	73.44876	12.79411	5.53754E+14	-3.78488E-06	4.07344E+14
0	91.5	43.14369	111.7884	26.7124	1.21906E+15	-6.84577E-06	3.25238E+14
0	106.5	49.31134	110.55	25.0074	1.06774E+15	-5.92221E-06	2.79439E+14
100	0	18.79649	44.33675	12.09233	2.80979E+15	-7.61061E-06	1.50264E+15
100	10	19.68563	44.35002	10.91578	2.58628E+15	-7.18452E-06	1.59247E+15
100	15	19.70541	49.42904	14.53598	1.96902E+15	-7.42292E-06	1.08145E+15
100	30	20.72931	44.30276	10.29203	2.57284E+15	-6.53566E-06	1.48557E+15
100	50	24.85485	57.7347	17.45363	2.22476E+15	-6.57189E-06	6.47923E+14
100	5	19.67087	40.35342	9.221121	2.07947E+15	-7.74517E-06	2.34083E+15
10	10	19.84856	43.48106	10.65653	4.77765E+15	-1.15708E-05	3.61681E+15
10	15	19.82459	42.39052	10.14606	3.08356E+15	-8.11622E-06	2.20726E+15
10	20	20.83508	47.47469	11.38445	2.86968E+15	-5.85941E-06	1.05891E+15
10	30	21.80508	71.13022	35.19175	3.02622E+15	-5.56166E-06	1.32485E+14
10	40	22.81233	53.66496	14.69249	2.10473E+15	-6.31251E-06	8.01818E+14
10	50	25.88403	51.48294	9.562454	2.02712E+15	-6.32598E-06	1.5701E+15
10	60	29.97341	45.34223	4.599589	2.33656E+15	-5.54429E-06	3.45723E+15
125	0	19.67534	46.36437	13.44621	2.66703E+15	-7.25101E-06	1.17483E+15
150	0	19.70812	43.29944	10.28554	1.14799E+15	-8.24296E-06	2.21976E+15
175	0	20.81802	41.2385	7.420718	7.52285E+14	-8.69991E-06	3.74348E+15
20	0	19.86698	39.29322	9.595769	3.68042E+15	-1.19292E-05	4.35215E+15
20	100	51.49621	108.936	27.0918	2.10405E+15	-4.85957E-06	1.66464E+14
20	10	19.70947	39.2106	9.923796	4.74083E+15	-1.38216E-05	5.21454E+15
20	120	82.43324	112.9805	10.67837	1.83161E+15	-5.28356E-06	9.80747E+14
20	140	108.8915	134.6922	9.163602	1.37863E+15	-5.78171E-06	1.44112E+15
20	150	109.096	140.8904	6.543556	1.22987E+15	-5.96257E-06	2.47053E+15
20	15	19.7589	39.37204	9.495634	3.18696E+15	-1.20065E-05	4.4551E+15
20	20	20.84308	40.22272	9.750323	3.03516E+15	-1.07435E-05	3.62786E+15
20	30	21.7845	45.35036	11.84526	2.78326E+15	-9.45105E-06	2.21982E+15
20	40	22.79472	48.49547	14.1009	2.00945E+15	-8.97217E-06	1.56798E+15
20	50	23.81375	54.76958	12.435	1.09779E+15	-6.86108E-06	1.20785E+15
20	5	19.90545	51.66957	22.58596	7.25493E+15	-1.45381E-05	1.713E+15
20	60	27.93712	65.87229	16.64056	1.31649E+15	-6.71739E-06	7.29225E+14
30	0	19.86278	41.4208	10.94978	2.94299E+15	-1.05207E-05	3.00214E+15
30	100	48.59664	100.6781	18.11859	1.84464E+15	-5.62765E-06	4.6047E+14
30	10	19.89407	40.20254	10.77306	4.40517E+15	-1.01716E-05	2.91033E+15
30	120	76.26422	112.9968	10.15607	1.94157E+15	-4.94745E-06	9.48023E+14
30	20	19.85561	45.54877	12.24275	2.24742E+15	-7.69141E-06	1.50105E+15
30	30	20.94777	51.51314	13.51279	3.20109E+15	-5.23462E-06	6.617E+14
30	40	22.90483	52.56101	13.02955	1.44106E+15	-6.99125E-06	1.15954E+15
30	50	24.94871	67.86633	21.65049	1.77604E+15	-6.77553E-06	4.63128E+14

X	Y	Floating	Plasma	E temp	Density OML	Ion Sat Current	Density thin sheath
30	5	19.7283	51.46574	24.14873	6.17913E+15	-1.30995E-05	1.28298E+15
30	60	27.98289	51.65928	8.822741	2.85626E+15	-5.19612E-06	1.27708E+15
30	80	38.14323	79.134	16.36132	1.61515E+15	-6.52353E-06	7.12057E+14
40	0	18.6857	45.52534	14.41579	4.35647E+15	-1.12976E-05	2.23079E+15
40	100	52.57537	102.8581	16.4805	1.3732E+15	-6.36983E-06	6.74435E+14
40	10	18.68868	41.40278	11.72536	3.46287E+15	-1.11244E-05	2.98452E+15
40	120	84.4633	123.2659	18.18078	1.99076E+15	-5.10661E-06	3.74362E+14
40	15	19.91642	44.30235	13.57629	3.16107E+15	-1.19396E-05	2.72131E+15
40	20	19.82324	48.4524	16.90842	1.85001E+15	-1.20365E-05	1.94956E+15
40	40	22.81314	51.6823	15.78604	9.66392E+14	-1.0846E-05	1.81672E+15
40	50	24.99882	57.61728	18.91353	1.5382E+15	-7.93168E-06	7.91691E+14
40	5	18.7625	42.32294	13.23874	5.02165E+15	-1.19578E-05	2.82703E+15
40	60	32.01525	59.67104	12.49508	1.1013E+15	-1.08523E-05	2.62441E+15
40	60	28.92987	86.48362	35.663	1.32683E+15	-6.93254E-06	1.96662E+14
40	80	39.37218	69.93824	7.185668	9.90821E+14	-6.85949E-06	2.71179E+15
50	10	18.90349	46.55412	13.56744	3.15676E+15	-8.09417E-06	1.39759E+15
50	15	18.69979	47.56299	13.1132	2.42656E+15	-7.8257E-06	1.39115E+15
50	50	24.95791	89.47488	45.66659	2.17266E+15	-6.82526E-06	1.20339E+14
50	5	18.66647	51.48389	17.26952	4.04458E+15	-7.92601E-06	9.18322E+14
75	0	18.81342	51.3536	17.48976	2.07214E+15	-8.5026E-06	1.01729E+15
75	10	18.84593	49.37202	15.33393	2.51417E+15	-8.19148E-06	1.17753E+15
75	120	85.3255	118.0269	13.28484	1.59502E+15	-5.77338E-06	8.07706E+14
75	15	18.7973	40.19089	8.430586	2.54778E+15	-7.92495E-06	2.74315E+15
75	20	18.87152	38.25767	7.545829	2.16573E+15	-7.85161E-06	3.13228E+15
75	30	19.87701	51.59467	17.74621	1.41899E+15	-7.94788E-06	8.82582E+14
75	50	24.93611	59.78738	17.30081	6.26919E+14	-7.88978E-06	9.0828E+14
75	5	18.64345	54.40837	19.8709	2.62124E+15	-8.28851E-06	7.88554E+14
75	60	31.09239	64.93127	15.21389	1.7378E+15	-7.0741E-06	9.24675E+14
75	80	45.27587	106.7956	25.1408	5.02245E+14	-7.70649E-06	4.51262E+14
100	5	19.67087	46.49778	12.6477	2.07947E+15	-7.76681E-06	1.45196E+15
125	0	19.67534	49.27071	14.56665	2.22632E+15	-7.66369E-06	1.13884E+15
150	0	19.70812	46.17639	11.43012	1.72492E+15	-7.99576E-06	1.77592E+15
175	0	20.81802	46.14226	11.69358	1.70839E+15	-8.37578E-06	1.85411E+15
30	15	19.83895	48.39674	14.17261	2.2524E+15	-8.36247E-06	1.38061E+15
50	30	19.72003	50.6133	15.01172	6.50024E+14	-8.09656E-06	1.19362E+15
0	120	52.3714	94.37174	6.528162	9.82816E+14	-6.80944E-06	3.03922E+15
0	80	37.12677	77.06967	14.04084	1.10654E+15	-6.93574E-06	1.0163E+15
100	0	18.87355	41.14545	10.39215	2.72335E+15	-6.96127E-06	1.62607E+15
100	100	35.15102	71.95598	16.32805	2.23889E+15	-6.05504E-06	6.25969E+14
100	120	38.15325	84.08679	16.78456	1.03089E+15	-6.80983E-06	7.36502E+14
100	140	39.27534	60.7609	4.922462	2.24102E+15	-4.582E-06	2.38897E+15
100	40	20.68976	73.02999	34.52307	2.86763E+15	-5.77307E-06	1.47446E+14
100	60	21.38699	54.65649	17.18275	2.87396E+15	-1.50344E-06	4.13914E+13
100	80	25.4677	73.49197	29.6512	3.26777E+15	-1.44143E-07	1.36056E+11
100	80	31.98844	73.85548	19.2259	1.81639E+15	-6.31995E-06	5.1305E+14
10	0	17.7023	45.29713	15.25747	3.39851E+15	-1.18059E-05	2.20514E+15
10	10	16.85853	45.39885	13.6537	5.64602E+15	-1.23719E-05	2.85872E+15
10	120	38.60479	73.92469	16.82819	1.67821E+15	-2.96899E-06	1.57014E+14
10	130	25.01331	46.45187	8.30263	1.38934E+15	-6.39424E-06	1.99565E+15
10	130	20.71265	55.02759	19.31364	2.96444E+15	5.15314E-07	-3.87115E+12
10	135	23.80535	51.36985	12.90538	2.35935E+15	-5.43064E-06	7.60725E+14
10	140	62.81331	110.6964	26.19015	2.06776E+15	1.07212E-08	-919049100
10	20	18.8141	50.52675	13.6377	1.99338E+15	-7.45303E-06	1.20443E+15
10	40	20.78971	52.39131	14.07869	2.31121E+15	-6.39501E-06	8.78952E+14
10	60	26.00159	82.23185	36.83397	2.32687E+15	-6.08234E-06	1.44367E+14
10	80	33.98708	84.27464	27.90419	1.26382E+15	-6.75013E-06	2.92848E+14
200	0	22.90334	56.32914	15.14788	1.63088E+15	-7.65771E-06	1.06868E+15
200	0	21.89014	38.26336	5.344403	2.49279E+15	-6.71578E-06	3.82385E+15
225	0	22.80257	58.50385	22.39665	2.29235E+15	-6.95846E-06	4.58305E+14
40	0	16.62842	45.17714	13.4213	3.5038E+15	-8.41803E-06	1.51872E+15
40	0	16.7923	36.04531	8.75425	3.55547E+15	-1.03879E-05	3.96635E+15
50	0	16.69438	41.24608	11.2466	2.23442E+15	-8.59466E-06	2.04903E+15
50	0	17.84478	48.28378	15.90238	3.21304E+15	-7.30981E-06	9.11422E+14
50	120	39.28049	66.86287	14.02043	3.18972E+15	-4.73061E-06	5.20289E+14
50	140	46.41679	83.08618	8.710242	1.91279E+15	-6.00477E-06	1.68613E+15
50	20	18.67026	40.13767	8.73429	1.6731E+15	-7.47925E-06	2.38668E+15
50	40	19.87335	55.46762	18.59609	2.1671E+15	-6.65083E-06	5.95024E+14
50	60	23.93022	61.80769	17.16756	1.63039E+15	-6.76931E-06	7.02003E+14
50	80	29.07817	59.54075	12.9323	3.07531E+15	-5.30471E-06	7.27692E+14

X	Y	Floating	Plasma	E temp	Density OML	Ion Sat Current	Density thin sheath
10	0	0	38.17451	11.26631	4.31323E+15	-1.31652E-05	4.1051E+15
150	0	0	41.11051	8.101631	2.66149E+15	-6.88474E-06	2.32113E+15
175	0	0	42.05315	13.61555	2.18311E+15	-7.03714E-06	1.0942E+15
200	0	0	56.46837	20.54955	3.36262E+15	-5.65358E-06	3.63926E+14
200	0	0	62.43409	20.9215	2.82043E+15	-6.19574E-06	4.17336E+14
200	15	0	44.27039	9.316146	1.66093E+15	-7.48165E-06	2.18378E+15
200	80	0	67.74552	14.71698	1.63169E+15	-6.54834E-06	8.52665E+14
225	0	0	61.74499	22.15019	3.41319E+15	-5.70062E-06	3.23509E+14
30	0	0	40.1462	13.13935	3.57751E+15	-1.02679E-05	2.18504E+15
50	0	0	43.41266	11.72249	2.99342E+15	-7.77119E-06	1.63094E+15
50	0	0	38.07375	8.803953	2.38086E+15	-8.4948E-06	2.88458E+15
60	0	0	43.29903	13.25687	2.67528E+15	-7.73758E-06	1.34187E+15
80	0	0	57.48103	28.68185	2.78247E+15	-7.56964E-06	3.4521E+14
90	0	0	46.44144	14.75069	3.24655E+15	-6.76436E-06	8.99035E+14
0	36.5	0	61.77262	20.77514	2.2656E+15	-5.54754E-06	3.44707E+14
0	38.5	0	47.44475	10.83965	1.46288E+15	-6.17685E-06	1.24933E+15
0	42.5	0	65.14364	27.90418	2.17672E+15	-1.77201E-06	2.19736E+13
0	46.5	0	50.44305	13.21956	1.49317E+15	-2.49395E-06	1.75145E+14
0	66.5	0	50.31344	12.08638	1.98301E+15	-1.16268E-06	4.89204E+13
0	76.5	0	53.8497	12.74257	2.32141E+15	-1.53884E-06	7.55992E+13
0	81.5	0	92.68487	31.3505	2.21372E+15	-1.98571E-06	2.19157E+13

Data for 0° Thrust Vector continued

X	Y	Debye OML	Debye thin sheath	Ratio OML	Ratio thin sheath
100	0	0.000431441	0.000573	0.264926182	0.132977
100	30	0.000426404	0.000481	0.268055778	0.158445
100	50	0.001051074	0.001033	0.108745865	0.073742
100	5	0.000567136	0.000454	0.201538856	0.167937
10	10	0.00027716	0.000229	0.412397603	0.332696
10	15	0.000383668	0.000351	0.297914026	0.217032
10	20	0.00028164	0.000201	0.405837136	0.378796
10	30	0.000365242	0.00038	0.312942827	0.200449
150	0	0.000935894	0.000413	0.122129271	0.184362
20	0	0.000530776	0.000787	0.215345061	0.09688
20	100	0.000859605	0.001909	0.132967993	0.039925
20	10	0.000272447	0.000222	0.419531696	0.343448
20	15	0.000325384	0.00024	0.351277586	0.317355
20	20	0.000341372	0.000313	0.334825671	0.243523
20	30	0.000376123	0.000292	0.303890223	0.260963
20	40	0.00036158	0.000244	0.316112496	0.311944
20	50	0.000485158	0.000224	0.235593268	0.339984
20	5	0.000166381	0.000101	0.686976032	0.751192
20	60	0.000589069	0.00046	0.194035135	0.165616
30	0	0.000326339	0.000209	0.350249371	0.364577
30	100	0.000951331	0.004524	0.120147494	0.016843
30	10	0.000331704	0.000197	0.344584713	0.386584
30	20	0.000399403	0.000409	0.286177265	0.186235
30	30	0.00040574	0.000484	0.281707297	0.157557
30	40	0.000512175	0.00046	0.223165915	0.165644
30	50	0.00043156	0.000317	0.264853236	0.240091
30	5	0.000403057	0.000645	0.283582746	0.118139
30	60	0.000406641	0.000608	0.28108308	0.125414
40	100	0.000925516	0.001035	0.12349871	0.073594
40	10	0.000628297	0.000774	0.181920383	0.098489
40	120	0.000739838	0.000811	0.15449326	0.093948
40	15	0.000609581	0.000685	0.187505925	0.1112
40	20	0.00151622	0.000496	0.075384814	0.15377
40	40	0.000533482	0.000349	0.214252898	0.218243
40	50	0.00086778	0.000716	0.131715409	0.106471
40	5	0.000385386	0.00051	0.296585439	0.149288
40	60	0.000779272	0.000298	0.146675449	0.256046
40	80	0.001171459	0.001352	0.097570651	0.056344
50	10	0.00111906	0.000478	0.102139251	0.159526
50	15	0.000811721	0.000446	0.140811863	0.170666
50	30	0.000811953	0.000594	0.140771631	0.128195
50	50	0.000806365	0.001423	0.141747292	0.053567
75	100	0.000808679	0.003926	0.14134163	0.019411
75	120	0.000761752	0.002861	0.150048772	0.02663
75	15	0.000658244	0.000669	0.173643707	0.11385
75	20	0.000441693	0.000365	0.258777211	0.208627
75	5	0.000509307	0.000633	0.224422637	0.120466
75	60	0.000684306	0.000619	0.167030544	0.123144
75	80	0.00105264	0.001311	0.108584085	0.058121
75	30	0.000874171	0.001665	0.130752402	0.045758
100	0	0.000333224	0.000353	0.343012744	0.21575
100	0	0.000333549	0.000294	0.342677823	0.25917
10	0	0.000314728	0.000229	0.363170569	0.332321
10	130	0.000408809	0.002282	0.279593004	0.033399
10	130	0.000537438	0.000497	0.212675651	0.153166
10	135	0.000352664	0.000336	0.324104964	0.227023
125	0	0.000458196	0.000465	0.249456597	0.163723
125	0	0.00043387	0.000422	0.26344287	0.1806
150	0	0.000697637	0.000349	0.163838713	0.218276
175	0	0.000482318	0.00045	0.236980714	0.169449
200	100	0.001025368	0.002211	0.111472201	0.034461
200	10	0.000363184	0.000385	0.314716602	0.19787
200	120	0.000699491	0.001359	0.163404421	0.05607
200	20	0.000423812	0.000341	0.269695146	0.223256
200	25	0.000309678	0.00035	0.369093079	0.217769
200	30	0.000303101	0.00028	0.377101736	0.272116

X	Y	Debye OML	Debye thin sheath	Ratio OML	Ratio thin sheath
200	35	0.00026777	0.0003	0.426858289	0.254141
200	40	0.000389374	0.000361	0.293548216	0.211064
200	45	0.000275155	0.00017	0.415402717	0.447945
200	50	0.00038718	0.000262	0.295211354	0.290561
200	55	0.000344332	0.000186	0.33194745	0.40883
200	5	0.000374676	0.00035	0.305063604	0.217472
200	60	0.000334581	0.000229	0.341621398	0.333163
200	70	0.000537006	0.000677	0.21284672	0.112611
200	90	0.000676782	0.000844	0.168887411	0.090317
20	0	0.000257503	0.000128	0.443878195	0.594241
20	0	0.000212993	0.000218	0.536637359	0.349153
225	0	0.000529841	0.000675	0.215725002	0.112817
30	0	0.000498006	0.000854	0.229515318	0.089246
40	0	0.000393796	0.000342	0.29025186	0.222702
40	0	0.000360564	0.000389	0.317003378	0.195952
50	0	0.000401404	0.000304	0.284750586	0.250415
60	0	0.000376211	0.000435	0.303818727	0.175056
70	0	0.000411027	0.000425	0.27808404	0.179396
70	0	0.000864557	0.002281	0.132206504	0.033413
75	0	0.000500473	0.000621	0.228383974	0.122729
75	0	0.000859705	0.001923	0.132952568	0.039625
80	0	0.000558085	0.000999	0.204807455	0.076281
90	0	0.00053954	0.000889	0.211846977	0.085671
90	0	0.000544499	0.000787	0.209917877	0.096838
0	34.5	0.000820109	0.003791	0.139371776	0.020099
0	40.5	0.001125726	0.003458	0.101534457	0.022038
0	44.5	0.00081175	0.016852	0.14080683	0.004522
0	56.5	0.000686992	0.033468	0.166377487	0.002277
0	71.5	0.000599268	0.001962	0.190732837	0.038839
0	86.5	0.001129368	0.001317	0.101207069	0.057868
0	91.5	0.001099847	0.002129	0.103923556	0.035786
0	106.5	0.00113708	0.002223	0.100520609	0.034283
100	0	0.000487424	0.000667	0.234498213	0.114324
100	10	0.000482701	0.000615	0.236792337	0.123872
100	15	0.00063839	0.000861	0.179044265	0.08846
100	30	0.000469929	0.000618	0.243228076	0.123214
100	50	0.000658098	0.001219	0.173682432	0.062486
100	5	0.000494771	0.000466	0.231015764	0.163403
10	10	0.000350905	0.000403	0.325729347	0.188939
10	15	0.000426198	0.000504	0.268185175	0.151267
10	20	0.000467981	0.00077	0.244240934	0.09891
10	30	0.000801234	0.003829	0.142655023	0.019899
10	40	0.000620781	0.001006	0.18412303	0.075763
10	50	0.000510309	0.00058	0.223981875	0.131415
10	60	0.000329655	0.000271	0.346726185	0.281171
125	0	0.000527564	0.000795	0.216656372	0.095864
150	0	0.000703287	0.000506	0.162522492	0.150663
175	0	0.000737939	0.000331	0.154890851	0.230346
20	0	0.000379385	0.000349	0.301277346	0.218413
20	100	0.000843101	0.002997	0.135570919	0.025422
20	10	0.000339939	0.000324	0.336236999	0.235091
20	120	0.000567316	0.000775	0.201475142	0.098286
20	140	0.000605756	0.000592	0.188689841	0.128612
20	150	0.000541959	0.000382	0.210901713	0.199276
20	15	0.000405567	0.000343	0.281827546	0.222143
20	20	0.000421122	0.000385	0.271417834	0.197825
20	30	0.000484713	0.000543	0.235809825	0.140395
20	40	0.000622406	0.000705	0.183642101	0.108147
20	50	0.000790772	0.000754	0.144542336	0.101077
20	5	0.000414564	0.000853	0.275711443	0.089315
20	60	0.000835343	0.001122	0.136830092	0.067891
30	0	0.000453207	0.000449	0.252202415	0.169816
30	100	0.000736369	0.001474	0.155221096	0.051702
30	10	0.000367432	0.000452	0.311077896	0.168565
30	120	0.000537372	0.000769	0.212702011	0.099086
30	20	0.000548385	0.000671	0.208430102	0.11356
30	30	0.000482739	0.001062	0.236774094	0.071767
30	40	0.0007065	0.000788	0.161783333	0.096749
30	50	0.000820344	0.001606	0.139331856	0.047433

X	Y	Debye OML	Debye thin sheath	Ratio OML	Ratio thin sheath
30	5	0.000464485	0.001019	0.246078733	0.074753
30	60	0.000412944	0.000618	0.276792806	0.123388
30	80	0.00074781	0.001126	0.152846343	0.067657
40	0	0.000427406	0.000597	0.267427305	0.127578
40	100	0.000813967	0.001161	0.140423405	0.065607
40	10	0.000432349	0.000466	0.264370047	0.163622
40	120	0.000710044	0.001637	0.160975915	0.046538
40	15	0.000486925	0.000525	0.234738192	0.145199
40	20	0.000710318	0.000692	0.160913774	0.110124
40	40	0.000949617	0.000693	0.120364266	0.110021
40	50	0.000823888	0.001148	0.138732418	0.066353
40	5	0.000381495	0.000508	0.299610554	0.149868
40	60	0.000791416	0.000513	0.144424736	0.148632
40	60	0.001218119	0.003164	0.093833227	0.024083
40	80	0.000632739	0.000382	0.180643082	0.199233
50	10	0.000487098	0.000732	0.23465484	0.104089
50	15	0.000546195	0.000721	0.20926605	0.105633
50	50	0.00107719	0.004577	0.106109445	0.016648
50	5	0.000485503	0.001019	0.235425813	0.074787
75	0	0.000682608	0.000974	0.167445985	0.078216
75	10	0.000580254	0.000848	0.196982792	0.089872
75	120	0.000678084	0.000953	0.16856325	0.079968
75	15	0.000427402	0.000412	0.267429774	0.184996
75	20	0.000438571	0.000365	0.260618945	0.20895
75	30	0.000830907	0.001054	0.137560546	0.072325
75	50	0.001234288	0.001025	0.092604028	0.074309
75	5	0.00064691	0.001179	0.176685968	0.064606
75	60	0.000695199	0.000953	0.164413348	0.079954
75	80	0.001662343	0.001754	0.068758393	0.04345
100	5	0.000579453	0.000693	0.197254854	0.109885
125	0	0.000601	0.00084	0.19018306	0.090681
150	0	0.000604826	0.000596	0.188980027	0.127836
175	0	0.000614709	0.00059	0.185941769	0.12914
30	15	0.000589375	0.000753	0.193934397	0.101223
50	30	0.001129118	0.000833	0.101229444	0.09145
0	120	0.000605547	0.000344	0.188754823	0.221285
0	80	0.000836955	0.000873	0.13656649	0.087253
100	0	0.000458975	0.000594	0.24903293	0.128287
100	100	0.000634512	0.0012	0.180138457	0.0635
100	120	0.000948064	0.001122	0.120561536	0.067936
100	140	0.000348222	0.000337	0.328238455	0.225933
100	40	0.000815234	0.003595	0.140205176	0.021195
100	60	0.000574507	0.004787	0.198953296	0.015918
100	80	0.000707757	0.109686	0.161496058	0.000695
100	80	0.000764412	0.001438	0.149526705	0.052979
10	0	0.000497835	0.000618	0.229593959	0.123294
10	10	0.000365378	0.000513	0.312826454	0.148398
10	120	0.000744019	0.002432	0.153625157	0.031327
10	130	0.00057437	0.000479	0.19900069	0.159001
10	130	0.000599721	0.003404	0.190588644	0.010154
10	135	0.000549513	0.000968	0.208002461	0.07874
10	140	0.000836195	0.091219	0.136690637	0.000413
10	20	0.000614561	0.000791	0.185986498	0.09638
10	40	0.000579896	0.00094	0.197104466	0.081034
10	60	0.000934818	0.003753	0.122269797	0.020304
10	80	0.00110403	0.002294	0.103529824	0.033224
200	0	0.000716067	0.000885	0.159621878	0.086142
200	0	0.00034403	0.000278	0.332238861	0.274326
225	0	0.000734413	0.001642	0.155634518	0.046393
40	0	0.000459851	0.000698	0.248558993	0.109096
40	0	0.00036868	0.000349	0.310024808	0.218299
50	0	0.000527129	0.00055	0.216835046	0.13843
50	0	0.000522711	0.000981	0.218667659	0.077642
50	120	0.000492599	0.00122	0.232034791	0.062475
50	140	0.000501384	0.000534	0.227969022	0.142691
50	20	0.000536837	0.000449	0.212913893	0.169531
50	40	0.000688271	0.001314	0.166068229	0.058013
50	60	0.000762425	0.001162	0.149916459	0.065582
50	80	0.000481817	0.00099	0.237226891	0.076931

X	Y	Debye OML	Debye thin sheath	Ratio OML	Ratio thin sheath
10	0	0.000379733	0.000389	0.301000924	0.195766
150	0	0.000409933	0.000439	0.278826038	0.173592
175	0	0.000586771	0.000829	0.194794792	0.091938
200	0	0.000580833	0.001766	0.19678641	0.043159
200	0	0.000639923	0.001664	0.178615215	0.045805
200	15	0.000556456	0.000485	0.205406935	0.157019
200	80	0.000705633	0.000976	0.161982154	0.078063
225	0	0.000598546	0.001944	0.190962764	0.039194
30	0	0.000450283	0.000576	0.253840512	0.132254
50	0	0.00046496	0.00063	0.24582782	0.120969
50	0	0.000451815	0.00041	0.252979693	0.185639
60	0	0.000523027	0.000739	0.218535392	0.103181
80	0	0.000754357	0.002142	0.151519714	0.03558
90	0	0.000500823	0.000952	0.228224488	0.080066
0	36.5	0.000711491	0.001824	0.160648636	0.041775
0	38.5	0.000639577	0.000692	0.178711947	0.110103
0	42.5	0.000841245	0.008373	0.135870023	0.009101
0	46.5	0.000699106	0.002041	0.163494636	0.03733
0	66.5	0.000580062	0.003693	0.197047964	0.020633
0	76.5	0.000550479	0.00305	0.207637171	0.02498
0	81.5	0.000884199	0.008887	0.129269603	0.008575

Thruster Conditions for 0° Thrust Vector Test

X	Y	Forward Power	Reverse Power	Screen Grid Current	Screen Grid Voltage	Accel Grid Current	Accel Grid Voltage
100	0	11.81076	1.449553	2.049535	1777.324	-0.19256	-198.494
100	30	11.80565	1.432032	2.015926	1775.898	-0.1857	-198.495
100	50	11.80298	1.444629	2.013911	1778.73	-0.18589	-198.5
100	5	11.80212	1.437202	2.018357	1781.259	-0.18762	-198.509
10	10	11.86907	1.480702	2.011112	1782.068	-0.18209	-198.507
10	15	11.87722	1.488517	2.01356	1781.338	-0.18029	-198.506
10	20	11.87211	1.483753	2.017491	1770.824	-0.17922	-198.51
10	30	11.87599	1.487598	2.015455	1780.948	-0.18004	-198.505
150	0	11.80207	1.462668	2.06487	1779.83	-0.19399	-198.484
20	0	11.87479	1.494552	2.024109	1767.258	-0.18205	-198.51
20	100	11.87439	1.492127	2.020069	1780.837	-0.18147	-198.514
20	10	11.88043	1.502445	2.024583	1770.102	-0.18221	-198.512
20	15	11.87356	1.495762	2.018956	1781.604	-0.18235	-198.508
20	20	11.87325	1.494511	2.024145	1776.399	-0.18261	-198.513
20	30	11.86552	1.494078	2.019044	1779.598	-0.18226	-198.505
20	40	11.87069	1.496197	2.020947	1766.863	-0.18018	-198.509
20	50	11.87116	1.494544	2.02089	1778.978	-0.18212	-198.503
20	5	11.87548	1.497811	2.020675	1780.99	-0.18394	-198.507
20	60	11.87339	1.494199	2.020246	1780.625	-0.18204	-198.502
30	0	11.88163	1.50222	2.02634	1779.997	-0.18377	-198.512
30	100	11.86058	1.481759	2.02472	1769.025	-0.1834	-198.503
30	10	11.86384	1.48575	2.028521	1763.443	-0.18313	-198.504
30	20	11.85532	1.481725	2.017627	1780.45	-0.18309	-198.507
30	30	11.85641	1.486013	2.018095	1780.232	-0.18318	-198.513
30	40	11.85898	1.479749	2.019576	1771.944	-0.18266	-198.504
30	50	11.85236	1.477386	2.018243	1773.368	-0.18299	-198.501
30	5	11.87106	1.494264	2.023705	1778.979	-0.1843	-198.519
30	60	11.85842	1.480532	2.016272	1780.696	-0.18322	-198.5
40	100	11.8571	1.483148	2.024574	1778.502	-0.18415	-198.504
40	10	11.86874	1.483261	2.023936	1779.368	-0.18584	-198.502
40	120	11.8605	1.485231	2.024895	1775.876	-0.18395	-198.503
40	15	11.87224	1.485913	2.021847	1780.965	-0.18599	-198.509
40	20	11.8745	1.486036	2.023993	1778.737	-0.18633	-198.52
40	40	11.86674	1.484634	2.020165	1775.71	-0.18491	-198.509
40	50	11.87076	1.489938	2.022162	1779.306	-0.18491	-198.513
40	5	11.87317	1.483985	2.021825	1780.769	-0.18554	-198.502
40	60	11.87092	1.488864	2.020165	1781.559	-0.18471	-198.508
40	80	11.8639	1.489204	2.02526	1778.436	-0.18434	-198.504
50	10	11.84337	1.474096	2.020621	1779.986	-0.18621	-198.499
50	15	11.84456	1.475689	2.019842	1780.369	-0.18619	-198.503
50	30	11.84952	1.478021	2.020962	1779.02	-0.18596	-198.499
50	50	11.8593	1.482171	2.02122	1780.093	-0.18625	-198.506
75	100	11.81105	1.445484	2.028653	1777.436	-0.18809	-198.494
75	120	11.80934	1.443864	2.024486	1775.211	-0.18724	-198.493
75	15	11.80495	1.44559	2.036529	1778.202	-0.19059	-198.502
75	20	11.81089	1.448068	2.034613	1779.856	-0.19054	-198.496
75	5	11.80948	1.444098	2.03695	1780.491	-0.19152	-198.51
75	60	11.80514	1.442145	2.030752	1777.56	-0.18886	-198.502
75	80	11.80276	1.44066	2.030088	1773.393	-0.18841	-198.497
75	30	11.815	1.446562	2.036105	1774.964	-0.18941	-198.488
100	0	12.26766	1.693544	2.156754	1783.941	-0.2466	-201.866
100	0	12.241	1.690766	2.165799	1788.248	-0.26843	-201.861
10	0	12.27633	1.688515	2.166564	1776.659	-0.25233	-201.866
10	130	12.2983	1.679267	2.133444	1788.913	-0.21716	-201.869
10	130	12.29549	1.684186	2.137818	1788.888	-0.21761	-201.863
10	135	12.29853	1.683849	2.13749	1788.775	-0.21811	-201.877
125	0	12.25999	1.690436	2.168231	1777.456	-0.24588	-201.877
125	0	12.23779	1.688918	2.171319	1780.472	-0.26464	-201.83
150	0	12.26619	1.688173	2.165626	1779.779	-0.24469	-201.866
175	0	12.26231	1.688992	2.159295	1782.14	-0.24354	-201.864
200	100	12.29065	1.681976	2.145044	1788.3	-0.23355	-201.878
200	10	12.26864	1.691148	2.156172	1782.233	-0.24078	-201.87
200	120	12.2983	1.687761	2.147189	1788.317	-0.23372	-201.873
200	20	12.27168	1.692775	2.149799	1784.964	-0.24017	-201.877
200	25	12.26787	1.687885	2.156862	1781.01	-0.23987	-201.88
200	30	12.27071	1.68964	2.161803	1776.603	-0.23889	-201.891

X	Y	Forward Power	Reverse Power	Screen Grid Current	Screen Grid Voltage	Accel Grid Current	Accel Grid Voltage
200	35	12.27508	1.691103	2.171604	1768.686	-0.23478	-201.86
200	40	12.273	1.684735	2.145263	1788.143	-0.23858	-201.858
200	45	12.27987	1.688477	2.167889	1770.386	-0.23533	-201.867
200	50	12.27391	1.681239	2.151966	1781.246	-0.23582	-201.861
200	55	12.27834	1.684426	2.151447	1783.194	-0.23546	-201.87
200	5	12.26772	1.687661	2.150284	1785.374	-0.24114	-201.855
200	60	12.28515	1.690326	2.147746	1788.136	-0.23629	-201.874
200	70	12.2752	1.684209	2.144806	1788.258	-0.23491	-201.866
200	90	12.27903	1.683559	2.145622	1788.327	-0.23398	-201.87
20	0	12.26646	1.685398	2.163355	1783.209	-0.25247	-201.836
20	0	12.27577	1.690786	2.153774	1783.297	-0.25362	-201.843
225	0	12.25676	1.6957	2.176337	1775.931	-0.25908	-201.857
30	0	12.27386	1.689882	2.16415	1779.351	-0.25515	-201.873
40	0	12.25319	1.675128	2.154101	1783.821	-0.24973	-201.845
40	0	12.2782	1.698178	2.170231	1777.502	-0.25627	-201.87
50	0	12.24589	1.67701	2.153498	1783.843	-0.24995	-201.846
60	0	12.25556	1.693575	2.172276	1774.878	-0.25557	-201.846
70	0	12.25939	1.680728	2.160248	1781.663	-0.2483	-201.855
70	0	12.25205	1.69144	2.167969	1777.836	-0.2563	-201.866
75	0	12.25665	1.680572	2.157087	1783.472	-0.2481	-201.862
75	0	12.25884	1.702195	2.186368	1769.946	-0.25731	-201.85
80	0	12.25225	1.693364	2.170658	1776.698	-0.25553	-201.85
90	0	12.26347	1.692056	2.162075	1777.144	-0.24425	-201.868
90	0	12.24959	1.697841	2.168285	1781.718	-0.25968	-201.86
0	34.5	12.29678	1.684236	2.137441	1789.027	-0.21942	-201.874
0	40.5	12.30222	1.681393	2.13944	1788.907	-0.21981	-201.864
0	44.5	12.29986	1.681548	2.136761	1788.921	-0.22108	-201.865
0	56.5	12.30396	1.683035	2.139012	1788.833	-0.22254	-201.862
0	71.5	12.30734	1.677091	2.139985	1785.763	-0.22262	-201.866
0	86.5	12.30525	1.683234	2.140366	1788.665	-0.22594	-201.858
0	91.5	12.30353	1.690393	2.170021	1763.813	-0.22233	-201.869
0	106.5	12.29924	1.687928	2.144237	1788.445	-0.22821	-201.871
100	0	11.81076	1.449553	2.049535	1777.324	-0.19256	-198.494
100	10	11.80991	1.441986	2.02265	1772.467	-0.18664	-198.503
100	15	11.80787	1.441551	2.018214	1780.709	-0.18668	-198.502
100	30	11.80565	1.432032	2.015926	1775.898	-0.1857	-198.495
100	50	11.80298	1.444629	2.013911	1778.73	-0.18589	-198.5
100	5	11.80212	1.437202	2.018357	1781.259	-0.18762	-198.509
10	10	11.86907	1.480702	2.011112	1782.068	-0.18209	-198.507
10	15	11.87722	1.488517	2.01356	1781.338	-0.18029	-198.506
10	20	11.87211	1.483753	2.017491	1770.824	-0.17922	-198.51
10	30	11.87599	1.487598	2.015455	1780.948	-0.18004	-198.505
10	40	11.8633	1.477699	2.010593	1781.035	-0.1798	-198.505
10	50	11.86118	1.481371	2.013069	1780.661	-0.18021	-198.509
10	60	11.87136	1.488333	2.016615	1780.182	-0.18092	-198.509
125	0	11.81912	1.461061	2.059842	1779.785	-0.19353	-198.496
150	0	11.80207	1.462668	2.06487	1779.83	-0.19399	-198.484
175	0	11.79787	1.462534	2.07118	1779.523	-0.19511	-198.501
20	0	11.87479	1.494552	2.024109	1767.258	-0.18205	-198.51
20	100	11.87439	1.492127	2.020069	1780.837	-0.18147	-198.514
20	10	11.88043	1.502445	2.024583	1770.102	-0.18221	-198.512
20	120	11.86824	1.483917	2.015596	1781.604	-0.1807	-198.508
20	140	11.86041	1.481323	2.015292	1780.805	-0.18084	-198.514
20	150	11.87424	1.494374	2.017259	1770.773	-0.17995	-198.512
20	15	11.87356	1.495762	2.018956	1781.604	-0.18235	-198.508
20	20	11.87325	1.494511	2.024145	1776.399	-0.18261	-198.513
20	30	11.86552	1.494078	2.019044	1779.598	-0.18226	-198.505
20	40	11.87069	1.496197	2.020947	1766.863	-0.18018	-198.509
20	50	11.87116	1.494544	2.02089	1778.978	-0.18212	-198.503
20	5	11.87548	1.497811	2.020675	1780.99	-0.18394	-198.507
20	60	11.87339	1.494199	2.020246	1780.625	-0.18204	-198.502
30	0	11.88163	1.50222	2.02634	1779.997	-0.18377	-198.512
30	100	11.86058	1.481759	2.02472	1769.025	-0.1834	-198.503
30	10	11.86384	1.48575	2.028521	1763.443	-0.18313	-198.504
30	120	11.85958	1.484167	2.02105	1780.443	-0.1844	-198.508
30	20	11.85532	1.481725	2.017627	1780.45	-0.18309	-198.507
30	30	11.85641	1.486013	2.018095	1780.232	-0.18318	-198.513
30	40	11.85898	1.479749	2.019576	1771.944	-0.18266	-198.504
30	50	11.85236	1.477386	2.018243	1773.368	-0.18299	-198.501

X	Y	Forward Power	Reverse Power	Screen Grid Current	Screen Grid Voltage	Accel Grid Current	Accel Grid Voltage
30	5	11.87106	1.494264	2.023705	1778.979	-0.1843	-198.519
30	60	11.85842	1.480532	2.016272	1780.696	-0.18322	-198.5
30	80	11.85762	1.481503	2.017029	1777.622	-0.18283	-198.509
40	0	11.87344	1.486092	2.025687	1774.016	-0.18581	-198.499
40	100	11.8571	1.483148	2.024574	1778.502	-0.18415	-198.504
40	10	11.86874	1.483261	2.023936	1779.368	-0.18584	-198.502
40	120	11.8605	1.485231	2.024895	1775.876	-0.18395	-198.503
40	15	11.87224	1.485913	2.021847	1780.965	-0.18599	-198.509
40	20	11.8745	1.486036	2.023993	1778.737	-0.18633	-198.52
40	40	11.86674	1.484634	2.020165	1775.71	-0.18491	-198.509
40	50	11.87076	1.489938	2.022162	1779.306	-0.18491	-198.513
40	5	11.87317	1.483985	2.021825	1780.769	-0.18554	-198.502
40	60	11.87092	1.488864	2.020165	1781.559	-0.18471	-198.508
40	60	11.86769	1.493007	2.024834	1775.209	-0.1843	-198.507
40	80	11.8639	1.489204	2.02526	1778.436	-0.18434	-198.504
50	10	11.84337	1.474096	2.020621	1779.986	-0.18621	-198.499
50	15	11.84456	1.475689	2.019842	1780.369	-0.18619	-198.503
50	50	11.8593	1.482171	2.02122	1780.093	-0.18625	-198.506
50	5	11.83084	1.462713	2.016819	1779.029	-0.18638	-198.503
75	0	11.80913	1.445327	2.041027	1778.888	-0.19166	-198.495
75	10	11.8132	1.449473	2.040622	1778.042	-0.191	-198.493
75	120	11.80934	1.443864	2.024486	1775.211	-0.18724	-198.493
75	15	11.80495	1.44559	2.036529	1778.202	-0.19059	-198.502
75	20	11.81089	1.448068	2.034613	1779.856	-0.19054	-198.496
75	30	11.815	1.446562	2.036105	1774.964	-0.18941	-198.488
75	50	11.81804	1.451718	2.032463	1777.446	-0.1892	-198.497
75	5	11.80948	1.444098	2.03695	1780.491	-0.19152	-198.51
75	60	11.80514	1.442145	2.030752	1777.56	-0.18886	-198.502
75	80	11.80276	1.44066	2.030088	1773.393	-0.18841	-198.497
100	5	11.80212	1.437202	2.018357	1781.259	-0.18762	-198.509
125	0	11.81912	1.461061	2.059842	1779.785	-0.19353	-198.496
150	0	11.80207	1.462668	2.06487	1779.83	-0.19399	-198.484
175	0	11.79787	1.462534	2.07118	1779.523	-0.19511	-198.501
30	15	11.86584	1.489477	2.021608	1772.497	-0.18314	-198.511
50	30	11.84952	1.478021	2.020962	1779.02	-0.18596	-198.499
0	120	12.30188	1.664942	2.123449	1789.27	-0.20346	-201.853
0	80	12.28878	1.663868	2.122601	1789.443	-0.20355	-201.866
100	0	12.29979	1.662917	2.120009	1788.792	-0.20511	-201.863
100	100	12.31759	1.667378	2.125187	1789.001	-0.20709	-201.869
100	120	12.31652	1.668083	2.127174	1788.961	-0.20776	-201.869
100	140	12.31342	1.663824	2.126212	1788.859	-0.20752	-201.87
100	40	12.30523	1.669761	2.124098	1788.911	-0.2059	-201.864
100	60	12.31141	1.669105	2.124093	1788.936	-0.20624	-201.871
100	80	12.30787	1.666313	2.126046	1788.977	-0.20627	-201.871
100	80	12.3141	1.670463	2.127161	1788.959	-0.20687	-201.87
10	0	12.30464	1.675002	2.126063	1789.263	-0.21322	-201.863
10	10	12.30531	1.67435	2.128937	1789.258	-0.21416	-201.867
10	120	12.30289	1.677931	2.132782	1789.223	-0.21392	-201.873
10	130	12.29549	1.684186	2.137818	1788.888	-0.21761	-201.863
10	130	12.2983	1.679267	2.133444	1788.913	-0.21716	-201.869
10	135	12.29853	1.683849	2.13749	1788.775	-0.21811	-201.877
10	140	12.29523	1.676095	2.132406	1789.08	-0.21417	-201.859
10	20	12.30344	1.670488	2.126337	1789.271	-0.21234	-201.865
10	40	12.30061	1.668565	2.12552	1789.254	-0.21206	-201.866
10	60	12.30766	1.672332	2.127341	1789.315	-0.21204	-201.859
10	80	12.3207	1.674463	2.129448	1789.368	-0.21245	-201.859
200	0	12.2814	1.693213	2.170084	1782.256	-0.26371	-201.868
200	0	12.26274	1.691282	2.152296	1784.477	-0.24234	-201.846
225	0	12.27124	1.691598	2.16133	1778.516	-0.24269	-201.89
40	0	12.2782	1.698178	2.170231	1777.502	-0.25627	-201.87
40	0	12.25319	1.675128	2.154101	1783.821	-0.24973	-201.845
50	0	12.26249	1.699092	2.167709	1777.32	-0.25471	-201.856
50	0	12.30633	1.671977	2.124536	1788.983	-0.20822	-201.865
50	120	12.30873	1.681066	2.132535	1789.12	-0.21074	-201.87
50	140	12.30936	1.674119	2.130984	1789.031	-0.21096	-201.867
50	20	12.30502	1.669723	2.125017	1789.068	-0.20835	-201.868
50	40	12.30151	1.668427	2.124912	1789.178	-0.20929	-201.88
50	60	12.30836	1.674268	2.127133	1789.106	-0.20853	-201.854
50	80	12.30657	1.674732	2.128049	1789.274	-0.2092	-201.867

X	Y	Forward Power	Reverse Power	Screen Grid Current	Screen Grid Voltage	Accel Grid Current	Accel Grid Voltage
10	0	12.28465	1.695192	2.157171	1782.15	-0.25297	-201.85
150	0	12.27029	1.696747	2.186682	1772.066	-0.26437	-201.859
175	0	12.282	1.697323	2.18415	1774.897	-0.26414	-201.865
200	0	12.26274	1.691282	2.152296	1784.477	-0.24234	-201.846
200	0	12.2814	1.693213	2.170084	1782.256	-0.26371	-201.868
200	15	12.26986	1.691796	2.16077	1777.523	-0.23813	-201.853
200	80	12.28938	1.685072	2.146156	1788.283	-0.23456	-201.864
225	0	12.27124	1.691598	2.16133	1778.516	-0.24269	-201.89
30	0	12.26059	1.676882	2.157812	1782.811	-0.25035	-201.822
50	0	12.25525	1.675937	2.155811	1781.575	-0.24838	-201.857
50	0	12.26249	1.699092	2.167709	1777.32	-0.25471	-201.856
60	0	12.2563	1.67976	2.164509	1776.992	-0.24809	-201.881
80	0	12.26525	1.691981	2.17715	1770.437	-0.24658	-201.891
90	0	12.26877	1.69302	2.160178	1781.64	-0.2481	-201.896
0	36.5	12.30692	1.687274	2.141403	1788.929	-0.21967	-201.866
0	38.5	12.30533	1.678927	2.134873	1788.941	-0.21939	-201.865
0	42.5	12.29624	1.680941	2.137076	1787.32	-0.22002	-201.869
0	46.5	12.30077	1.683178	2.139607	1788.94	-0.22191	-201.865
0	66.5	12.30484	1.676185	2.139368	1785.923	-0.22225	-201.861
0	76.5	12.31336	1.682372	2.141754	1785.65	-0.22382	-201.87
0	81.5	12.31045	1.684619	2.140161	1788.73	-0.22545	-201.869

Data for 2.5° Thrust Vector

X Position	Y Position	Floating	Plasma	E temp	Density OML	Ion Sat Current	Density thin sheath
100	0	22.80406	39.37624	6.031803	1.1E+15	-7.3E-06	3.75E+15
100	0	21.82255	40.33744	7.592148	1.61E+15	-6.7E-06	2.42E+15
100	100	47.3918	103.9057	22.21199	6.14E+14	-6.8E-06	4.4E+14
100	10	21.83	51.70031	14.6008	9.5E+14	-7.5E-06	1.09E+15
100	120	58.66922	116.3133	22.73381	1.79E+15	-5.6E-06	3.04E+14
100	140	70.02912	115.2774	19.02444	3.18E+14	-6.8E-06	5.96E+14
100	15	21.7933	54.76471	17.31477	1.68E+15	-7.1E-06	7.59E+14
100	20	21.76405	40.3438	7.853484	1.55E+15	-7E-06	2.5E+15
100	30	21.92996	50.46323	15.11283	1.85E+15	-6.7E-06	8.43E+14
100	40	22.80637	54.57103	17.19327	2.38E+15	-6.1E-06	5.84E+14
100	50	24.02801	46.45092	8.548446	2.68E+15	-5.6E-06	1.51E+15
100	5	21.86576	40.25997	6.922084	3.54E+15	-4.9E-06	1.67E+15
100	60	25.86724	46.42153	9.51432	3.56E+15	-3.6E-06	6.05E+14
100	70	29.98817	44.49684	4.295974	2.4E+15	-5.5E-06	3.66E+15
100	90	41.24432	79.38848	13.13345	6.94E+14	-6.8E-06	1.1E+15
125	0	22.89467	39.18812	6.185764	1.8E+15	-6.5E-06	3.02E+15
150	0	23.942	37.15562	5.089163	2.9E+15	-5E-06	2.64E+15
200	0	25.88173	59.8677	19.73906	2.94E+15	-5.6E-06	3.88E+14
200	0	21.92102	36.08012	9.942524	6.42E+14	1.43E-07	-1.1E+12
20	0	19.87118	34.08744	9.233629	1.08E+15	-8.9E-07	4.81E+13
225	0	28.01648	47.36214	5.97732	1.25E+15	-7E-06	3.52E+15
30	0	20.91567	34.20378	8.100125	5.88E+14	-3.2E-06	6.48E+14
50	1	23.00708	41.40779	8.537314	2.14E+15	-1.1E-05	4.31E+15
50	2	21.82228	41.38937	8.744106	3.37E+15	-9.2E-06	3.3E+15
50	3	22.87422	40.38944	7.851527	1.4E+15	-1.1E-05	5.14E+15
50	4	21.93578	40.34272	7.928951	2.38E+15	-1.1E-05	4.95E+15
50	5	21.93971	38.2211	7.152704	2.4E+15	-9.6E-06	4.56E+15
75	10	21.79425	38.15853	7.141112	1.43E+15	-1.1E-05	5.26E+15
75	120	48.41137	90.47467	6.516966	1.18E+15	-6.1E-06	2.57E+15
75	15	21.81145	31.999	3.997289	6.24E+14	-7.9E-06	6.76E+15
75	1	22.80637	41.28698	8.808486	2.21E+15	-1.1E-05	4.14E+15
75	20	21.97533	58.68953	21.95709	2.54E+15	-6.9E-06	4.64E+14
75	30	21.75768	56.75766	18.69398	2.57E+15	-6.7E-06	5.93E+14
75	3	22.88749	42.41653	9.309011	2.43E+15	-1.1E-05	3.76E+15
75	40	22.96794	40.22624	6.532564	2.41E+15	-6.3E-06	2.67E+15
75	4	22.79093	36.23749	5.587682	2.21E+15	-7.8E-06	4.48E+15
75	5	22.94641	41.43773	8.474417	2.71E+14	-1.1E-05	4.69E+15
75	60	24.97986	63.8918	21.24125	1.83E+15	-6.4E-06	4.34E+14
75	80	35.31246	57.69096	6.310161	1.02E+15	-6.6E-06	3.02E+15
75	90	39.40712	60.90474	2.856258	1.58E+15	-6.2E-06	6.9E+15
80	0	21.74102	50.6305	18.84917	1.53E+15	-6.9E-06	6.17E+14
90	0	21.95014	51.69056	15.84268	1.67E+15	-6.9E-06	8.26E+14
75	90	39.40712	79.3083	13.58109	1.58E+15	-6.3E-06	9.06E+14
100	0	20.88967	40.1378	9.0841	1.13E+15	-9.2E-06	3.15E+15
200	0	27.78732	71.61562	19.8671	1.5E+15	-8.9E-06	8.91E+14
50	0	19.86414	51.44122	16.50072	2.55E+15	-9.1E-06	1.25E+15
50	10	19.86861	146.912	17.44759	4.49E+15	-7.9E-06	8.93E+14
50	11	19.92942	48.38617	15.02824	4.33E+15	-8.1E-06	1.19E+15
50	12	19.82581	48.44157	15.26024	5.05E+15	-7.1E-06	9.21E+14
50	13	19.84816	50.60422	15.41047	4.15E+15	-8.2E-06	1.17E+15
50	14	19.84301	49.62163	15.29475	4.54E+15	-7.2E-06	9.35E+14
50	15	19.71543	50.6867	16.94562	4E+15	-7.8E-06	9.25E+14
50	16	19.72518	48.46378	14.784	2.01E+15	-9.6E-06	1.64E+15
50	17	19.82093	48.48518	14.6281	3.28E+15	-8E-06	1.22E+15
50	18	19.87863	46.41557	12.76366	2.14E+15	-9.2E-06	1.91E+15
50	19	19.75024	50.69944	14.60311	1.85E+15	-8.7E-06	1.42E+15
50	1	19.6878	49.36633	14.89758	1.14E+15	-9.7E-06	1.63E+15
50	20	20.88127	50.5147	14.54638	2.06E+15	-8.9E-06	1.46E+15
50	21	20.97025	48.58892	14.2553	2.54E+15	-8.3E-06	1.35E+15
50	22	20.73134	48.43466	13.7259	1.38E+15	-8.6E-06	1.53E+15
50	23	20.98894	49.49825	14.55751	2.92E+15	-7.6E-06	1.13E+15
50	24	20.97729	47.55161	12.02776	2.31E+15	-7.9E-06	1.63E+15
50	25	20.79215	46.379	11.73131	1.75E+15	-8.4E-06	1.87E+15
50	26	20.74339	50.52906	15.12527	2.75E+15	-7E-06	9.24E+14
50	27	20.76317	47.61012	12.64711	2.08E+15	-8.1E-06	1.56E+15
50	28	20.82208	48.41936	13.31387	2.64E+15	-7.3E-06	1.22E+15
50	29	21.76513	49.46222	13.21257	3.04E+15	-6.9E-06	1.12E+15

X Position	Y Position	Floating	Plasma	E temp	Density OML	Ion Sat Current	Density thin sheath
50	2	19.90436	50.36897	15.64095	2.73E+15	-8.8E-06	1.28E+15
50	30	21.92318	50.66747	14.59403	2.44E+15	-7.2E-06	1.02E+15
50	31	21.77867	55.83479	18.07804	2.94E+15	-6.6E-06	6.22E+14
50	3	19.66897	46.46311	12.869	2.79E+15	-8.9E-06	1.79E+15
50	4	19.90965	146.5885	16.05026	3.31E+15	-8.3E-06	1.12E+15
50	5	19.89204	49.56231	14.98178	3.45E+15	-8.3E-06	1.24E+15
50	6	19.74089	51.44772	17.49338	3.43E+15	-8.5E-06	1.01E+15
50	7	19.81254	50.59921	16.67707	3.51E+15	-8.6E-06	1.13E+15
50	8	19.70229	52.58607	18.71691	2.78E+15	-9.4E-06	1.08E+15
50	9	19.81024	46.53042	13.20493	4.44E+15	-7.5E-06	1.28E+15
0	100	55.61877	75.17315	5.401934	2.27E+15	-4E-06	1.72E+15
0	120	76.34603	113.0902	32.07444	2.55E+15	-3.7E-06	7.24E+13
0	140	96.71601	120.2756	7.393639	1.89E+15	-4.1E-06	1.13E+15
0	32	21.8514	39.44071	5.823981	1.94E+15	-5.8E-06	2.77E+15
0	35	22.00431	36.24061	4.503858	1.47E+15	-6.2E-06	4.14E+15
0	40	23.04433	43.33777	7.571346	1.34E+15	-6E-06	2.05E+15
0	60	29.03768	45.56801	3.288273	1.95E+15	-5E-06	4.51E+15
0	80	49.59481	99.74384	15.57904	9.66E+14	-5.7E-06	6E+14
100	1	22.75165	38.1179	6.403293	4.96E+14	-6.5E-06	2.89E+15
100	2	22.91336	57.71696	19.43517	2.15E+15	-5.9E-06	4.41E+14
100	3	22.95873	44.46311	9.116958	2.1E+15	-6.1E-06	1.57E+15
100	4	22.89413	49.4048	12.32611	2.63E+15	-5.8E-06	9.14E+14
100	5	22.94776	44.46663	9.181268	1.91E+15	-6.7E-06	1.85E+15
10	0	18.65117	31.13424	8.448822	1.25E+15	-2.7E-06	4.44E+14
10	100	50.65582	77.28515	3.850338	2.75E+15	-8.2E-06	7.43E+15
10	10	18.69451	37.34049	13.23429	7.35E+15	-1.3E-05	3.39E+15
10	15	18.82087	41.4793	10.2182	4.69E+15	-1.4E-05	5.35E+15
10	15	18.71956	33.06191	9.249191	3.06E+15	-8.2E-06	2.54E+15
10	1	18.82209	34.24373	9.004302	1.35E+15	-1.9E-06	1.99E+14
10	20	19.84694	46.4711	15.39752	7.77E+14	-1.2E-05	2.36E+15
10	25	20.95156	44.51431	11.1742	3.25E+15	-9.5E-06	2.48E+15
10	2	18.77563	32.03814	7.783601	2.04E+15	-2.4E-06	4.15E+14
10	30	21.74928	44.48736	10.08169	2.46E+15	-8.1E-06	2.21E+15
10	3	18.74841	54.57374	10.39714	1.92E+15	-5.5E-06	1.09E+15
10	40	22.85174	52.57984	15.49277	2.01E+15	-9.9E-06	1.62E+15
10	4	18.70615	31.99805	9.087189	2.25E+15	-5.2E-06	1.2E+15
10	5	18.80976	30.15571	5.984304	1.88E+15	-6.7E-06	3.32E+15
10	60	28.04763	52.54991	12.13463	9.4E+14	-1E-05	2.59E+15
10	60	25.89947	66.90825	19.81717	1.97E+15	-6E-06	4.31E+14
10	80	41.41687	61.83559	2.663137	2.44E+15	-9E-06	1.2E+16
150	0	24.86501	51.59779	15.40816	1.87E+15	-8.1E-06	1.15E+15
150	100	55.70951	102.8061	10.37388	1.37E+15	-6E-06	1.29E+15
150	10	23.88634	45.42255	10.72963	2.44E+15	-8.9E-06	2.37E+15
150	140	98.85646	131.5323	14.20258	1.23E+15	-5.7E-06	7.12E+14
150	15	23.9867	49.61851	11.5951	1.84E+15	-6.5E-06	1.23E+15
150	20	22.95291	50.64025	12.59321	1.26E+15	-6.8E-06	1.16E+15
150	30	23.99415	53.60699	13.87362	2.07E+15	-6.1E-06	8.19E+14
150	40	25.02198	54.61667	12.67114	1.45E+15	-6.8E-06	1.15E+15
150	50	26.94775	53.72076	11.83381	1.91E+15	-6E-06	1.05E+15
150	5	25.03931	47.3895	11.743	3.01E+15	-9.2E-06	2.16E+15
150	60	30.0391	69.07375	20.66057	1.34E+15	-6.3E-06	4.44E+14
150	70	33.11243	78.34074	22.01629	1.87E+15	-6.1E-06	3.69E+14
20	0	19.87795	49.59346	16.93959	3.8E+15	-9.9E-06	1.39E+15
20	10	18.64169	42.19414	13.83022	7.56E+15	-1.3E-05	3.02E+15
20	15	18.81505	48.56576	15.96678	4.24E+15	-1.1E-05	1.96E+15
20	1	19.87714	41.40888	10.80062	2.69E+15	-1.2E-05	3.6E+15
20	20	19.86387	42.36736	12.66066	3.18E+15	-1.1E-05	2.71E+15
20	25	19.74766	47.52263	16.15266	2.57E+15	-1E-05	1.65E+15
20	2	18.85446	43.23795	12.34291	2.73E+15	-1.2E-05	3.13E+15
20	30	20.71861	49.62908	17.35555	2.38E+15	-1E-05	1.45E+15
20	3	18.66309	46.30343	15.35157	2.76E+15	-1.1E-05	1.88E+15
20	40	21.92765	49.60429	14.02853	7.5E+14	-8.9E-06	1.56E+15
20	4	18.85053	45.29307	14.89568	3.24E+15	-1.2E-05	2.5E+15
20	50	23.79722	51.56935	11.87267	3.33E+15	-9.1E-06	2.1E+15
20	5	18.7667	54.51185	26.5389	4.81E+15	-1.2E-05	8.78E+14
20	60	18.72092	52.43343	23.81557	6.38E+15	-8.7E-06	6.34E+14
30	0	19.8017	47.45234	15.53737	3.56E+15	-1.1E-05	1.9E+15
30	100	42.28908	91.56237	20.19777	2.2E+15	-5.1E-06	3.15E+14
30	10	19.86129	45.4797	16.77615	6.34E+15	-1.2E-05	1.9E+15
30	120	51.61743	100.8254	13.00797	1.55E+15	-5.4E-06	7.5E+14

X Position	Y Position	Floating	Plasma	E temp	Density OML	Ion Sat Current	Density thin sheath
30	140	59.67064	114.9991	18.59187	1.59E+15	-5.2E-06	3.71E+14
30	15	19.70161	42.45567	13.11334	3.53E+15	-1.3E-05	3.24E+15
30	1	19.67263	45.33004	13.62803	1.1E+15	-1.2E-05	2.88E+15
30	20	19.70107	47.33925	18.02906	7.57E+14	-8.9E-06	1.04E+15
30	25	19.65638	45.32679	11.77734	1.79E+15	-7.3E-06	1.47E+15
30	2	19.73886	42.39919	11.4364	3.71E+15	-1.1E-05	3.06E+15
30	3	19.67642	44.38524	13.67905	4.84E+15	-1E-05	2.05E+15
30	40	21.89027	48.46283	10.35711	1.54E+15	-6.4E-06	1.43E+15
30	4	19.80048	44.44469	13.88426	2.91E+15	-1.2E-05	2.71E+15
30	50	23.79505	49.41238	10.26943	3.04E+15	-4.6E-06	8.11E+14
30	5	19.84355	42.36831	11.75714	4.36E+15	-9.7E-06	2.39E+15
30	60	25.8476	67.9461	24.85603	2.61E+15	-5E-06	2.09E+14
30	80	33.0164	71.04191	18.87548	2.14E+15	-5.3E-06	3.69E+14
40	0	22.96821	43.2542	9.754474	2.84E+15	-1.1E-05	3.74E+15
40	10	22.95765	53.57517	21.68364	4.67E+15	-1.1E-05	1.14E+15
40	140	78.29131	115.2171	13.27349	2.06E+15	-4.1E-06	4.4E+14
40	15	22.75558	43.44883	12.49944	3.92E+15	-1.1E-05	2.65E+15
40	1	22.87232	44.40135	10.65548	2E+15	-1.2E-05	3.74E+15
40	20	22.86406	45.34548	12.29982	1.98E+15	-1.2E-05	3.07E+15
40	25	23.79045	42.314	8.620786	2.5E+15	-1.1E-05	4.58E+15
40	2	22.86244	49.59075	15.06093	3.2E+15	-1.1E-05	2.03E+15
40	30	23.92724	41.30093	8.748694	2.03E+15	-7.7E-06	2.5E+15
40	3	22.91864	42.42547	9.821572	2.86E+15	-1.2E-05	4.14E+15
40	40	24.96374	42.20701	7.633011	2.25E+15	-8.5E-06	3.5E+15
40	4	22.82844	46.35273	14.50414	3.56E+15	-1.1E-05	2.22E+15
40	5	22.7633	45.52033	10.39511	2.3E+15	-1.2E-05	4.17E+15
40	60	30.12401	54.52336	12.43496	1.01E+15	-1E-05	2.33E+15
40	80	36.15799	60.86478	17.18955	2.71E+15	-9.2E-06	1.19E+15

Data for 2.5° Thrust Vector continued.

X Position	Y Position	Debye OML	Debye thin sheath	Ratio OML	Ratio thin sheath
100	0	0.000551	0.000298	0.207598	0.255682
100	0	0.00051	0.000416	0.224211	0.183118
100	100	0.001413	0.001669	0.080903	0.045665
100	10	0.000921	0.00086	0.12407	0.088555
100	120	0.000838	0.002034	0.136329	0.037472
100	140	0.001816	0.001328	0.06294	0.057384
100	15	0.000753	0.001122	0.151731	0.067923
100	20	0.000529	0.000416	0.216242	0.183113
100	30	0.000671	0.000995	0.170321	0.076615
100	40	0.000632	0.001275	0.180945	0.059755
100	50	0.00042	0.000559	0.272205	0.136207
100	5	0.000328	0.000479	0.348025	0.159211
100	60	0.000384	0.000932	0.297727	0.081785
100	70	0.000315	0.000254	0.363248	0.299502
100	90	0.001022	0.000813	0.111843	0.093756
125	0	0.000435	0.000336	0.262728	0.226649
150	0	0.000311	0.000326	0.367493	0.233633
200	0	0.000608	0.001676	0.187856	0.045472
200	0	0.000925	0.004234	0.12363	0.008273
20	0	0.000687	0.003257	0.166278	0.023396
225	0	0.000515	0.000306	0.222035	0.248941
30	0	0.000872	0.000831	0.131073	0.091728
50	1	0.00047	0.00033	0.243369	0.230564
50	2	0.000378	0.000382	0.302081	0.199299
50	3	0.000557	0.00029	0.205108	0.262353
50	4	0.000429	0.000297	0.2667	0.256314
50	5	0.000406	0.000294	0.28152	0.258946
75	10	0.000525	0.000274	0.217565	0.278217
75	120	0.000553	0.000374	0.206703	0.203672
75	15	0.000595	0.000181	0.192259	0.421879
75	1	0.000469	0.000343	0.243649	0.222384
75	20	0.00069	0.001617	0.165597	0.047138
75	30	0.000634	0.001319	0.180362	0.057759
75	3	0.00046	0.00037	0.248409	0.206191
75	40	0.000387	0.000367	0.295595	0.207387
75	4	0.000374	0.000262	0.305818	0.290339
75	5	0.001313	0.000316	0.087032	0.241233
75	60	0.000801	0.001643	0.142668	0.046368
75	80	0.000584	0.00034	0.19574	0.224383
75	90	0.000315	0.000151	0.362307	0.504114
80	0	0.000825	0.001299	0.138494	0.058657
90	0	0.000725	0.001029	0.157711	0.074035
75	90	0.000688	0.00091	0.166153	0.083753
100	0	0.000668	0.000399	0.171196	0.191057
200	0	0.000855	0.001109	0.133734	0.06868
50	0	0.000598	0.000854	0.19115	0.089276
50	10	0.000463	0.001038	0.246827	0.073381
50	11	0.000438	0.000835	0.261216	0.091304
50	12	0.000408	0.000956	0.27984	0.079673
50	13	0.000453	0.000852	0.252328	0.089475
50	14	0.000431	0.000951	0.264918	0.080167
50	15	0.000484	0.001005	0.23623	0.075791
50	16	0.000638	0.000706	0.179232	0.107864
50	17	0.000496	0.000813	0.230505	0.09377
50	18	0.000573	0.000607	0.199324	0.125531
50	19	0.000661	0.000753	0.172955	0.101253
50	1	0.000849	0.000709	0.134575	0.107432
50	20	0.000624	0.000741	0.183179	0.102791
50	21	0.000557	0.000763	0.205187	0.099917
50	22	0.00074	0.000703	0.154468	0.108427
50	23	0.000524	0.000842	0.21797	0.090522
50	24	0.000536	0.000639	0.213095	0.119339
50	25	0.000609	0.000589	0.187682	0.129352
50	26	0.000551	0.000951	0.207429	0.080154
50	27	0.000579	0.00067	0.197466	0.113739
50	28	0.000528	0.000777	0.216478	0.098062
50	29	0.00049	0.000806	0.23343	0.094521

X Position	Y Position	Debye OML	Debye thin sheath	Ratio OML	Ratio thin sheath
50	2	0.000563	0.000821	0.203142	0.092802
50	30	0.000575	0.000891	0.198779	0.085546
50	31	0.000583	0.001267	0.19621	0.060162
50	3	0.000504	0.00063	0.226655	0.120868
50	4	0.000518	0.000888	0.22076	0.085826
50	5	0.000489	0.000817	0.233551	0.093225
50	6	0.000531	0.000976	0.215348	0.078059
50	7	0.000512	0.000904	0.223089	0.084267
50	8	0.000609	0.000977	0.187619	0.078025
50	9	0.000405	0.000755	0.282114	0.100905
0	100	0.000362	0.000417	0.315318	0.182827
0	120	0.000834	0.004944	0.137067	0.015414
0	140	0.000465	0.000602	0.245778	0.126508
0	32	0.000407	0.000341	0.280514	0.223663
0	35	0.000412	0.000245	0.277462	0.311116
0	40	0.000559	0.000452	0.204311	0.168695
0	60	0.000305	0.000201	0.374711	0.379681
0	80	0.000944	0.001197	0.121134	0.06366
100	1	0.000844	0.00035	0.135412	0.217872
100	2	0.000706	0.00156	0.161814	0.048834
100	3	0.000489	0.000565	0.233593	0.134754
100	4	0.000508	0.000863	0.224861	0.088291
100	5	0.000515	0.000523	0.221762	0.14571
10	0	0.00061	0.001025	0.187305	0.074311
10	100	0.000278	0.000169	0.41088	0.450622
10	10	0.000315	0.000465	0.362433	0.16403
10	15	0.000347	0.000325	0.329479	0.234744
10	15	0.000408	0.000448	0.279808	0.169993
10	1	0.000607	0.001579	0.188385	0.048254
10	20	0.001046	0.000601	0.109308	0.126892
10	25	0.000436	0.000499	0.262433	0.152745
10	2	0.000458	0.001017	0.249347	0.074901
10	30	0.000476	0.000502	0.240366	0.151876
10	3	0.000547	0.000726	0.208881	0.104931
10	40	0.000652	0.000728	0.175254	0.104718
10	4	0.000472	0.000646	0.24214	0.118033
10	5	0.000419	0.000315	0.272967	0.241651
10	60	0.000844	0.000509	0.135398	0.14971
10	60	0.000746	0.001592	0.153275	0.047851
10	80	0.000245	0.000111	0.46596	0.68837
150	0	0.000675	0.000862	0.169383	0.088433
150	100	0.000647	0.000667	0.176613	0.114188
150	10	0.000493	0.0005	0.231962	0.152355
150	140	0.000797	0.001049	0.143403	0.072616
150	15	0.00059	0.000721	0.19386	0.105754
150	20	0.000744	0.000775	0.153729	0.098376
150	30	0.000608	0.000967	0.188091	0.078803
150	40	0.000694	0.000779	0.164614	0.097791
150	50	0.000585	0.00079	0.195409	0.096483
150	5	0.000464	0.000548	0.246213	0.139141
150	60	0.000923	0.001603	0.123837	0.047535
150	70	0.000805	0.001816	0.141915	0.04196
20	0	0.000496	0.00082	0.230433	0.092888
20	10	0.000318	0.000503	0.359725	0.151563
20	15	0.000456	0.000671	0.250539	0.11353
20	1	0.000471	0.000407	0.242844	0.187347
20	20	0.000469	0.000508	0.243878	0.149978
20	25	0.000589	0.000735	0.194154	0.103609
20	2	0.000499	0.000467	0.22896	0.163275
20	30	0.000634	0.000813	0.180228	0.09376
20	3	0.000554	0.000672	0.206453	0.113452
20	40	0.001016	0.000704	0.112506	0.108231
20	4	0.000504	0.000574	0.226715	0.132839
20	50	0.000443	0.000559	0.257729	0.136309
20	5	0.000552	0.001292	0.207002	0.058986
20	60	0.000454	0.00144	0.251769	0.05293
30	0	0.000491	0.000672	0.23275	0.113323
30	100	0.000711	0.00188	0.160714	0.040528
30	10	0.000382	0.000698	0.299125	0.109125
30	120	0.000681	0.000979	0.167815	0.077849

X Position	Y Position	Debye OML	Debye thin sheath	Ratio OML	Ratio thin sheath
30	140	0.000802	0.001662	0.142465	0.045841
30	15	0.000453	0.000473	0.252536	0.161082
30	1	0.000827	0.000511	0.138161	0.149074
30	20	0.001147	0.000977	0.09965	0.07803
30	25	0.000603	0.000665	0.189524	0.114587
30	2	0.000413	0.000454	0.277022	0.167753
30	3	0.000395	0.000606	0.289502	0.125669
30	40	0.00061	0.000633	0.187466	0.120326
30	4	0.000513	0.000532	0.222863	0.143189
30	50	0.000432	0.000836	0.264487	0.091158
30	5	0.000386	0.000521	0.296301	0.146207
30	60	0.000725	0.002562	0.157642	0.029744
30	80	0.000698	0.00168	0.163861	0.045357
40	0	0.000435	0.00038	0.262648	0.200704
40	10	0.000506	0.001025	0.225736	0.074356
40	140	0.000596	0.001291	0.191814	0.05902
40	15	0.00042	0.00051	0.272337	0.149303
40	1	0.000542	0.000397	0.211008	0.192179
40	20	0.000585	0.00047	0.195326	0.162092
40	25	0.000437	0.000322	0.261754	0.236389
40	2	0.000509	0.000639	0.224345	0.119177
40	30	0.000487	0.000439	0.234503	0.173448
40	3	0.000436	0.000362	0.262438	0.210572
40	40	0.000433	0.000347	0.26393	0.219562
40	4	0.000474	0.000601	0.241153	0.12686
40	5	0.0005	0.000371	0.228598	0.205439
40	60	0.000823	0.000543	0.138845	0.140282
40	80	0.000591	0.000893	0.193259	0.085364

Thruster Conditions for 2.5° Thrust Condition

X Position	Y Position	Forward Power	Reverse Power	Screen Grid Current	Screen Grid Voltage	Accel Grid Current	Accel Grid Voltage
100	0	11.86672	1.48298	2.013921	1777.967	-0.17723	-198.514
100	0	11.86552	1.483746	2.012644	1780.521	-0.1789	-198.513
100	100	11.87798	1.484447	2.015805	1771.59	-0.17496	-198.504
100	10	11.86602	1.48655	2.01365	1781.398	-0.17737	-198.516
100	120	11.87928	1.480573	2.011935	1781.677	-0.17608	-198.519
100	140	11.88372	1.480441	2.012354	1775.644	-0.17566	-198.522
100	15	11.87022	1.488838	2.019054	1769.162	-0.17632	-198.514
100	20	11.87914	1.486167	2.014312	1778.812	-0.17636	-198.513
100	30	11.87401	1.482623	2.010331	1773.836	-0.1752	-198.511
100	40	11.87502	1.482202	2.010512	1781.463	-0.1765	-198.514
100	50	11.87437	1.484132	2.010799	1773.025	-0.17515	-198.505
100	5	11.86442	1.482979	2.011798	1768.754	-0.17613	-198.514
100	60	11.87644	1.487593	2.018117	1766.994	-0.17541	-198.517
100	70	11.86536	1.474368	2.007975	1781.533	-0.17579	-198.518
100	90	11.86187	1.475358	2.009339	1781.673	-0.17553	-198.507
125	0	11.86776	1.486431	2.015702	1777.245	-0.17894	-198.511
150	0	11.8661	1.485355	2.010901	1780.971	-0.17862	-198.511
200	0	11.86794	1.491967	2.013011	1780.263	-0.17893	-198.508
200	0	11.8687	1.490254	2.0137	1780.793	-0.17791	-198.515
20	0	11.88764	1.492751	2.014853	1764.095	-0.17561	-198.514
225	0	11.87401	1.494338	2.015042	1772.745	-0.17836	-198.515
30	0	11.88236	1.486775	2.014396	1778.548	-0.17774	-198.508
50	1	11.86439	1.48375	2.011771	1776.894	-0.17359	-198.517
50	2	11.86523	1.482398	2.009063	1782.15	-0.17439	-198.524
50	3	11.88228	1.487933	2.010517	1782.818	-0.1744	-198.525
50	4	11.87129	1.48506	2.01488	1768.289	-0.17392	-198.522
50	5	11.85977	1.480797	2.009342	1781.966	-0.17426	-198.523
75	10	11.85472	1.474193	2.005327	1781.62	-0.17398	-198.516
75	120	11.87004	1.475021	2.008131	1781.819	-0.1752	-198.519
75	15	11.86058	1.478545	2.014234	1767.077	-0.17366	-198.522
75	1	11.85524	1.476197	2.007453	1781.675	-0.17403	-198.525
75	20	11.86063	1.475094	2.005934	1776.609	-0.17435	-198.514
75	30	11.86597	1.47812	2.012845	1770.676	-0.17381	-198.516
75	3	11.85432	1.476264	2.007287	1781.902	-0.17458	-198.529
75	40	11.86465	1.479632	2.017011	1769.084	-0.1739	-198.509
75	4	11.85928	1.48127	2.009368	1781.755	-0.17499	-198.528
75	5	11.86187	1.479456	2.008954	1770.202	-0.17318	-198.516
75	60	11.87061	1.477597	2.007614	1781.784	-0.17509	-198.521
75	80	11.8643	1.474879	2.007047	1781.83	-0.17516	-198.521
75	90	11.87352	1.479122	2.014716	1769.11	-0.17461	-198.519
80	0	11.86677	1.483105	2.012838	1780.314	-0.17838	-198.511
90	0	11.87181	1.486445	2.012901	1774.2	-0.1777	-198.513
75	90	11.87352	1.479122	2.014716	1769.11	-0.17461	-198.519
100	0	10.99849	1.244868	2.140893	1788.526	-0.17078	-199.436
200	0	10.98811	1.252917	2.155488	1788.231	-0.17292	-199.438
50	0	10.99369	1.237058	2.129518	1789.77	-0.17025	-199.44
50	10	11.01644	1.237647	2.113038	1787.623	-0.16788	-199.443
50	11	11.01479	1.237645	2.107983	1790.668	-0.1682	-199.45
50	12	11.01577	1.240013	2.110974	1789.97	-0.16792	-199.44
50	13	11.00365	1.230928	2.105041	1790.281	-0.16681	-199.436
50	14	10.99661	1.227284	2.102574	1790.114	-0.16692	-199.439
50	15	11.00062	1.228201	2.10404	1789.407	-0.16701	-199.442
50	16	10.99487	1.227823	2.101735	1790.538	-0.16645	-199.437
50	17	10.99963	1.231276	2.102807	1790.526	-0.1666	-199.438
50	18	10.98834	1.226219	2.102383	1789.112	-0.16638	-199.451
50	19	11.00202	1.234655	2.107153	1789.02	-0.16674	-199.443
50	1	11.00213	1.238681	2.124353	1790.509	-0.1703	-199.445
50	20	10.98839	1.227028	2.099573	1790.823	-0.16657	-199.446
50	21	10.98787	1.226728	2.101076	1788.744	-0.16625	-199.453
50	22	10.99706	1.232107	2.105106	1789.324	-0.16666	-199.448
50	23	11.01161	1.24045	2.106427	1790.829	-0.16697	-199.443
50	24	10.99602	1.231241	2.100897	1790.872	-0.16649	-199.442
50	25	10.98878	1.226415	2.098588	1790.855	-0.16621	-199.454
50	26	10.98867	1.22661	2.098824	1790.903	-0.16622	-199.454
50	27	10.97987	1.221727	2.096769	1790.847	-0.16624	-199.458
50	28	10.97877	1.220429	2.095085	1790.797	-0.16585	-199.454

X Position	Y Position	Forward Power	Reverse Power	Screen Grid Current	Screen Grid Voltage	Accel Grid Current	Accel Grid Voltage
50	29	11.00372	1.226802	2.098071	1790.724	-0.16582	-199.452
50	2	11.01635	1.243282	2.124994	1789.482	-0.16977	-199.437
50	30	11.01931	1.230167	2.101276	1790.811	-0.16656	-199.457
50	31	11.01319	1.226194	2.09873	1790.879	-0.16635	-199.466
50	3	11.0194	1.243277	2.126112	1787.672	-0.16944	-199.435
50	4	11.01844	1.241011	2.118912	1788.715	-0.16897	-199.443
50	5	11.01115	1.234638	2.112939	1790.481	-0.1688	-199.444
50	6	11.01018	1.233041	2.1114	1789.102	-0.16854	-199.446
50	7	11.00797	1.231487	2.108155	1789.676	-0.16787	-199.437
50	8	11.00806	1.232875	2.107928	1790.022	-0.16833	-199.45
50	9	11.00912	1.23305	2.106953	1790.555	-0.16822	-199.446
0	100	11.88959	1.493694	2.004127	1681.924	-0.16222	-198.503
0	120	11.89868	1.500771	2.022465	1659.025	-0.16276	-198.504
0	140	11.8853	1.493459	2.000685	1692.59	-0.16217	-198.505
0	32	11.88653	1.492833	2.015766	1664.892	-0.1622	-198.502
0	35	11.88892	1.497527	2.002074	1674.635	-0.16149	-198.503
0	40	11.8896	1.497552	2.005119	1675.272	-0.1614	-198.507
0	60	11.88228	1.493277	2.014399	1666.589	-0.162	-198.503
0	80	11.88256	1.492975	2.010048	1681.088	-0.16409	-198.509
100	1	11.87259	1.478665	2.012313	1743.19	-0.16533	-198.511
100	2	11.87041	1.478753	2.015175	1742.754	-0.16582	-198.513
100	3	11.87506	1.487869	2.020341	1743.544	-0.16706	-198.518
100	4	11.87069	1.483506	2.011926	1748.719	-0.16659	-198.524
100	5	11.85856	1.47446	2.003998	1759.4	-0.16644	-198.513
10	0	11.88775	1.494871	2.015925	1660.375	-0.1634	-198.512
10	100	11.87363	1.500803	2.017563	1663.208	-0.16301	-198.505
10	10	11.88304	1.499381	2.020002	1653.677	-0.16466	-198.513
10	15	11.87737	1.497088	2.022603	1657.969	-0.16358	-198.511
10	15	11.88618	1.502702	2.023325	1658.344	-0.16352	-198.512
10	1	11.88554	1.492557	2.008108	1668.553	-0.16258	-198.513
10	20	11.87757	1.495723	2.020828	1662.221	-0.16215	-198.507
10	25	11.87306	1.497098	2.043604	1649.287	-0.16319	-198.517
10	2	11.89068	1.496366	2.011517	1665.466	-0.16269	-198.508
10	30	11.88456	1.500339	2.0141	1659.186	-0.16399	-198.517
10	3	11.89711	1.503362	2.015025	1663.874	-0.16246	-198.502
10	40	11.89766	1.505904	2.033372	1650.117	-0.16479	-198.507
10	4	11.88567	1.500004	2.007652	1671.354	-0.1619	-198.503
10	5	11.88152	1.496167	2.012754	1671.976	-0.16088	-198.504
10	60	11.87706	1.500502	2.010695	1668.933	-0.16172	-198.506
10	60	11.88572	1.49957	2.039813	1646.188	-0.16361	-198.508
10	80	11.87562	1.502628	2.013782	1666.631	-0.16224	-198.51
150	0	11.85739	1.477041	2.007769	1781.413	-0.17238	-198.526
150	100	11.86437	1.48646	2.013584	1781.537	-0.17208	-198.521
150	10	11.86075	1.484124	2.011129	1778.649	-0.17214	-198.521
150	140	11.85547	1.482945	2.011523	1781.695	-0.17209	-198.515
150	15	11.86016	1.482227	2.009897	1781.401	-0.17243	-198.52
150	20	11.8658	1.488222	2.013319	1777.135	-0.17198	-198.518
150	30	11.86452	1.48371	2.010089	1781.4	-0.17252	-198.518
150	40	11.86257	1.483689	2.016911	1765.334	-0.17102	-198.516
150	50	11.86017	1.480091	2.009311	1781.656	-0.17245	-198.512
150	5	11.85888	1.479788	2.009253	1781.399	-0.17251	-198.525
150	60	11.85981	1.48397	2.015522	1762.797	-0.17127	-198.517
150	70	11.8625	1.484089	2.01238	1781.572	-0.1726	-198.523
20	0	11.88071	1.488895	2.008413	1675.938	-0.16212	-198.512
20	10	11.89001	1.502106	2.02722	1664.907	-0.16243	-198.501
20	15	11.89551	1.500708	2.013409	1676.88	-0.16133	-198.506
20	1	11.87867	1.486463	1.999318	1676.791	-0.1618	-198.514
20	20	11.89507	1.504974	2.024667	1656.468	-0.16306	-198.499
20	25	11.89819	1.508426	2.026218	1653.842	-0.16399	-198.515
20	2	11.87939	1.490072	2.010762	1672.67	-0.16218	-198.512
20	30	11.89853	1.51122	2.025912	1658.883	-0.16274	-198.501
20	3	11.88077	1.491146	2.012502	1671.372	-0.16205	-198.503
20	40	11.89782	1.511114	2.017443	1659.78	-0.16253	-198.507
20	4	11.88532	1.496389	2.014849	1666.629	-0.16292	-198.504
20	50	11.89592	1.509561	2.016945	1657.548	-0.16275	-198.508
20	5	11.8812	1.49062	2.01311	1674.526	-0.16172	-198.502
20	60	11.88522	1.494079	2.008341	1670.907	-0.16235	-198.503
30	0	11.88117	1.486787	2.01812	1664.357	-0.16171	-198.503
30	100	11.88663	1.490059	2.025008	1665.558	-0.16174	-198.508

X Position	Y Position	Forward Power	Reverse Power	Screen Grid Current	Screen Grid Voltage	Accel Grid Current	Accel Grid Voltage
30	10	11.89194	1.492856	2.009836	1674.172	-0.16238	-198.509
30	120	11.88616	1.48849	2.025522	1665.609	-0.16156	-198.512
30	140	11.8904	1.490355	2.012166	1677.233	-0.16326	-198.509
30	15	11.89058	1.494676	2.013981	1669.863	-0.16306	-198.512
30	1	11.88665	1.483882	2.002857	1671.519	-0.16145	-198.509
30	20	11.88152	1.489067	2.007665	1672.498	-0.16229	-198.505
30	25	11.88326	1.491966	2.015315	1669.897	-0.16196	-198.511
30	2	11.88864	1.488426	2.010331	1668.972	-0.16201	-198.505
30	3	11.88814	1.489593	2.009706	1665.784	-0.16311	-198.506
30	40	11.88692	1.487951	2.022623	1661.992	-0.16265	-198.51
30	4	11.88629	1.488217	2.01456	1662.891	-0.16308	-198.502
30	50	11.8869	1.489791	2.003593	1678.955	-0.1618	-198.502
30	5	11.88641	1.485729	2.019885	1665.152	-0.16248	-198.508
30	60	11.88982	1.490194	2.016409	1667.651	-0.16166	-198.496
30	80	11.88968	1.490849	2.018746	1670.459	-0.16137	-198.51
40	0	11.86983	1.479261	1.998093	1717.564	-0.16288	-198.52
40	10	11.8739	1.483648	2.034181	1687.082	-0.16461	-198.51
40	140	11.893	1.493818	2.025862	1682.096	-0.16286	-198.515
40	15	11.87519	1.4824	2.00736	1701.439	-0.16366	-198.507
40	1	11.87305	1.481792	2.005596	1714.785	-0.16295	-198.509
40	20	11.87745	1.482412	2.010898	1695.964	-0.16409	-198.511
40	25	11.88113	1.485397	2.022849	1682.936	-0.16603	-198.511
40	2	11.87525	1.483724	2.010532	1709.613	-0.16333	-198.51
40	30	11.88115	1.486194	2.014229	1687.742	-0.16592	-198.512
40	3	11.87681	1.486534	2.010395	1710.652	-0.16323	-198.511
40	40	11.86538	1.471425	2.003836	1724.995	-0.16972	-198.512
40	4	11.87743	1.483823	1.999971	1718.449	-0.16294	-198.517
40	5	11.87214	1.482342	2.00831	1706.404	-0.16337	-198.516
40	60	11.87121	1.475024	2.006038	1732.049	-0.16823	-198.508
40	80	11.88636	1.488168	2.011521	1680.146	-0.1654	-198.513

Data for 5° Thrust Vector

X	Y	Floating	Plasma	E temp	Density OML	Ion Sat Current	Density thin sheath
5	0	23.06492	51.81218	17.61621	3.61E+15	-1E-05	1.38E+15
5	10	21.7979	46.68739	13.16669	3.65E+15	-1.5E-05	4.26E+15
5	15	22.00634	47.65969	14.10327	8.85E+15	-2.1E-05	6.21E+15
5	20	21.90178	48.73479	16.08779	4.35E+15	-1.8E-05	4.09E+15
5	40	26.07622	56.71798	18.97239	2.04E+15	-1.1E-05	1.42E+15
5	5	22.02923	45.43853	11.67059	2.89E+15	-9.8E-06	2.44E+15
75	100	71.28421	114.4256	21.58151	2.31E+15	-4.7E-06	2.41E+14
75	10	23.00871	52.77961	18.49532	2.88E+15	-1E-05	1.25E+15
75	10	21.84802	48.6817	18.95531	7.63E+14	-5.5E-06	3.96E+14
75	120	85.63998	120.3299	24.13667	1.2E+15	-6.6E-06	3.69E+14
75	140	93.82403	147.3148	10.44393	1.51E+15	-5.7E-06	1.17E+15
75	20	22.00147	48.65299	15.60186	2.12E+15	-7.4E-06	9.65E+14
75	30	22.8409	52.56521	19.37938	2.27E+15	-6.5E-06	5.37E+14
75	35	23.05909	54.70999	16.63004	1.58E+15	-7.9E-06	9.68E+14
75	40	23.02618	55.8612	16.335	3.02E+15	-6.4E-06	6.99E+14
75	50	24.87327	54.63821	14.23302	1.91E+15	-7.2E-06	1.06E+15
75	5	22.79919	51.56731	18.91408	2.4E+15	-7.3E-06	6.83E+14
75	60	28.09544	65.01998	20.73413	3.28E+15	-5.6E-06	3.5E+14
50	80	43.42147	78.51329	14.53935	2.84E+15	-5.2E-06	5.83E+14
50	60	28.03924	56.86384	11.46837	1.43E+15	-7.3E-06	1.5E+15
50	50	24.9506	54.64363	13.79894	1.96E+15	-6.8E-06	1.01E+15
50	5	23.05408	48.57931	14.78814	2.8E+15	-1.1E-05	2.2E+15
50	40	23.04203	55.70261	16.75872	3.05E+15	-6.5E-06	6.86E+14
50	35	23.05015	50.64675	13.81853	2.52E+15	-7.2E-06	1.12E+15
50	30	23.00329	47.42295	13.62883	2.97E+15	-8E-06	1.37E+15
50	20	21.8277	41.26911	8.861618	4.1E+15	-8.8E-06	3E+15
50	15	21.78964	44.54492	10.83127	3.9E+15	-1.1E-05	3.18E+15
50	10	22.00715	50.55343	16.06857	3.23E+15	-1E-05	1.64E+15
50	100	62.93195	102.0125	13.37724	2.46E+15	-4.6E-06	5.39E+14
20	15	20.79378	38.22774	8.539165	4.97E+15	-1E-05	3.93E+15
20	20	22.0165	40.28448	8.067288	3.94E+15	-1.5E-05	7.58E+15
20	30	22.85038	42.4424	9.419701	1.08E+15	-1.2E-05	4.43E+15
20	35	22.90375	41.49461	6.209825	1.64E+15	-7.8E-06	3.94E+15
20	50	27.17095	52.76999	9.392951	5.61E+14	-7.6E-06	2.2E+15
20	5	22.02666	42.32389	10.01616	3.14E+15	-1.2E-05	4.33E+15
20	60	30.24442	54.66421	8.787225	1.1E+15	-7.2E-06	2.25E+15
20	80	43.54323	73.31739	8.1326	2.13E+15	-6.2E-06	1.95E+15
30	0	21.84937	36.22382	5.97015	2.63E+15	-6.2E-06	2.94E+15
30	10	21.88079	38.30074	7.120876	4.65E+15	-7.2E-06	2.93E+15
30	120	82.36322	112.1805	14.40508	1.05E+15	-6.2E-06	8.13E+14
30	15	21.83027	41.31529	9.616085	5.09E+15	-1.3E-05	4.8E+15
30	20	21.79303	41.28847	9.258749	5.19E+15	-1.2E-05	4.74E+15
30	30	22.89007	39.30907	7.423907	2.35E+15	-1.1E-05	5.02E+15
30	40	22.89928	56.68344	18.02505	1.68E+15	-7.6E-06	7.94E+14
30	50	26.95737	56.70484	13.88864	3.18E+15	-5E-06	5.91E+14
30	5	21.81876	41.51398	10.20976	1.58E+15	-1.3E-05	4.39E+15
30	60	30.23033	53.81827	8.961985	1.75E+15	-7.1E-06	2.11E+15
30	80	40.49955	81.35706	17.76352	1.45E+15	-6.9E-06	6.78E+14
40	0	21.87835	40.33825	7.809818	1.45E+15	-1.2E-05	6.01E+15
40	100	57.77303	101.0726	10.84189	1.4E+15	-6.4E-06	1.31E+15
40	10	21.80278	48.72517	12.96832	3.43E+15	-1.1E-05	2.41E+15
40	120	84.64235	109.0555	14.57165	2.12E+15	-4.6E-06	4.71E+14
40	140	89.72855	116.3339	17.2334	1.82E+15	-5.7E-06	5.05E+14
40	15	21.95813	39.22631	8.025968	3.82E+15	-7.9E-06	2.94E+15
40	20	21.79289	47.43825	14.62602	3.19E+15	-1.1E-05	2.19E+15
40	30	22.96415	45.58074	11.89532	2.19E+15	-1E-05	2.64E+15
40	35	21.79831	51.57571	13.33105	2.53E+15	-7.5E-06	1.26E+15
40	40	23.0446	54.81658	15.9277	1.61E+15	-7.8E-06	1.01E+15
40	50	25.90882	51.66212	10.73627	1.16E+15	-7.4E-06	1.72E+15
40	5	21.82079	50.74697	16.43423	1.54E+15	-1.3E-05	2.27E+15
40	60	29.05921	64.14249	15.28869	1.41E+15	-7.1E-06	9.27E+14
40	80	40.45066	76.297	13.11377	2.34E+15	-6.1E-06	9.17E+14
50	0	21.77258	53.62541	20.06844	2E+15	-7.9E-06	7.13E+14
0	35	24.87435	44.43467	5.975516	8.74E+14	-7.6E-06	4.03E+15
0	40	25.96678	55.70518	11.66973	1.11E+15	-7.4E-06	1.53E+15
0	50	31.03225	57.94734	9.845345	1.94E+15	-6.8E-06	1.7E+15
0	60	39.42405	79.33729	16.15231	1.24E+15	-7.2E-06	8.67E+14

X	Y	Floating	Plasma	E temp	Density OML	Ion Sat Current	Density thin sheath
0	100	103.0924	139.1046	15.16942	1.17E+15	-6.4E-06	7.7E+14
0	120	102.8921	128.5796	4.315128	1.52E+15	-5.5E-06	3.69E+15
0	80	85.44048	147.0972	27.45623	6.16E+14	-7.3E-06	3.5E+14
100	0	22.93178	45.3704	8.364734	2.51E+15	-6.6E-06	2.09E+15
100	100	55.70911	100.8131	13.73306	1.64E+15	-5.8E-06	7.65E+14
100	10	23.03661	38.29898	6.140811	2.26E+15	-7.2E-06	3.55E+15
100	120	87.69564	147.2682	26.39929	8.5E+14	-6.8E-06	3.27E+14
100	140	95.71243	147.2186	18.85606	1.34E+15	-6.3E-06	5.23E+14
100	15	21.86549	40.44646	7.938463	1.24E+15	-7.9E-06	2.94E+15
100	20	21.77068	39.42866	7.281854	2.09E+15	-7.3E-06	2.94E+15
100	30	21.77475	43.32991	9.215151	1.1E+15	-7.9E-06	2.42E+15
100	35	21.99984	37.20641	5.547678	9.26E+14	-7.7E-06	4.45E+15
100	40	22.90551	39.38572	6.881854	1.63E+15	-7.2E-06	3.07E+15
100	50	23.83379	48.66531	11.1242	9.24E+14	-7.3E-06	1.6E+15
100	5	22.80731	53.78591	16.8359	2.27E+15	-7E-06	7.76E+14
100	60	25.89649	54.79477	15.5807	1.7E+15	-7E-06	8.74E+14
100	80	35.1173	60.76307	10.61432	1.13E+15	-6.4E-06	1.38E+15
10	0	21.89068	36.41451	5.06854	1.89E+15	-1.2E-05	8.99E+15
10	100	86.53332	111.2626	16.78868	2.54E+15	-3.8E-06	2.56E+14
10	10	19.78762	48.67736	16.83446	1.21E+15	-1.7E-06	5.59E+13
10	120	89.5793	127.7701	13.37043	6.9E+14	-7.1E-06	1.15E+15
10	140	99.00165	130.8314	12.00932	1.75E+15	-5.3E-06	8.3E+14
10	15	22.00269	44.41869	13.58826	6.62E+15	-1.5E-05	3.83E+15
10	20	21.81836	36.39921	5.17169	4.17E+15	-1.5E-05	1.25E+16
10	30	21.79357	47.47482	12.87522	1.9E+15	-4.5E-06	5.56E+14
10	40	24.99828	52.7597	11.66795	1.71E+15	-7.3E-06	1.48E+15
10	5	22.01677	42.32159	10.20322	2.41E+15	-1.2E-05	4.02E+15
10	60	31.04837	78.31054	24.17306	1.02E+15	-7.3E-06	4.4E+14
10	80	53.78861	105.1655	21.34693	2.13E+15	-5.4E-06	3.17E+14
150	0	26.09924	49.66876	9.740188	1.98E+15	-7.2E-06	1.91E+15
175	0	28.16167	72.19245	29.60003	1.41E+15	-7.8E-06	3.44E+14
50	100	62.93195	109.0577	16.51712	1.86E+15	-5.8E-06	5.69E+14
50	120	83.60816	111.3307	14.95264	2.21E+15	-4.9E-06	5.03E+14
50	30	23.00329	48.69009	14.51551	1.85E+15	-9.1E-06	1.54E+15
50	35	23.05015	52.70336	14.29723	2.24E+15	-7.5E-06	1.14E+15
50	40	23.04203	49.66632	12.01688	2.41E+15	-7.3E-06	1.41E+15
50	50	24.9506	59.98444	18.45354	1.96E+15	-6.8E-06	6.34E+14
50	80	43.42147	79.30207	11.31687	1.6E+15	-7E-06	1.45E+15

Data for 5° Thrust Vector Continued

X	Y	Debye OML	Debye thin sheath	Ratio OML	Ratio thin sheath
5	0	0.000519	0.000841	0.220142	0.090653
5	10	0.000446	0.000413	0.256162	0.184493
5	15	0.000297	0.000354	0.385303	0.215215
5	20	0.000452	0.000466	0.25306	0.163509
5	40	0.000716	0.000859	0.159605	0.088693
5	5	0.000472	0.000514	0.242267	0.148206
75	100	0.000718	0.002224	0.159094	0.03426
75	10	0.000596	0.000904	0.191865	0.084308
75	10	0.001171	0.001626	0.097581	0.046856
75	120	0.001053	0.0019	0.10853	0.040108
75	140	0.000618	0.000703	0.184825	0.108329
75	20	0.000638	0.000945	0.179221	0.080656
75	30	0.000686	0.001412	0.166631	0.053985
75	35	0.000763	0.000974	0.149812	0.078249
75	40	0.000546	0.001136	0.209152	0.06709
75	50	0.000642	0.000861	0.17799	0.088455
75	5	0.00066	0.001237	0.173238	0.061623
75	60	0.000591	0.00181	0.193423	0.042107
50	80	0.000532	0.001173	0.214936	0.064936
50	60	0.000665	0.000649	0.171888	0.117404
50	50	0.000624	0.000869	0.183287	0.087715
50	5	0.00054	0.00061	0.211492	0.125004
50	40	0.000551	0.001162	0.207502	0.065597
50	35	0.00055	0.000825	0.207814	0.092394
50	30	0.000503	0.000741	0.227113	0.102903
50	20	0.000345	0.000404	0.330944	0.188559
50	15	0.000392	0.000433	0.291949	0.175848
50	10	0.000524	0.000736	0.218103	0.103594
50	100	0.000548	0.00117	0.208748	0.065114
20	15	0.000308	0.000346	0.37123	0.219939
20	20	0.000336	0.000242	0.339885	0.314429
20	30	0.000694	0.000342	0.164602	0.222484
20	35	0.000457	0.000295	0.249927	0.258243
20	50	0.000961	0.000486	0.118895	0.156818
20	5	0.000419	0.000357	0.272502	0.213209
20	60	0.000663	0.000464	0.172398	0.164183
20	80	0.000459	0.00048	0.248945	0.15867
30	0	0.000354	0.000335	0.322587	0.227532
30	10	0.000291	0.000366	0.392991	0.208122
30	120	0.000872	0.000989	0.131087	0.077058
30	15	0.000323	0.000333	0.353912	0.229114
30	20	0.000314	0.000328	0.364055	0.232085
30	30	0.000418	0.000286	0.273586	0.266819
30	40	0.00077	0.001119	0.148373	0.068087
30	50	0.000491	0.001139	0.232607	0.066892
30	5	0.000597	0.000358	0.191385	0.212699
30	60	0.000532	0.000484	0.214772	0.157504
30	80	0.000823	0.001202	0.138921	0.063369
40	0	0.000546	0.000268	0.209484	0.284529
40	100	0.000654	0.000676	0.174754	0.112804
40	10	0.000457	0.000546	0.25004	0.139668
40	120	0.000615	0.001307	0.185743	0.058294
40	140	0.000723	0.001372	0.1582	0.055536
40	15	0.000341	0.000388	0.335456	0.196409
40	20	0.000503	0.000608	0.227199	0.125385
40	30	0.000548	0.000498	0.208631	0.152899
40	35	0.000539	0.000765	0.211984	0.099616
40	40	0.00074	0.000932	0.154483	0.081737
40	50	0.000715	0.000588	0.159809	0.129681
40	5	0.000767	0.000632	0.149082	0.120634
40	60	0.000772	0.000954	0.147981	0.079871
40	80	0.000556	0.000888	0.205502	0.085777
50	0	0.000745	0.001247	0.153425	0.061127
0	35	0.000615	0.000286	0.186	0.266281
0	40	0.000761	0.000649	0.150219	0.117345
0	50	0.000529	0.000566	0.216218	0.134676
0	60	0.000847	0.001014	0.134926	0.075136

X	Y	Debye OML	Debye thin sheath	Ratio OML	Ratio thin sheath
0	100	0.000847	0.001043	0.134869	0.07307
0	120	0.000396	0.000254	0.28871	0.300084
0	80	0.001569	0.002082	0.072848	0.036591
100	0	0.000429	0.00047	0.266283	0.161971
100	100	0.000679	0.000995	0.168269	0.076561
100	10	0.000387	0.000309	0.294998	0.246502
100	120	0.00131	0.00211	0.087268	0.036122
100	140	0.000882	0.001411	0.12962	0.054008
100	15	0.000595	0.000386	0.192097	0.19742
100	20	0.000439	0.00037	0.260377	0.20603
100	30	0.00068	0.000458	0.168034	0.166277
100	35	0.000575	0.000262	0.198746	0.290588
100	40	0.000482	0.000352	0.236969	0.216512
100	50	0.000815	0.000619	0.140168	0.123154
100	5	0.00064	0.001094	0.1785	0.069631
100	60	0.000712	0.000992	0.160602	0.076791
100	80	0.000719	0.000652	0.158943	0.116951
10	0	0.000385	0.000176	0.297267	0.432003
10	100	0.000604	0.001904	0.189108	0.040029
10	10	0.000878	0.004078	0.13017	0.018684
10	120	0.001034	0.000803	0.110495	0.094933
10	140	0.000616	0.000894	0.185583	0.085264
10	15	0.000337	0.000442	0.339452	0.172267
10	20	0.000262	0.000151	0.436976	0.505101
10	30	0.000612	0.001131	0.186798	0.067367
10	40	0.000613	0.000659	0.186465	0.115634
10	5	0.000483	0.000375	0.236461	0.20347
10	60	0.001143	0.001741	0.100014	0.043775
10	80	0.000744	0.001927	0.153694	0.039542
150	0	0.000521	0.00053	0.219183	0.143785
175	0	0.001076	0.002179	0.106242	0.034976
50	100	0.000701	0.001265	0.163093	0.060219
50	120	0.000611	0.001282	0.187048	0.059455
50	30	0.000658	0.000722	0.173716	0.105516
50	35	0.000593	0.000832	0.192721	0.091584
50	40	0.000525	0.000687	0.217921	0.110927
50	50	0.000721	0.001268	0.158494	0.060106
50	80	0.000624	0.000656	0.183109	0.116152

Thruster Conditions for 5° Thrust Vector

X	Y	Forward Power	Reverse Power	Screen Grid Current	Screen Grid Voltage	Accel Grid Current	Accel Grid Voltage
5	0	11.05652	1.241639	2.095647	1791.281	-0.15859	-199.481
5	10	11.05908	1.240101	2.094704	1791.321	-0.15912	-199.48
5	15	11.06419	1.243939	2.09704	1791.541	-0.16474	-199.48
5	20	11.07086	1.249342	2.099683	1791.376	-0.16078	-199.48
5	40	11.07401	1.249898	2.098552	1791.318	-0.15855	-199.474
5	5	11.05757	1.240195	2.09454	1791.257	-0.15832	-199.476
75	100	11.03931	1.237167	2.101998	1790.617	-0.1618	-199.467
75	10	11.04009	1.234132	2.095044	1789.676	-0.15825	-199.486
75	10	11.04528	1.236688	2.094166	1790.537	-0.15887	-199.477
75	120	11.04641	1.240428	2.104221	1790.65	-0.16252	-199.473
75	140	11.0105	1.22963	2.09857	1790.832	-0.16276	-199.459
75	20	11.05989	1.247712	2.102537	1790.582	-0.15953	-199.487
75	30	11.03748	1.235234	2.094431	1790.629	-0.15927	-199.484
75	35	11.04237	1.236678	2.095378	1790.747	-0.15965	-199.482
75	40	11.04137	1.23656	2.097982	1790.636	-0.16069	-199.483
75	50	11.03691	1.234642	2.09612	1790.603	-0.16003	-199.481
75	5	11.0547	1.240142	2.097436	1790.6	-0.15829	-199.468
75	60	11.05067	1.243693	2.101419	1790.641	-0.16139	-199.475
50	80	11.04314	1.238723	2.099924	1790.979	-0.16183	-199.473
50	60	11.03457	1.234681	2.096031	1790.928	-0.16095	-199.474
50	50	11.04533	1.239665	2.102009	1789.124	-0.1603	-199.475
50	5	11.0572	1.242915	2.09955	1789.19	-0.15886	-199.474
50	40	11.0454	1.239295	2.098566	1790.904	-0.16053	-199.476
50	35	11.04148	1.235468	2.09406	1790.949	-0.15975	-199.477
50	30	11.03544	1.233494	2.092649	1790.935	-0.15939	-199.478
50	20	11.0596	1.248575	2.102829	1790.902	-0.16017	-199.495
50	15	11.07362	1.252451	2.103975	1790.868	-0.16007	-199.483
50	10	11.05319	1.24094	2.09774	1790.866	-0.1598	-199.498
50	100	11.04276	1.237697	2.101197	1791.046	-0.16224	-199.466
20	15	11.06479	1.248243	2.102477	1791.084	-0.15926	-199.481
20	20	11.05405	1.243431	2.099192	1791.099	-0.15939	-199.48
20	30	11.04279	1.239817	2.096395	1791.085	-0.15998	-199.487
20	35	11.03173	1.232713	2.093231	1791.181	-0.16018	-199.487
20	50	11.04582	1.239006	2.098348	1787.266	-0.15975	-199.471
20	5	11.04769	1.236735	2.093506	1791.02	-0.15794	-199.479
20	60	11.02352	1.229223	2.093404	1791.161	-0.16094	-199.481
20	80	11.04285	1.238316	2.099028	1791.239	-0.16222	-199.476
30	0	11.04727	1.237814	2.095737	1791.018	-0.15824	-199.489
30	10	11.045	1.238373	2.095488	1791.043	-0.15813	-199.473
30	120	11.03859	1.235667	2.101333	1791.037	-0.16263	-199.469
30	15	11.05004	1.241793	2.099057	1791.027	-0.1591	-199.487
30	20	11.04358	1.23908	2.097321	1791.057	-0.159	-199.485
30	30	11.03434	1.23512	2.094298	1791.081	-0.15945	-199.484
30	40	11.04617	1.24097	2.097687	1791.106	-0.16064	-199.48
30	50	11.04979	1.241158	2.098851	1791.114	-0.16094	-199.477
30	5	11.05345	1.241448	2.096389	1791.061	-0.15899	-199.487
30	60	11.03147	1.231626	2.095202	1791.099	-0.16083	-199.478
30	80	11.04168	1.237116	2.09825	1791.146	-0.16165	-199.471
40	0	11.04792	1.236515	2.094831	1790.931	-0.15785	-199.482
40	100	11.04462	1.241041	2.101935	1791.026	-0.16245	-199.467
40	10	11.05955	1.24572	2.101607	1789.486	-0.15895	-199.484
40	120	11.04271	1.239033	2.102872	1790.979	-0.16281	-199.465
40	140	11.02729	1.230295	2.100711	1790.944	-0.16315	-199.458
40	15	11.06196	1.247991	2.115162	1780.714	-0.15864	-199.479
40	20	11.05046	1.241893	2.099054	1791.017	-0.15934	-199.491
40	30	11.03871	1.237011	2.09481	1791.055	-0.15974	-199.481
40	35	11.03774	1.235297	2.094554	1791.043	-0.1599	-199.48
40	40	11.04669	1.240299	2.097888	1791.038	-0.16083	-199.483
40	50	11.05731	1.245043	2.102454	1789.36	-0.16088	-199.479
40	5	11.05992	1.242328	2.096717	1791.003	-0.1589	-199.491
40	60	11.04289	1.237427	2.097514	1791.092	-0.16139	-199.482
40	80	11.04691	1.241138	2.100993	1791.046	-0.16173	-199.465
50	0	11.06221	1.242962	2.098815	1790.832	-0.15859	-199.488
0	35	11.03022	1.232102	2.093815	1790.717	-0.16019	-199.481
0	40	11.03734	1.23603	2.093525	1791.242	-0.16021	-199.474
0	50	11.02995	1.233106	2.092471	1791.183	-0.16082	-199.479

X	Y	Forward Power	Reverse Power	Screen Grid Current	Screen Grid Voltage	Accel Grid Current	Accel Grid Voltage
0	60	11.03123	1.234269	2.09345	1791.254	-0.16064	-199.475
0	100	11.03111	1.233466	2.09726	1791.124	-0.16199	-199.477
0	120	11.04274	1.239335	2.104265	1791.085	-0.16303	-199.459
0	80	11.04091	1.23871	2.099022	1791.169	-0.16186	-199.471
100	0	11.01565	1.227468	2.097843	1790.373	-0.16424	-199.457
100	100	11.00771	1.229687	2.099445	1790.523	-0.16324	-199.453
100	10	11.00448	1.222159	2.096778	1789.628	-0.16372	-199.464
100	120	11.00636	1.22978	2.09941	1790.573	-0.16325	-199.458
100	140	11.00865	1.230134	2.099349	1790.566	-0.16253	-199.459
100	15	11.00532	1.222267	2.096319	1790.351	-0.1638	-199.456
100	20	11.01036	1.223867	2.096903	1789.743	-0.16318	-199.461
100	30	11.03168	1.235832	2.102843	1790.442	-0.16385	-199.454
100	35	11.01704	1.235104	2.1019	1790.471	-0.16393	-199.458
100	40	11.0175	1.235904	2.104425	1789.179	-0.16385	-199.454
100	50	11.01083	1.23326	2.099685	1790.511	-0.16354	-199.461
100	5	10.99226	1.216691	2.095664	1787.955	-0.16369	-199.471
100	60	11.00946	1.231413	2.098778	1790.54	-0.1636	-199.461
100	80	11.00123	1.226441	2.097622	1790.51	-0.16345	-199.457
10	0	11.06861	1.246904	2.100595	1789.363	-0.15828	-199.474
10	100	11.02449	1.231522	2.096094	1791.137	-0.16191	-199.478
10	10	11.06424	1.245669	2.097374	1791.303	-0.15903	-199.469
10	120	11.02817	1.230551	2.099313	1791.112	-0.16298	-199.464
10	140	11.0375	1.235785	2.103088	1790.957	-0.16332	-199.46
10	15	11.07471	1.256254	2.105941	1790.117	-0.16143	-199.476
10	20	11.06705	1.251832	2.102925	1791.255	-0.16079	-199.487
10	30	11.046	1.241448	2.095627	1790.995	-0.15984	-199.488
10	40	11.03942	1.23588	2.093829	1791.205	-0.1602	-199.479
10	5	11.06411	1.245067	2.097508	1791.323	-0.15893	-199.492
10	60	11.03326	1.236326	2.095301	1791.265	-0.16117	-199.482
10	80	11.04034	1.237916	2.098682	1791.161	-0.1617	-199.476
150	0	10.99289	1.218059	2.094799	1787.96	-0.16381	-199.46
175	0	10.99705	1.220988	2.094146	1790.13	-0.16432	-199.46
50	100	11.04276	1.237697	2.101197	1791.046	-0.16224	-199.466
50	120	11.04609	1.239903	2.103234	1790.871	-0.16256	-199.46
50	30	11.03544	1.233494	2.092649	1790.935	-0.15939	-199.478
50	35	11.04148	1.235468	2.09406	1790.949	-0.15975	-199.477
50	40	11.0454	1.239295	2.098566	1790.904	-0.16053	-199.476
50	50	11.04533	1.239665	2.102009	1789.124	-0.1603	-199.475
50	80	11.04314	1.238723	2.099924	1790.979	-0.16183	-199.473